

THESIS
3
2002

This is to certify that the

dissertation entitled

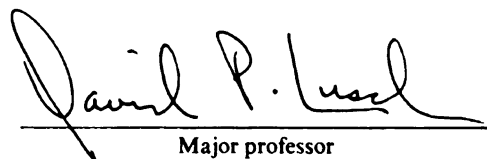
A CLASSIFICATION-BASED ASSESSMENT OF THE
OPTIMAL SPATIAL AND SPECTRAL RESOLUTION
OF COASTAL WETLAND IMAGERY

presented by

Brian L. Becker

has been accepted towards fulfillment
of the requirements for

Ph.D. degree in Geography


Major professor

Date 8/1/02

LIBRARY
Michigan State
University

PLACE IN RETURN BOX to remove this checkout from your record.
TO AVOID FINES return on or before date due.
MAY BE RECALLED with earlier due date if requested.

DATE DUE	DATE DUE	DATE DUE
JUL 21 2006		
07 17 06		



A CLASSIFICATION-BASED ASSESSMENT OF THE OPTIMAL SPATIAL
AND SPECTRAL RESOLUTION OF COASTAL WETLAND IMAGERY

By

Brian L. Becker

A DISSERTATION

Submitted to
Michigan State University
in partial fulfillment of the requirements
for the degree of

DOCTOR OF PHILOSOPHY

Department of Geography

2002

ABSTRACT

A CLASSIFICATION-BASED ASSESSMENT OF THE OPTIMAL SPATIAL AND SPECTRAL RESOLUTION OF COASTAL WETLAND IMAGERY

By

Brian L. Becker

Great Lakes wetlands are increasingly being recognized as vital ecosystem components that provide valuable functions such as sediment retention, wildlife habitat, and nutrient removal. Aerial photography has traditionally provided a cost effective means to inventory and monitor coastal wetlands, but is limited by its broad spectral sensitivity and non-digital format. Airborne sensor advancements have now made the acquisition of digital imagery with high spatial and spectral resolution a reality.

In this investigation, we selected two Lake Huron coastal wetlands, each from a distinct eco-region, over which, digital, airborne imagery (AISA or CASI-II) was acquired. The 1-meter images contain approximately twenty, 10-nanometer-wide spectral bands strategically located throughout the visible and near-infrared. The 4-meter hyperspectral imagery contains 48 contiguous bands across the visible and short-wavelength near-infrared. Extensive, in-situ reflectance spectra (SE-590) and sub-meter GPS locations were acquired for the dominant botanical and substrate classes field-delineated at each location.

Normalized in-situ spectral signatures were subjected to Principal Components and 2nd Derivative analyses in order to identify the most botanically explanative image bands. Three image-based investigations were implemented in order to evaluate the ability of three classification algorithms (ISODATA, Spectral Angle Mapper and Maximum-Likelihood) to differentiate botanical regions-of-interest. Two additional investigations were completed in order to assess classification changes associated with the independent manipulation of both spatial and spectral resolution.

Of the three algorithms tested, the Maximum-Likelihood classifier best differentiated (89%) the regions-of-interest in both study sites. Covariance-based PCA rotation consistently enhanced the performance of the Maximum-Likelihood classifier. Seven non-overlapping bands (425.4, 514.9, 560.1, 685.5, 731.5, 812.3 and 916.7 nanometers) were identified that represented the best performing bands with respect to classification performance. A spatial resolution of 2 meters or less was determined to be the as being most appropriate in Great Lakes coastal wetland environments. This research represents the first step in evaluating the effectiveness of applying high-resolution, narrow-band imagery to the detailed mapping of coastal wetlands in the Great Lakes region.

to the memory of my grandfathers, for they instilled my appreciation for the natural world and the game species I passionately pursue. I must also dedicate this work to my twins, Brianna and Brendin, for unknowingly being my inspiration and motivation.

ACKNOWLEDGMENTS

I would like to express my appreciation to the three members of my research committee. Special thanks also goes to my committee chairperson Dr. David Lusch who has been my supervisor, research partner, and friend. Without his guidance and support, the completion of this body of work would have been doubtful. Thanks for statistical help must also go out to Dr. Bruce Pigozzi. I would also like to thank Robb Macleod at the Midwestern Ducks Unlimited office, for his support greatly contributed to the success and end-user applicability of this research. The Great Lakes Fisheries Commission must also be thanked for their support of my research efforts.

I would like to thank my Parents for their mental and financial support during my graduate school endeavors. Finally, special thanks must also go out to my wife Julie, for she supported my Ph.D. endeavors and allowed me to avoid “regular” employment just a little longer.

TABLE OF CONTENTS

LIST OF TABLES.....	ix
LIST OF FIGURES.....	x
LIST OF TERMS.....	xi
CHAPTER 1: INTRODUCTION	1
1.1 Great Lakes Coastal Wetlands.....	1
1.2 Wetland Remote Sensing.....	5
1.2.1 Biophysical Relationships.....	6
1.2.2 Aerial Photography of Wetlands.....	9
1.2.3 Digital Wetland Imagery.....	12
1.2.4 Satellite Remote Sensing of Wetlands.....	13
1.2.5 Airborne Hyperspectral Systems.....	14
1.2.6 Hyperspectral Wetland Applications.....	20
1.3 Study Sites.....	21
1.3.1 Les Cheneaux Island Complex.....	23
1.3.2 Wildfowl Bay Island Complex.....	26
1.4 Statement of Problem.....	28
CHAPTER 2: <i>A Comparison of Image Classification Strategies to Optimize Wetland</i> <i>Botanical Differentiation</i>	32
2.1 Introduction and Rationale.....	32
2.2 Methods.....	35
2.2.1 Airborne Image Acquisition.....	35
2.2.2 Image Geo-rectification.....	37
2.2.3 Imagery Percent Reflectance Transformation.....	42
2.2.4 Imagery Principal Components Rotation.....	46
2.2.5 Accuracy Assessment Regions-of-Interest.....	49
2.2.6 Image Classifications.....	52
2.3 Results and Discussion.....	60
2.3.1 ISODATA - Investigation 1.....	61
2.3.2 Maximum-Likelihood - Investigation 1.....	64
2.3.3 Spectral Angle Mapper - Investigation 1.....	66
2.3.4 PC-rotated Classifications - Investigation 2.....	69
2.3.5 Prentiss Bay Classifications - Investigation 3.....	72
2.4 Summary and Conclusions.....	74

CHAPTER 3:	<i>Principal components and second derivative analyses of hyperspectral reflectance data from freshwater coastal wetlands.....</i>	<i>79</i>
3.1	Introduction and Rationale	79
3.2	Methods.....	83
3.2.1	Spectral Data Pre-Processing.....	83
3.2.2	2 nd Derivative Approximations	90
3.2.3	Principal Components Analysis.....	93
3.2.4	Image classifications – Bandset Optimization.....	98
3.2.5	Image classifications – Bandwidth Optimization.....	104
3.2.6	Image classifications – IKONOS Spectral Simulation.....	106
3.3	Results and Discussion.....	108
3.3.1	Representative Spectral Clusters.....	108
3.3.2	2 ND derivative Summary	112
3.3.3	PCA Loading Curve Inspection.....	119
3.3.4	Loading Curve Derivation.....	122
3.3.5	Correlation-based, PCA Factor Interpretation.....	124
3.3.6	Covariance-based, PCA Dimension Interpretation.....	130
3.3.7	Bandset Optimization – Investigation 4.....	134
3.4	Summary and Conclusions.....	144
CHAPTER 4:	<i>A Classification-based Assessment of the Optimal Spatial Resolution of Coastal Wetland Imagery</i>	<i>149</i>
4.1	Introduction and Rationale.....	149
4.2	Methods.....	151
4.2.1	Image Spatial Degradation – Investigation 5.....	151
4.3	Results and Discussion.....	157
4.3.1	Spectral Angle Mapper – Investigation 5.....	157
4.3.2	Mahalanobis Classifications - Investigation 5.....	161
4.4	Summary and Conclusions.....	166
CHAPTER 5:	CONCLUSIONS AND FUTURE RESEARCH.....	167
5.1	Classifier Performance and Transferability.....	167
5.2	Optimal Spectral Resolution.....	170
5.3	Optimal Spatial Resolution.....	174
5.4	Limitations of the Technology.....	175
5.5	Recommendations for Future Research.....	178
APPENDIX A.....		180
APPENDIX B.....		184
APPENDIX C.....		201

APPENDIX D.....214

APPENDIX E.....218

BIBLIOGRAPHY.....225

LIST OF TABLES

Table 1.1.	Instrument Spectral Sensitivities and Spatial Resolutions.....	15
Table 2.1.	Instrument Specifications and Flight Parameters.....	38
Table 2.2.	Instrument Bandsets with FWHM.....	39
Table 2.3.	Image Rectification Summary.....	42
Table 2.4.	Image Percent Reflectance Methodology.....	47
Table 2.5.	Prentiss Bay Regions-of-Interest.....	52
Table 2.6.	Horseshoe Bay, 1-meter Regions-of-Interest.....	53
Table 2.7.	Classification Accuracy Summary.....	63
Table 3.1.	Collected In-situ Spectral Signatures.....	85
Table 3.2.	Horseshoe Bay, 4-meter Regions-of-Interest.....	101
Table 3.3.	Bandwidth Manipulation FWHM Parameters.....	106
Table 3.4.	In-situ 2 nd Derivative Summary.....	115
Table 3.5.	Summary of Investigation-4 Classifications.....	135
Table 4.1.	Summary Table, SAM Spatial Degradation.....	158
Table 4.2.	Summary Table, Mahalanobis-Distance Spatial Degradation.....	162

LIST OF FIGURES

Figure 1.1.	Five Characteristic Spectral Signatures.....	8
Figure 1.2.	Synthetically Resampled Spectral Signatures.....	17
Figure 1.3.	Lake Huron Ecoregions.....	23
Figure 1.4.	Prentiss Bay Image Area and Vicinity.....	25
Figure 1.5.	Horseshoe Bay Image Area (1 and 4 meter) and Vicinity.....	27
Figure 2.1.	Horseshoe Bay; Dimensions 1-6 PCA Images	50
Figure 2.2.	Isodata Classification Parameters.....	56
Figure 2.3.	Nine Representative Spectra.....	66
Figure 2.4.	PC-transformed Spectral Signatures.....	71
Figure 3.1.	Representative Spectral Signatures.....	90
Figure 3.2.	Derivative Calculation Schematic.....	92
Figure 3.3.	4-meter, Horseshoe Bay Rectangular Image Subset.....	102
Figure 3.4.	Nine Representative Spectra.....	109
Figure 3.5.	Representative 2 nd Derivative Plots.....	113
Figure 3.6.	Frequency of 2 nd Derivative Occurrences	118
Figure 3.7.	Key Wavelength Domains - Dimensional PCA Loadings.....	122
Figure 3.8.	Frequency of 2 nd -Derivative Occurrences of Loading Curves.....	124
Figure 3.9.	Correlation-based, PCA Component Loading Curves.....	126
Figure 3.10.	Covariance-based, PCA Component Loading Curves.....	131
Figure 4.1.	Spatial Manipulation, Image Processing Schematic.....	155
Figure 5.1.	Horseshoe Bay; PC654321 Max.-Likelihood Classification	176
Figure E-1.	Prentiss Bay; False Color Composite.....	219
Figure E-2.	Horseshoe Bay; True Color Composite and ROIs	220
Figure E-3.	Horseshoe Bay; False Color Composite.....	221
Figure E-4.	Prentiss Bay PCA Image; 4, 3, 2 Color Composite.....	222
Figure E-5.	Horseshoe Bay PCA Image; 4, 3, 2 Color Composite.....	223
Figure E-6.	Pixel Level Spatial Degradation Patterns.....	224

LIST OF TERMS

2nd Derivative Approximation - a slope-based method used to differentiate 1st-order polynomials that would otherwise not yield higher-order derivatives.

AISA - A hyperspectral sensor deployed by 3DI, Inc.; Airborne Imaging Spectrometer for Applications

ARC/INFO - GIS software developed by Environmental Systems Research Inc. (ESRI).

ARCVIEW - Desktop GIS software developed by Environmental Systems Research Inc. (ESRI).

CASI-II - a hyperspectral sensor manufactured and deployed by ITRES Inc.; Compact Airborne Spectrometric Imager.

ENVI - The Environment for Visualizing Imagery; image processing software developed by Research Systems, Inc., a KODAK company.

ERDAS - The Earth Resources Data Analysis System; image processing software developed by ERDAS, Inc., a Leica Geosystems company.

Hyperspectral Sensors - imaging spectrometers capable of recording spectral data similar in nature to laboratory spectrometers, making it possible to construct spectral reflectance curves.

IKONOS - a commercial earth resource satellite remote sensing system developed by a U.S. private company designed to provide high spatial resolution imagery.

Image Classification - the process of establishing a link between an informational category of interest and a related image spectral class.

Landsat - A series of satellite remote sensing platforms (NASA) carrying instruments specifically designed to acquire data about earth resources on a systematic, repetitive, medium resolution, multispectral basis.

Near-infrared Spectrum - that portion of the electromagnetic spectrum containing wavelengths between 700nm and 1200nm.

NIR Plateau - the longer-wavelength spectral region adjacent to the red edge in which the NIR reflectance of foliar materials levels out at or near its maximum reflectance.

Pixels - the basic building blocks of digital images; picture elements.

Principal Components Analysis - a statistical transformation tool used to generate orthogonal channels or components that are more interpretable and dimensionally reduced with respect to the non-transformed data.

Red edge - the steep reflectance slope between high pigment absorption in the red-light zone and high cellular reflectance in the near-infrared zone.

Spectroradiometer - a laboratory or hand-held instrument that acquires light reflectance data in very narrow, contiguous bands across the visible and infrared portions of the electromagnetic spectrum.

SPOT - a commercial earth resource satellite remote sensing system (*Systeme Pour l'Observation de la Terre*) conceived and designed by the French Centre National d'Etudes Spatiales (CNES).

Supervised Classification - classification process in which informational categories are defined, labeled, and mapped when the spectral characteristics and/or location of informational classes are known prior to image classification through a combination of fieldwork, image analysis, and personal experience.

Unsupervised Classification - classification process in which informational categories are defined, labeled, and mapped with no extensive prior knowledge of the informational categories found in an image.

Visible Spectrum - that portion of the electromagnetic spectrum containing wavelengths between 400nm and 700nm.

Chapter 1: INTRODUCTION

1.1 Great Lakes Coastal Wetlands

Estimates indicate that 215 million acres of wetland habitat existed within the borders of the contiguous United States prior to European settlement (Roe et al., 1954; p. 501). Approximately 53% of this original acreage has been lost due to direct and indirect impact by humans (Dahl et al., 1991). Long thought of as wastelands, wetlands are now recognized as being vital to the health and stability of our ecosystems. The protection, restoration, and management of our nation's remaining wetlands are critical, because they play a vital role in energy fixation, nutrient assimilation, geo-chemical cycling, sediment stabilization, and wildlife habitat (Hardisky et al., 1986). Despite current progress in wetland protection and conservation, there are concerns that these efforts will fall far short of what is needed to maintain valued wetland functions (Zelazny and Feierabend, 1988). Freshwater wetlands are of added concern, for they represented ninety-eight percent of wetland losses that occurred between 1986 and 1997 (Dahl, 2000; p, 10).

In general, coastal wetlands can be described as ecotones, areas of transition between terrestrial (upland) and open water habitats (Cowardin et al., 1979; Chadde 1998; p. 2). Inherent to this landscape position is hydrologic

interaction with the physical, chemical, and biological components of the landscape. The presence of surface or near-surface water is a fundamental component to all wetlands, that creates the unique physiochemical and biological conditions that set wetlands apart from both terrestrial and open water environments (Mitsch and Gosselink, 2000; p. 107).

The Great Lakes contain approximately one fifth of the world's fresh water and, along with their connecting waterways, have approximately 15,000 kilometers of shoreline (Prince et al., 1992). There are approximately 1,200 km² of wetlands along the U.S. coastline alone, which represents only a small portion (approximately 30%) of the once expansive coastal marshes found in this area at the time of European settlement (Cardinale et al., 1998). The most common type of wetland found along the shorelines of the Great Lakes are coastal marshes, because the non-woody vegetation that typifies these areas best tolerates long-term and short-term water level fluctuations (Keddy and Reznicek, 1986). The remaining coastal marshes have largely been degraded by a multitude of environmental stressors, the majority of which are directly linked to the level of residential, industrial, and agricultural development in this region (Comer et al., 1995). Many Great Lakes coastal marshes are managed and protected by artificial dikes that serve to protect them from excessive flooding and wave action, as well as allow active water level management (Herdendorf, 1987).

Despite the reduced distribution and degraded nature of coastal Great Lakes wetlands, they are widely recognized as areas of concentrated biodiversity and productivity (Krieger, 1992). Great Lake wetlands represent, almost without exception, the most photosynthetically productive areas along the gradient from upland to open water (Wetzel, 1992). Wetlands are a critical component of the Great Lakes ecosystem, ultimately serving a wealth of physical, chemical, and biological functions that contribute to the region's environmental health. The annual economic value of Michigan's coastal wetlands, has been estimated at \$51.8 million with respect to fisheries, wildlife, and recreation (Jaworski and Raphael, 1979). This estimate was undoubtedly conservative, since it did not incorporate the value of less tangible functions such as flood mitigation, nutrient assimilation, and sediment stabilization. The protection and proper management of the remaining coastal wetlands are directly linked to the economic and cultural prosperity of the region (Raphael, 1987). Effective protection and restoration strategies for Great Lakes wetlands require knowledge of the nature of wetland health, loss, and degradation (Detenbeck et al., 1999).

Coastal Great Lakes wetlands are inherently dynamic, for they occupy the transitional boundary between dry land and open water. Coastal wetlands experience physical and environmental perturbations at a higher frequency than that typical of upland and open water habitats as a result of their

landscape position and exposure to large-lake processes (Maynard and Wilcox, 1997; p. 17). Coastal zone stressors, such as water-level fluctuations, currents, storms, ice, sedimentation, and erosion create an unstable and highly variable environment to which wetland plants have uniquely adapted (Keough et al., 1999). Wetland botanical diversity is reflective of, and dependent upon, a host of periodic stressors, especially those associated with water-level fluctuations (Keddy and Reznicek, 1986).

Hydrology is the single most important environmental determinant for establishing and maintaining wetland diversity and function, and hydrologic variability is the norm rather than the exception in most wetlands (Mitsch and Gosselink, 2000; p. 250). Individual plant species and plant assemblages display affinities and physiological adaptations for certain water-depth changes, the end result being a plant community that is continuously in a state of flux (Maynard and Wilcox, 1986; p. 27). Human and natural stressors continuously alter and reshape the mosaic of coastal wetland plant species, resulting in high spatial, temporal, and spatial variability. Different species are often distributed in rough zones that are determined by and distributed along coastal hydrologic gradients (Mitsch and Gosselink, 2000; p. 250). It is generally believed that spatially heterogeneous coastal marshes, those with a highly interspersed mosaic of plant species and open water areas, support a more diverse biotic community than homogeneous marshes (Gottgens et al., 1998;

Mitsch and Gosselink, 2000; p. 250). The dynamic nature of coastal environments and the inherent link of spatial heterogeneity to biotic diversity demands accurate and current wetland characterizations and inventories.

1.2 Wetland Remote Sensing

Since the vegetative community within a coastal wetland is shaped by environmental stressors, it follows that changes within a plant community would serve as an indicator of such perturbations. The natural and human induced stressors influencing Great Lakes coastal wetlands occur at various scales and can be found at the population, community, and landscape levels (Maynard and Wilcox, 1986; Pp. 36-40). Remote sensing and landscape ecology are powerful tools that provide a foundation upon which status and health assessments of Great Lakes coastal wetlands can be based (Wilcox, 1995).

Proper ground-based wetland characterization and inventory can be extremely difficult, time consuming, and inaccurate (Seher and Tueller, 1973). Many scientists have demonstrated that the need for cost-effective methods to inventory and monitor wetland areas necessitates the use of remote sensing techniques (Best et al., 1981; Carter and Anderson, 1982; Earnst-Dottavio et al., 1981; Gross and Klemas, 1986; Hardisky et al., 1986; Jensen et al., 1984; Oguma, 1996; and Stewart et al., 1980). Wetland remote sensing falls into two broad categories: vegetative mapping and the estimation of biophysical wetland

parameters (Gross et al., 1989; p. 475). Measurement of biophysical parameters involves the application of remote sensing data to determine characteristics such as plant biomass or percent cover. Mapping, the category explored in this research, primarily involves the delineation of wetland boundaries and the categorization of plant communities.

1.2.1 Biophysical Relationships

Energy across portions of the visible and non-visible electromagnetic spectrum, either emitted by the sun or generated by mankind, strikes and interacts with the landscape, including wetlands. The relative proportions of electromagnetic energy that are absorbed, transmitted or reflected will vary for different wetland cover types as a result of their structure, condition, or stage of life (Lillesand and Kiefer, 1994; p. 13). The foundation of wetland remote sensing is based on distinguishing features or cover-types within a wetland through the analysis of the electromagnetic energy reflected from substrates and/or vegetation.

Only a small segment of the electromagnetic spectrum is commonly utilized for wetland remote sensing, the visible and near-infrared portions of the spectrum. Energy in the blue (400-500nm), green (500-600nm), red (600-700nm) and near-infrared (700-1200nm) portions of the spectrum fall within the range of silicon-detector-based optical remote sensing and are most applicable

to wetland remote sensing. In general, the energy within these four broad wavelength domains is reflected by healthy, green vegetation in a characteristic pattern or spectral reflectance curve exemplified by the *Nuphar advena* curve shown in Figure 1.1. The spectral reflectance curves for three non-vegetative cover types are also shown in Figure 1.1: gravel, dead biomass, and clear water over a sand substrate. These non-vegetative signatures do not resemble the characteristic peak and valley configuration of the living vegetation curves. Vegetation (dead, dying and healthy), soil, and water are the three basic types of earth features (Lillesand and Kiefer, 1994; p. 17), all of which play a role in wetland remote sensing.

Three distinct regions exist within a typical vegetative spectral reflectance curve or spectral signature, the visible (400-700nm), red-edge (700-775nm), and NIR plateau (775-1200) (Lillesand and Kiefer, 1994; p. 18). Expression of reflectance as a percentage allows for a more accurate comparison of values generated under varied conditions. The relative combination of pigments (e.g. chlorophyll-a) present in live plant tissues largely dictates foliar reflectance in the visible range of the electromagnetic spectrum (Jensen, 2000; p. 337). Although most vegetative reflectance studies focus on the spectral nature of healthy, living plant tissue, spectral differences are present in green (living), dying, and necrotic (dead) plant materials (Figure 1.1). Dead biomass reflectance is significant in coastal wetlands because persistent plant species are

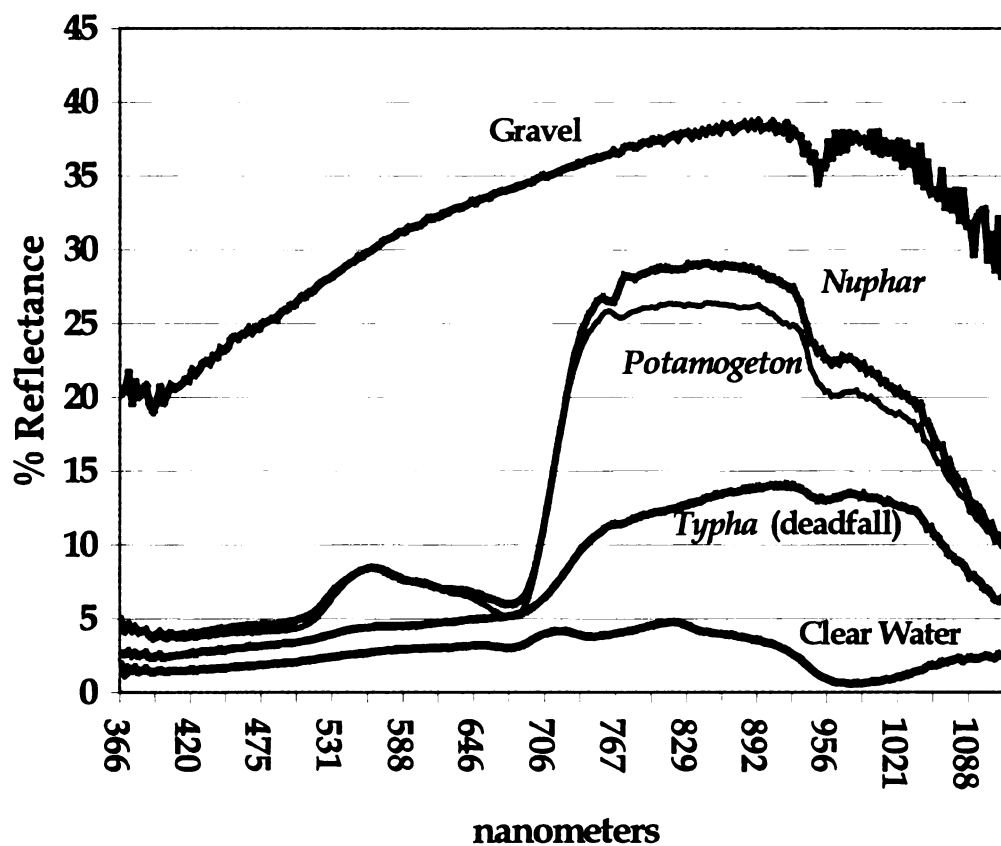


Figure 1.1. Five Characteristic Spectral Signatures

found in most coastal wetlands. Persistent vegetation are those plants whose dead biomass remains standing at least until the beginning of the following growing season (Cowardin et al., 1979). The relative proportion of green and dead/dying biomass varies with many wetland plant species, and the detection of related spectral differences may lead to better plant community discrimination (Elvidge and Portigal, 1990).

In general, the NIR portion of the spectrum can be divided into two regions. The region between 700 to 775nm is commonly termed the red edge or wall due to the marked change in reflectance by vegetation in this area (Figure 1.1). The NIR plateau is the spectral region adjacent to the red edge in which the NIR reflectance of foliar materials levels out at or near its peak (Figure 1.1). As NIR energy enters the mesophyll layer of a leaf, the air spaces and cellular membranes provide a multitude of surfaces through which NIR light is refracted. This is evident by the significant rise in reflectance in the infrared portion of the spectrum near 700nm (Figure 1.1). Intracellular and intercellular moisture content plays a secondary role in suppressing NIR reflectance of vegetation, because water absorbs nearly all NIR energy (Jensen, 2000; p. 342).

1.2.2 Aerial Photography of Wetlands

The photographic camera is certainly the oldest and most frequently used remote sensing instrument (Avery and Berlin, 1986; p. 21). Photography taken from an aircraft (aerial photography) represents the most common form of remote sensing applied to wetlands and it is well suited for general mapping strategies.

Aerial photography was commonly used as early as the 1950s as an upland land cover evaluation tool for natural vegetation and agricultural crops (Butera,

1983). Wetlands could be differentiated from similarly structured upland vegetation via infrared photography because hydrophytes tend to reflect higher levels of NIR energy, which prompted state and federal agencies to increasingly look towards aerial photography for the purposes of wetland mapping and inventory (Gross et al., 1989; p. 475).

Film types that are sensitive to NIR electromagnetic energy are generally preferred for wetland applications because they are more effective in detecting standing water and determining biomass, as well as differentiating wetland from upland vegetation (Hardisky et al., 1986). Black-and-white films are somewhat limited because the human eye is incapable of differentiating the full range of gray tones found in these panchromatic photographs (Lillesand and Kiefer, 1994; p. 79). The human eye is much more effective at differentiating the many hues on color films. Color infrared film (CIR) has emerged as the preferred wetland photographic media since it takes advantage of both the sensitivity to NIR and the increased tonal differentiation of color photography (Hardisky et al., 1986). Increased tonal differentiation is invaluable with respect to the botanical complexity and physical variation found in many coastal wetland areas. A host of state and federal agencies utilize CIR photography as the foundation of their wetland mapping strategies (Carter, 1982).

The image resolution of photographic systems is dictated by the physical size of the photo-reactive silver halide grains (50-100 micrometers), and is superior to digital remote sensing platforms (Avery and Berlin, 1986; p. 36). However, the non-digital format of photographic media limits its usefulness within computerized cartographic and geographic information systems (Hardisky et al., 1986).

As one would expect, there is less botanical detail in a photograph taken at 20,000 feet (smaller scale) than one taken at 5,000 feet (larger scale). The areal extent of the wetland to be photographed, the cost of photography, and the desired botanical detail ultimately determine the desired photographic scale. Photographs taken at 1:1,000-scale allow extremely accurate vegetation maps to be produced, but are 10 to 15 times more expensive than the same aerial coverage at 1:10,000-scale (Seher and Tueller, 1973). At scales of approximately 1:10,000, most large plant communities (25ft² or 2.3 m²) can be identified and mapped (Seher and Tueller, 1973).

Aerial photography (1:1,000 to 1:15,000 scales) has been found to be a fast, accurate, and relatively inexpensive method by which wetland boundaries, botanical changes, and areal extent can be recorded (Mitsch and Gosselink, 2000; p. 107). The two characteristics that limit the applicability of aerial photography to detailed vegetative mapping strategies are: 1) the limited

amount of spectral information (i.e. only three, wide sensitivity ranges) contained in each image (Jensen et al., 1984), and 2) its non-digital format (Hardisky et al., 1986). Spectral signatures like those shown in Figure 1.1 cannot be generated, or even approximated, via aerial photographs. If the assumption is made that more precise spectral reflectance data are needed to better differentiate wetland plant communities, photographs are not applicable to such methodologies.

1.2.3 Digital Wetland Imagery

The basic building blocks of digital images are pixels (picture elements), whose size is determined by both mission altitude and instantaneous field of view (IFOV). Along-track, digital imaging technologies are based on two-dimensional photosite arrays (Lillesand and Kiefer, 2000; p. 315) like those found in today's hand-held digital cameras. The 1st-dimension of such an array, comprised of a series of end-to-end photosites positioned perpendicular to the flight line, controls the swath width of the sensor. The 2nd-dimension, comprised of a series of end-to-end photosites positioned parallel to the flight line, relates to the spectral resolution of the instrument. Each photosite is a solid-state sensing device (CCD or CMOS) that responds to electromagnetic energies striking its surface by generating proportional electronic charges recorded for each pixel (Lillesand and Kiefer, 2000; p. 112). Arrays with well

over 1,000 photosites in the 2nd-dimension are operational today and are able to simultaneously record very small wavelength regions across much of the visible and NIR spectrum. Hundreds of 2nd-dimension pixels allow reflectance curves like those shown in Figure 1.1 to be captured.

Two-dimensional images are generated as the forward motion of the sensor positions the array so that data can be captured over adjacent portions of the landscape creating a ribbon-like image. Changing the elevation of a sensor with respect to a target changes the projected area of each photosite onto the target (i.e. ground resolution). Airborne platforms can yield a variety of spatial resolutions, determined by varying mission altitude (Equation 1.1).

$$D_{sp} = A * \beta \quad (\text{Eq. 1.1})$$

D_{sp} = Diameter equal to the spatial resolution (m) or height/width of pixel (m)

A = Mission Altitude (meters)

β = IFOV (radians)

1.2.4 Satellite Remote Sensing of Wetlands

In the early 1970s, the initial launch of the Landsat-1 satellite marked the practical beginning of spaceborne, earth resource remote sensing (Lillesand and Kiefer, 2000; p. 373). Over the ensuing thirty years, a variety of systems, with varied spatial and spectral resolutions, have been developed. Earth resource

satellite platforms are in continuous, circular orbits, a vantage point that provides near-simultaneous digital imagery over large geographic areas. Satellite platforms continue to provide an overwhelming array of earth resource data when fitted with remote sensing systems, and the status of these technologies continues to change as scientific advances yield improved spacecraft and sensors (Lillesand and Kiefer, 2000; p. 373). Although the rate of technological change is staggering, all current satellite-based systems display operational characteristics (Table 1.1) that significantly limit their applicability to detailed wetland remote sensing strategies. These limitations become obvious in the context of the two fundamental assumptions of this research: 1) the spatial heterogeneity of coastal wetlands is best captured by digital imagery with a spatial resolution at or below 5 meters (ITRES, 2000), and 2) separation of wetland plant communities is best achieved through the analysis of hyperspectral reflectance curves. If these assumptions are valid, then aerial photography and currently available satellite imagery are not applicable to detailed wetland mapping.

1.2.5 Airborne Hyperspectral Systems

The curves in Figure 1.1 are typical of the data generated by hand-held spectroradiometers acquiring data in many, very narrow, contiguous bands across the visible and infrared portions of the electromagnetic spectrum. Such spectroradiometric data have been used to discriminate earth surface features

<u>Satellite Systems</u>	<u>Wavelength</u>	<u>Pixel size</u>	<u>Band</u>
Landsat(4-5) MSS	500-600nm	79 x 79m	Band-1
	600-700nm	79 x 79m	Band-2
	700-800nm	79 x 79m	Band-3
	800-1100nm	79 x 79m	Band-4
Landsat TM (4-5)	450-520nm	30 x 30m	Band-1
	520-600nm	30 x 30m	Band-2
	630-690nm	30 x 30m	Band-3
	760-900nm	30 x 30m	Band-4
	1550-1750nm	30 x 30m	Band-5
	1040-1250nm	30 x 30m	Band-6
	2080-2350nm	30 x 30m	Band-7
Landsat-7 ETM+	450-520nm	30 x 30m	Band-1
	520-600nm	30 x 30m	Band-2
	630-690nm	30 x 30m	Band-3
	760-900nm	30 x 30m	Band-4
	1550-1750nm	30 x 30m	Band-5
	1040-1250nm	30 x 30m	Band-6
	2080-2350nm	30 x 30m	Band-7
	500-900nm	15 x 15m	Mono
SPOT	500-590nm	20 x 20m	Band-1
	610-680nm	20 x 20m	Band-2
	790-890nm	20 x 20m	Band-3
	510-730nm	10 x 10m	Mono
IKONOS	445-516nm	4 x 4m	Band-1
	506-595nm	4 x 4m	Band-2
	632-698nm	4 x 4m	Band-3
	757-853nm	4 x 4m	Band-4
	500-900nm	1 x 1m	Mono
<u>Aerial Photography</u>	<u>Wavelength</u>		
B&W Film*	300-720nm		
B&W Infrared*	300-960nm		
Color Film*	400-700nm		
Color Infrared Film*	400-900nm		
* = unfiltered			

Table 1.1. Instrument Spectral Sensitivities and Spatial Resolutions
(Source, Lillesand and Kiefer, 2000)

that exhibit diagnostic absorption and reflection patterns over narrow wavelength regions, patterns that are hidden or blurred in data collected at coarser spectral resolutions (Lillesand and Kiefer, 2000; p. 363). Hyperspectral sensors or imaging spectrometers record spectral data similar in nature to laboratory spectrometers, making it possible to construct spectral reflectance curves. The characteristic that exemplifies hyperspectral sensors is this inherent ability to create, or accurately approximate, a continuous spectral reflectance curve within a spectral domain most appropriate for a target of interest.

The visible and the NIR regions of the spectrum are most applicable to the spectral differentiation of vegetation. To have utility, a hyperspectral system would need to capture enough spectral information to effectively approximate a spectral signature across these regions. Examination of Figure 1.1 reveals substantial portions of all three vegetation curves in which the slope is essentially constant, and the data points found between the endpoints defining these regions of consistency are largely redundant. Therefore, the number of spectral bands needed to accurately approximate the spectral signature of vegetation can be reduced without adversely impacting our ability to differentiate targets based on spectral details. In order to better illustrate this idea, seven offset, spectral reflectance curves are presented in Figure 1.2. The original data set (bottom), captured by a hand-held spectroradiometer, is shown along with four other curves with synthetically reduced spectral

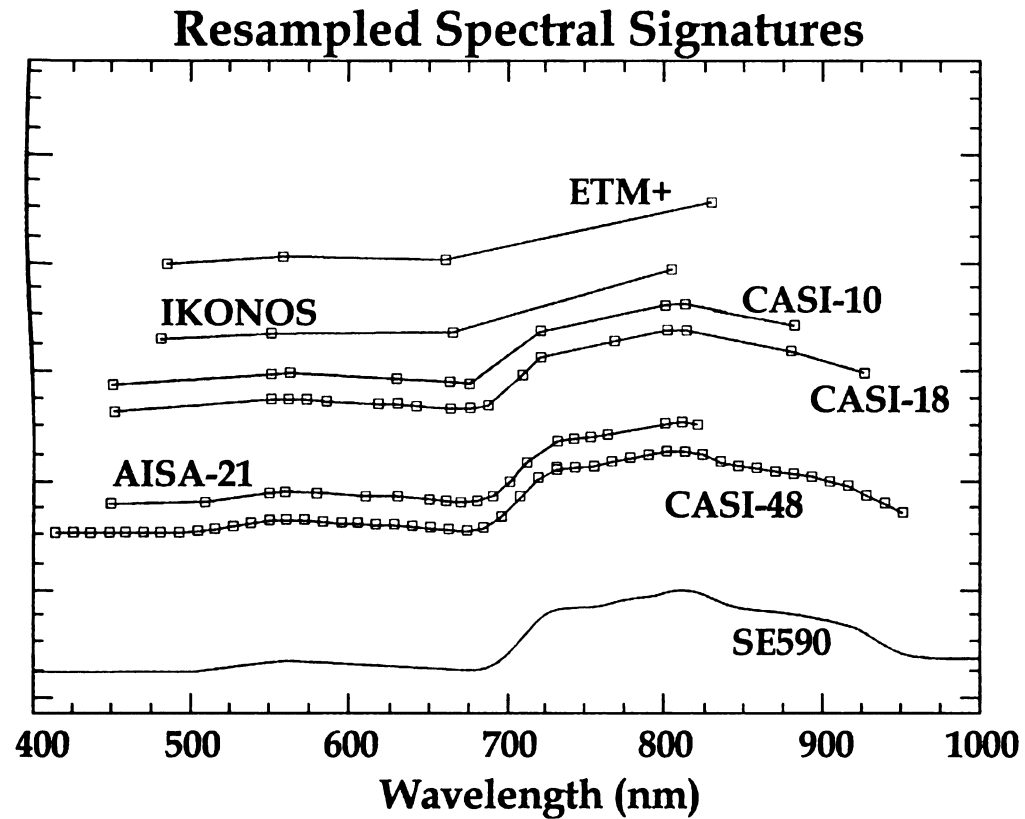


Figure 1.2 Synthetically Resampled Spectral Signatures

resolutions (CASI-48, AISA-21, CASI-18, CASI-10). Additionally, the visible and NIR bands of the IKONOS and LANDSAT-7 ETM+ instruments are depicted. Visually, there is little difference between the four curves of highest spectral resolution or band number. However, the two curves generated from satellite sensors poorly emulate the original data set. Much of the data recorded via the hand-held instrument is redundant, and can be effectively modeled with a significantly reduced bandset. Reduction in band number is significant because the constraints of current sensor technologies (i.e.

integration time) make it impossible to simultaneously record high spatial and high spectral detail.

The development of imaging spectrometers brought about increased interest in utilizing spectral reflectance data of vegetation canopies measured from the ground to aid in remotely differentiating plant species. The use of differences in canopy pigmentation and chemistry to classify to the species level has only recently emerged as a potentially new approach (Zarco-Tejada and Miller, 1999). Genera- or species-level vegetation differences are most frequent in the chlorophyll (visible) and water (NIR) absorption regions of the electromagnetic spectrum (Lillesand and Kiefer, 1994; p. 416). A major advantage of imaging spectrometry lies in the potential for integrated analysis comparing calibrated remote sensing imagery with field spectral measurements (Goetz, 1992; Kruse et al., 1993). A new era of wetland remote sensing began with the development of hyperspectral sensors capable of potentially exploiting detailed spectral characteristics as a means to better differentiate vegetation communities. Hyperspectral sensors provide data with superior spectral resolution, but spectral resolution alone does not effectively address coastal wetland remote sensing. In order for remotely sensed imagery to be truly useful in coastal environments, images must have a spatial resolution of 5 meters or less (ITRES, 2000). Currently, hyperspectral sensors are operational on several satellite platforms, and many more are expected to become

operational over the next decade. Although this is a major step forward in remote sensing, due to current technological constraints, satellite hyperspectral data can only be collected at spatial resolutions too coarse for detailed wetland mapping strategies.

Airborne sensors (photographic and digital) have several characteristics that make them effective remote sensing systems for wetland studies. Unlike orbital systems, airborne systems can be tasked when atmospheric and weather conditions are optimal. In addition, image capture can be timed to correspond with ecological (e.g. floods), phenological (e.g. flowering), or environmental (e.g. seiches) conditions. The ability to more easily dictate flight scheduling allows ground-based efforts, such as the placement of ground control targets, to be better coordinated with image data collection. Most importantly, airborne platforms can be flown at relatively low altitudes, a characteristic currently needed in order to simultaneously collect high spatial and high spectral resolution data.

Low-altitude, airborne, hyperspectral systems can provide the flexibility, spatial resolution, and spectral detail that are ideal for detailed wetland studies. Airborne hyperspectral sensors, when flown at altitudes appropriate for their IFOV, can acquire data with spatial resolutions below 1 meter. Such resolutions are comparable to those of 1:10,000 scale aerial photographs, making airborne

hyperspectral images a viable option to aerial photography even without considering the vastly improved spectral resolutions and digital format generated by such systems. The combination of hyperspectral sensors and light aircraft platforms resulted in a powerful tool for coastal wetland studies, one that provides the spatial, spectral and radiometric resolution needed to effectively study these environments.

1.2.6 Hyperspectral Wetland Applications

The combination of light aircraft and hyperspectral systems, which capture superior spectral and spatial resolutions, has been applied to a variety of remote sensing needs. Coastal applications have included, but are not limited to: water quality measurements, bathymetric charting, substrate mapping, coral reef monitoring, oil spill detection, and aquatic/terrestrial vegetation mapping (ITRES, 2000). Although applications specific to wetlands are not widespread in the literature, there are several examples of the use of airborne multi/hyperspectral sensors in these environments (Borstad Associates, 1995; Brown and Borstad, 1999; Forsyth et al., 1998; Jupp et al., 1994; Ritter and Lanzer, 1997; Savastano et al., 1984; Wang et al., 2000; Zacharis et al., 1992). Common to these investigations is the exploitation of improved spatial or spectral resolutions to more effectively differentiate wetland vegetation that is currently unattainable by other means. For example, Wang et al. (2000) mapped submergent and emergent macrophytes in Poyang Lake, China to an

accuracy estimated at 84 percent utilizing airborne hyperspectral imagery (3.75 meter pixels, 60 bands). This Poyang Lake study demonstrated that multi-species, botanical associations (e.g. Dense *Carex* Association, Reed Association) could be effectively mapped using hyperspectral images.

The wetland studies highlighted above, incorporating hyper/multispectral airborne sensors, illustrate several pertinent points. First, marine and estuarine settings represent the vast majority of wetland applications of airborne hyper/multispectral strategies currently reported in the literature. Second, although a limited number of freshwater studies incorporated in-situ reflectance data to aid in classification, few included detailed analysis of extensive species-level spectral libraries coupled with very high spatial resolution imagery (i.e. 1-meter pixels). Third, to my knowledge, multi/hyperspectral strategies have not been applied to the coastal wetlands of the Great Lakes. These deficiencies and the current need of many end-users for improved mapping of Great Lakes coastal resources provided the impetus for this research.

1.3 Study Sites

Lake Huron is the second largest of the Great Lakes, with an average surface area of 59,500 km² and 6,373 km of shoreline (IJC, 1993). In general, marsh and swamp wetland types are most commonly found along the shores of

Lake Huron (Maynard and Wilcox, 1997; p. 52), occupying a variety of environmental settings ranging from high energy, exposed shorelines to protected embayments associated with the numerous islands and peninsulas (Environment Canada, 1994). Complex wetland communities, some of national as well as global importance (Maynard and Wilcox, 1997; p. 52), are found along Lake Huron shorelines due to varied disturbance levels, varied hydro-geomorphology, and the presence of calcareous soils (Smith et al., 1991).

The Lake Huron basin and associated coastal areas, as well as the other four Great Lakes, have been subdivided into zones or eco-reaches (Figure 1.3) in which significant concentrations of similar wetland habitats are found (Chow-Fraser and Albert, 1998). These eco-reaches were delineated via differences in: climate, geology, hydro-geomorphology, and land use factors, differences that in combination dictate the development of wetlands with similar characteristics (Minc, 1997). Two wetland complexes, each from one of the ten distinct eco-reaches in Lake Huron, were selected as study sites for this investigation. The first study area is the Les Cheneaux Island complex, falling within the HG3 eco-reach, found along a stretch of shoreline that has some of the highest wetland density in northern Lake Huron (Koonce et al., 1999; p. 40). The second study area is the Wildfowl Bay Island complex, falling within the HG6 eco-reach, found along the southeastern shoreline of Saginaw Bay, Lake Huron.

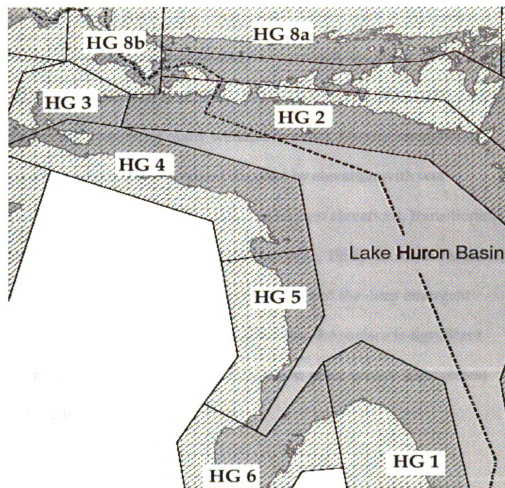


Figure 1.3. Lake Huron Ecoregions (from Koonce, et al., 1999)

1.3.1 Les Cheneaux Island Complex

The Les Cheneaux Islands are found within the most western portion of Lake Huron, located near the Straits of Mackinac, near the town of Hessel, Michigan. The marsh communities along the northern Lake Michigan/Huron shorelines are commonly found associated with sheltered embayments, environments providing protection not found along exposed, high-energy shorelines. An aerial view of the Les Cheneaux Islands reveals a maze of linear

waterways, islands, and peninsulas. In general, the wetlands in this area fall into two broad types, northern marsh and northern rich fen, albeit with considerable overlap (Koonce et al., 1999; p. 20). Both typically have vegetative zonal patterns characteristic of many wetland habitats. Species are generally distributed along a hydrologic gradient dictated by elevation with wet meadow/rich fen communities occupying the highest elevations, transitioning into shallow then deep emergent zones (Burton et al., 1999). In some instances, submergent plant species exist within and well beyond the deep emergent zone. The presence of limestone bedrock at or near the surface is significant because calcareous wetland soils develop that host plant species (calciphiles) indicative of such conditions.

The Prentiss Bay wetland (PBW) is located along the eastern boundary of the island complex, and is situated far back in a deep shoreline incision (Figure 1.4), bounded by Whitefish and Rover points. The embayment formed by these two peninsulas protects the shallow wetland from most wave energy, but waves generated by strong southeasterly winds can significantly influence the wetland. The PBW is relatively unusual in that route M-134 bisects the wetland parallel to the shoreline, and acts to roughly separate the wet meadow and emergent zones (Burton et al., 1999). The portion of the wetland north of the highway is typical of a northern wet meadow dominated by two sedge species, *Carex stricta* and *Carex lasiocarpa*, although several non-dominant species

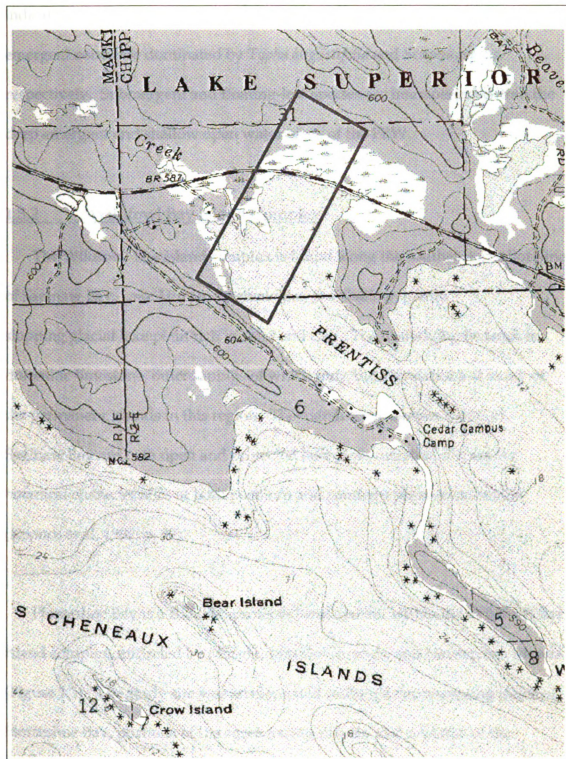


Figure 1.4 Prentiss Bay Image Area and Vicinity

indicative of a northern rich fen are interspersed. The shallow and deep emergent zones are dominated by *Typha angustifolia* and *Scirpus acutus*, respectively. Submergent and floating-leaf species are interspersed within the deep emergent and shallow open water areas of the PBW.

1.3.2 Wildfowl Bay Island Complex

The Wildfowl Bay island complex is found along the southeastern shoreline of Saginaw Bay, Lake Huron. Saginaw Bay is a shallow, gently sloping glacial lake plain rich in sand and clay. The underlying bedrock is dolomitic limestone, outcroppings of which form the foundations of many of the permanent islands in this region. The marsh communities found in Saginaw Bay are both open and protected lake plain marshes, displaying botanical characteristics of both northern and southern plant communities (Koonce et al, 1999; p. 20).

Horseshoe Bay is a shallow, protected embayment within the Wildfowl Bay island complex, encircled by Maisou, Middle Grounds, and Heisterman islands (Figure 1.5). The study site was an elongated rectangle encompassing much of Horseshoe Bay, portions of the surrounding islands, and a section of the mainland shoreline near the Geiger Road access site. During the 2000 growing season, due to extremely low water levels in Lake Huron, boat access to Horseshoe Bay was (at best) restricted to the narrow navigation channels.

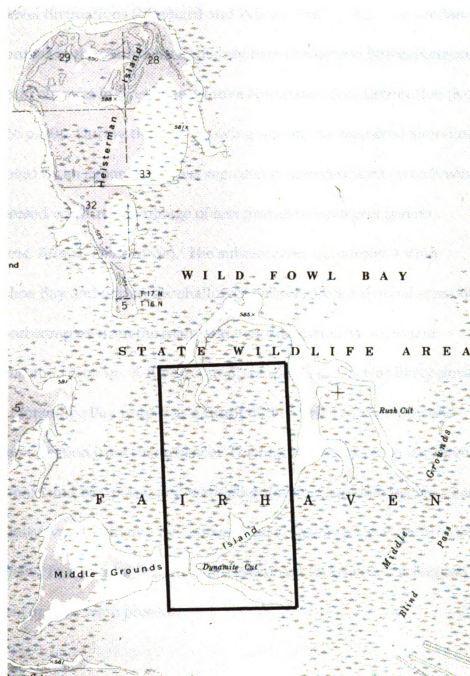


Figure 1.5. Horseshoe Bay Image Area (1- and 4-meter) and Vicinity

The shallow embayment wetlands of Saginaw Bay experience dramatic water-level fluctuations (Maynard and Wilcox, 1997; p. 52). The wetland plant communities in the study area and elsewhere in Saginaw Bay experience significant changes in overall vegetative abundance and distribution (Koonce et al., 1999; p. 20). During the 2000 growing season, the mainland shoreline was dominated by an expansive *Typha angustifolia* emergent zone, which was interspersed with an assemblage of less prevalent emergent genera (*Sagittaria*, *Alisma*, *Pontederia*). The submergent community within Horseshoe Bay and within the shallower portions of the channel separating the island complex from the mainland was dominated by *Vallisneria americana* and *Chara sp.* A diverse group of plant species was likely present within Horseshoe Bay proper as a result of the varied topography and relative protection from disturbance. The higher elevations on the islands were dominated by upland and wetland graminoids, while the emergent community was dominated by *Scirpus validus*, *Sagittaria rigida*, and *Typha angustifolia*. In addition, several floating leaf and less dominant shallow emergent species were present.

1.4 Statement of Problem

Strategies through which more accurate and detailed wetland maps could be produced would contribute to continued efforts to protect, monitor, and restore Great Lakes coastal wetlands. Technological advancements in sensor

and computer technologies have led to the development of the next generation of remote sensors. These hyperspectral systems are capturing imagery at spatial and spectral resolutions far superior to that available less than a decade ago.

The increased information content of high-resolution imagery should ultimately result in more accurate wetland mapping and monitoring strategies. This is based on the assumption that these new technologies help to improve the differentiation of coastal wetland plant communities. Thus, the first step is to explore if indeed botanical differentiation is improved via these technologies. Few studies have explored the potential benefits and pitfalls of applying high spatial and spectral resolution imagery to the characterization and mapping of freshwater coastal wetlands. Of the studies that have been conducted, even fewer have extensively explored the role of in-situ reflectance data and classification strategies with respect to the botanical differentiation of wetland plant communities. An exceptional opportunity exists to explore the application of high spatial and spectral resolution imagery in combination with radiometric field measurements in Great Lakes coastal wetlands.

The objectives of this research are to: 1) identify the best-performing image classification tool with respect to field-verified botanical regions of interest; 2)

quantitatively examine the properties of in-situ reflectance data to discern the optimal spectral framework for wetland imagery; and 3) quantitatively discern the optimal spatial framework for wetland imagery. These objectives will be addressed by 5 investigations grouped into three independent research components.

Research Component 1:

Identification of the best-performing image classification tool with respect to field-verified, botanical regions-of-interest (ROIs).

Investigation 1: Identification of the “best” method of classification via the direct comparison of the ISODATA, Spectral Angle Mapper, and Maximum-Likelihood classification results using image-based (Horseshoe Bay, 1-meter) training data.

Investigation 2: Comparison of the results from I-1 (ISODATA, SAM, and Maximum-Likelihood classifications of raw imagery) to similarly derived classifications based on Principal Components rotated imagery.

Investigation 3: Determination of the transferability of the “best approach” identified above (I-1 and I-2) via imagery taken at another location (Prentiss Bay), with a different sensor (AISA).

Research Component 2:

Quantitatively examine the properties of in-situ reflectance data to discern the optimal spectral framework for wetland imagery.

Investigation 4: Quantitative examine the properties of in-situ reflectance data to discern the optimal spectral framework for wetland imagery, to aid in the assessment of SAM and Maximum-Likelihood classification changes resulting from the manipulation of the spectral resolution of select imagery.

Research Component 3:

Quantitatively discern the optimal spatial framework for wetland imagery.

Investigation 5: Assessment of SAM and Mahalanobis-Distance classification changes resulting from the independent manipulation of the spatial resolution of select images.

Note: Images in this dissertation are presented in color.

Chapter 2: A Comparison of Image Classification Strategies to Optimize Wetland Botanical Differentiation.

2.1 Introduction and Rationale

In the 1970s, state and federal agencies increasingly looked towards aerial photography for the purposes of wetland mapping and inventory (Gross et al., 1989; p. 475). Film types that are sensitive to NIR electromagnetic energy are generally preferred for wetland applications because they are more effective in detecting standing water and determining biomass, as well as differentiating wetland and upland vegetation (Hardisky et al., 1986). Aerial photography (1:1000 to 1:15,000 scales) has been found to be a fast, accurate, and relatively inexpensive method by which wetland boundaries, botanical changes, and aerial extent can be recorded (Mitsch and Gosselink, 2000; p. 107). Two characteristics limit the applicability of aerial photography to detailed vegetative mapping strategies: 1) the limited amount of spectral information contained in each image (Jensen et al., 1986), and 2) its non-digital format (Hardisky et al., 1986).

The launch of the Landsat 1 satellite (i.e. 1970s) marked the practical beginning of spaceborne, earth resource remote sensing. Over the ensuing thirty years, a variety of systems, with varied spatial and spectral resolutions, have been developed. Orbiting satellite-based sensors do provide near-

simultaneous coverage of wetland imagery over large geographic areas recorded in digital format (Gross et al., 1989; p. 476). Satellite platforms continue to provide an overwhelming array of earth resource data when fitted with remote sensing systems, and the status of these technologies continues to change as scientific advances yield improved spacecraft and sensors (Lillesand and Kiefer, 2000; p. 373). However, regarding their utility for detailed wetland characterization, current systems are limited by their spatial and/or spectral resolutions. These limitations become obvious in the context of the two fundamental assumptions of this research: 1) the spatial heterogeneity of coastal wetlands is best captured by digital imagery with a spatial resolution of 5 meters or smaller, and 2) differentiation of wetland plant communities is best achieved through the analysis of hyperspectral (i.e. numerous narrow bands) reflectance records. Accepting these assumptions means that aerial photography and currently available satellite imagery are sub-optimal for detailed wetland mapping.

The development of imaging spectrometers created interest in utilizing spectral reflectance data of vegetation canopies measured from the ground to aid in remotely differentiating plant communities. Many next-generation, satellite-based systems (e.g. COIS, Hyperion, MODIS or Warfighter-1) incorporate hyperspectral sensors in order to address the spectral limitations of aerial photography and current satellites systems (ASPRS, 1995; Stoney and

Hughes, 1998; Thenkabail et al., 2000). A major advantage of imaging spectrometry lies in the potential for integrated analysis comparing calibrated remotely sensed imagery with field spectral measurements (Goetz 1992; Kruse et al., 1993). The use of systematic differences in canopy pigmentation and related chemistry to classify to the botanical species level has recently emerged as a promising new approach.

The development of new-age airborne and satellite-based imaging systems is making hyperspectral imagery more affordable and easier to obtain. Although not widespread, the wetland literature contains recent examples of investigations that utilized hyperspectral systems to map and monitor plant communities (Savastano et al., 1984; Zacharis et al., 1992; Forsyth et al., 1998; Borstad Associates, 1995; Jupp et al., 1994; Ritter and Lanzer, 1997; Brown and Borstad, 1999; Wang et al., 2000). Common to these investigations is the exploitation of improved spatial or spectral resolution to more effectively differentiate wetland vegetation.

The remote sensing community is hopeful that the improved resolving power of these hyperspectral (i.e. spatial, spectral, and radiometric) will lead to significant improvements in the differentiation of wetland plant communities, thereby improving coastal wetland mapping and monitoring efforts by

improving the accuracy of image classifications. One of the fundamental questions which remain unanswered is which image classification methodology is best suited for hyperspectral applications within the context of Great Lakes coastal wetlands. Answering this question is an important step needed to advance the application of hyperspectral imagery in coastal environments.

The goal of this component of my research is to perform a comparison of common classification methodologies in order to evaluate their ability to capitalize on the high spatial and spectral resolution of hyperspectral imagery. This goal addresses the first research objective outlined in Chapter 1 - identify the best-performing image classification tool with respect to the field-verified botanical regions-of-interest.

2.2 Methods

2.2.1 Airborne Image Acquisition

Two airborne imaging campaigns provided the digital imagery utilized throughout most of this research. On August 30, 1999, 3DI, Inc. (www.3dillc.com) captured airborne, digital imagery of the two study sites located in the Les Cheneaux Island complex (Appendix E; Figure E-1). The sensor utilized by 3DI, Inc. was the Airborne Imaging Spectrometer for Applications (AISA; www.specim.fi). Single-pass images (360 meters wide)

were collected over Prentiss and Mismar Bay, encompassing and roughly centered on previously established ecological transects (Gathman et al., 1999). Each of the 21-channel images were approximately 900 meters in overall length, extending from adjacent uplands, through the wetland proper and ending over open water (Figures 3.2 and 3.3).

On September 11, 2000, ITRES, Inc. (www.itres.com) captured digital imagery over the Horseshoe Bay study area (Appendix E; Figures E-2 and E-3). The sensor manufactured and deployed by ITRES Inc. was the second generation, Compact Airborne Spectrometric Imager (CASI-II). Both AISA and CASI-II are programmable, push broom, imaging spectrometers capable of being operated in spatial and spectral mode. ITRES, Inc. captured imagery in both spatial and spectral (hyperspectral) mode. The spatial extent of these images are large (2 km x 10 km) in comparison to the Les Cheneaux imagery, so the majority of my image analyses were performed on only the center portion of the imagery, largely Horseshoe Bay proper (Figure 1.5). This served two purposes: 1) it reduced the computation time needed to process and classify these image files, and 2) it eliminated the extraneous portions of the imagery where little or no ground control or field data were collected. Table 2.1 provides an overview of the AISA and CASI-II imaging and support systems, as well as a summary of basic flight parameters. The band center and Full-Width-Half-Maximum (FWHM) for each spectral band collected are

summarized in Table 2.2. Visual examination of a variety of spectral signatures from wetland plants provided the means by which band positions were strategically located throughout the visible and NIR regions of the spectrum for this 1-meter imagery. The 4-meter CASI-II imagery is truly hyperspectral, utilizing 48 contiguous, spectral bands across the NIR and visible wavelengths.

2.2.2 Image Geo-rectification

Both sets of imagery were delivered in geo-referenced format as a result of the on-board positioning technologies (GPS and Inertial Momentum) utilized by both imaging contractors. Both vendors indicated that the expected positional accuracy of their 1-meter imagery would be approximately 5-7 meters. At this level of image rectification, the spatial integrity of the in-situ data (i.e. sub-meter accuracies) would not be preserved. Thus, an in-house geo-rectification strategy was implemented.

Additional ground control points (GCPs) were identified at each of the study sites. Visually distinct features, such as pavement markings and culvert headwalls are ideal GCPs since they can be precisely located on the digital imagery. In areas where no infrastructure was present (i.e. Horseshoe Bay), white plywood GCP panels were installed in the wetland prior to the imaging

<u>Sensor</u>	<u>AISA</u>	<u>CASI-II</u>
Sensitivity Range	400-1000nm	400-1000nm
IFOV	1.0 milliradians	1.3 milliradians
Swath Width	360 pixels	512 pixels
Maximum # channels	288 bands	288 bands
Radiometric Res.	16 bit	12 bit
@ 1 meter pixels	21 bands	18 bands
@ 4.0 meter pixels	n/a	48 bands
<u>Horseshoe Bay (1m-CASI-II)</u>		
Date		9/11/00
Start time (HBW path 1)		12:21pm
Sun angle (HBW path 1)		52.0 degrees
Start time (HBW path 2)		1:06pm
Sun angle (HBW path 2)		51.3 degrees
Start time (HBW path 3)		1:16pm
Sun angle (HBW path 3)		50.8 degrees
Start time (HBW path 4)		1:26pm
Sun angle (HBW path 4)		50.2 degrees
<u>Horseshoe Bay (4m-CASI-II)</u>		
Date		9/11/00
Start time		12:54pm
Sun angle		51.7 degrees
<u>Les Cheneaux (1m-AISA)</u>		
Date		8/30/99
Start time (MBW)		12:18pm
Sun angle (MBW)		48.1 degrees
Start time (PBW)		12:49pm
Sun angle (PBW)		48.2 degrees

Table 2.1. Instrument Specifications and Flight Parameters.

CASI-II <u>48 band</u>	FWHM <u>4m</u>	AISA <u>21 Band</u>	FWHM <u>1m</u>	CASI-II <u>18 band</u>	FWHM <u>1m</u>
414.3	5.7	448.81	n/a	450.5	16
425.4	5.7	508.79	9.73	549.7	6.8
436.5	5.7	549.32	9.73	561	4.9
447.7	5.7	559.17	10.14	572.4	6.8
458.8	5.8	579.45	10.14	584.7	5.8
470	5.8	609.87	10.14	617.9	6.8
481.2	5.8	630.15	10.14	630.2	5.9
492.4	5.8	650.43	10.14	641.6	5.9
503.6	5.8	660.57	10.14	663.6	6.8
514.9	5.8	670.71	10.14	676	5.9
526.2	5.8	680.85	10.14	687.5	5.9
537.5	5.8	690.99	10.14	708.5	5.9
548.8	5.8	701.13	10.14	721	6.9
560.1	5.8	711.97	10.56	767.1	6.9
571.4	5.8	731.33	10.56	800.8	5.9
582.8	5.8	741.89	10.56	813.3	6.9
594.1	5.8	752.45	10.56	880.9	6.9
605.5	5.8	763.01	10.56	927.3	6.9
616.9	5.9	799.97	10.56		
628.3	5.9	810.53	10.56		
639.7	5.9	821.09	10.56		
651.2	5.9				
662.6	5.9				
674.1	5.9				
685.5	5.9				
697	5.9				
708.5	5.9	***CASI-II 48 band			
720	5.9	***continued			
731.5	5.9	847.1	5.9		
743	5.9	858.7	5.9		
754.6	5.9	870.3	5.9		
766.1	5.9	881.9	5.9		
777.7	5.9	893.4	5.9		
789.2	5.9	905.1	5.9		
800.8	5.9	916.7	5.9		
812.3	5.9	928.3	5.9		
823.9	5.9	939.9	5.9		
835.5	5.9	951.5	5.9		

Table 2.2. Instrument Bandsets with FWHM

CASI-II	FWHM	IKONOS	FWHM
<u>10 Band</u>	<u>60cm</u>	<u>4 band</u>	<u>4m</u>
449.5	15	480.5	71
549.7	6.8	550.5	89
562	5.8	665	66
629.3	6.8	805	96
663.6	6.8		
676	5.9		
721	6.9		
799.8	6.9		
812.3	5.9		
882.8	6.9		

Table 2.2. Continued

overpass. Sub-meter RT-DGPS positions were recorded for all GCP locations. These GPS data were exported via Trimble Pathfinder Office software into Arcview shapefiles. The GCPs provided an adequate distribution of control points to yield sub-pixel image rectification at each study site. The Image-to-Map Rectification module in the ENVI software provides a dual screen interactive tool by which images can be geo-rectified. A series of rectification pairs were created by visually selecting a GCP position on the image that was then linked to its appropriate location as recorded via the RT-DGPS. Once all of the viable rectification pairs were selected, an RST (Rotation-Scaling-

Translation), nearest neighbor rectification was performed. RST interpolation utilizes a linear (first-order polynomial), least-squares procedure to model spatial image corrections (Jensen, 1996. p. 127). This nearest neighbor method of intensity interpolation was chosen for two reasons: 1) the original input pixel values were not altered, and 2) the maximum spatial shift associated with any one input pixel would be one-half pixel, comparable to the sub-pixel accuracies associated with the in-situ data (Lillesand and Kiefer, 2000. p. 530).

The overall effectiveness of an image-to-map rectification can be expressed as a total root-mean-square error (RMSE), which is the average of all residual linear distances remaining between image positions and their paired GCT/GCP locations after completion of the rectification process. In this research, a total RMSE at or below the nominal pixel size of the imagery was desired and achieved (Table 2.3) so that the sub-pixel accuracies associated with the in-situ data could be effectively compared to the imagery at the pixel level.

2.2.3 Imagery Percent Reflectance Transformation

The baseline image data were recorded as raw radiance values, creating the need to transform the digital number associated with each pixel into relative percent reflectance. Generally, calibration surfaces used in such transformations need to be at least ten times larger than the nominal spatial resolution (pixel size) of the imagery. Large, homogeneous gravel parking

<u>Horseshoe Bay (1-meter data)</u>				
Total RMSE: 0.796261				
RST/Nearest Neighbor Resampling				
<u>GCP#</u>	<u>(Image X,Y)</u>	<u>(Predict X,Y)</u>	<u>(Error X,Y)</u>	<u>(RMSE)</u>
#1	(1526.50,4610.05)	(1527.08,4609.93)	(0.58,-0.12)	-0.59
#2	(1013.50,4966.45)	(1013.28,4966.50)	(-0.22,0.05)	-0.22
#3	(1671.45,5844.50)	(1670.03,5844.80)	(-1.42,0.30)	-1.46
#4	(1125.50,6143.50)	(1125.86,6143.42)	(0.36,-0.08)	-0.37
#5	(1862.50,6432.50)	(1863.20,6432.35)	(0.70,-0.15)	-0.72
<u>Horseshoe Bay (4-meter data)</u>				
Total RMSE: 0.288911				
RST/Nearest Neighbor Resampling				
<u>GCP#</u>	<u>(Image X,Y)</u>	<u>(Predict X,Y)</u>	<u>(Error X,Y)</u>	<u>(RMSE)</u>
#1	(414.45,1277.45)	(414.12,1277.57)	(-0.33,0.12)	-0.36
#2	(449.64,1372.64)	(450.07,1372.48)	(0.43,-0.16)	-0.46
#3	(284.45,1366.45)	(284.54,1366.42)	(0.09,-0.03)	-0.1
#4	(449.45,1586.45)	(449.20,1586.54)	(-0.25,0.09)	-0.26
#5	(498.55,1732.45)	(498.61,1732.43)	(0.06,-0.02)	-0.06
<u>Prentiss Bay</u>				
Total RMSE: 0.931855				
RST/Nearest Neighbor Resampling				
<u>GCP#</u>	<u>(Image X,Y)</u>	<u>(Predict X,Y)</u>	<u>(Error X,Y)</u>	<u>(RMSE)</u>
#1	685.50,518.50)	(684.78,518.32)	(-0.72,-0.18)	0.74
#2	680.50,536.50)	(680.65,536.39)	(0.15,-0.11)	0.19
#3	668.00,553.45)	(668.59,554.10)	(0.59,0.65)	-0.88
#4	416.05,593.21)	(415.44,593.52)	(-0.61,0.31)	0.69
#5	420.00,593.47)	(420.37,594.40)	(0.37,0.93)	1
#6	516.67,628.11)	(516.31,627.52)	(-0.36,-0.59)	0.69
#7	520.06,628.11)	(520.10,628.17)	(0.04,0.06)	0.07
#8	518.75,606.25)	(518.10,605.91)	(-0.65,-0.34)	-0.74
#9	521.00,606.75)	(521.90,606.46)	(0.90,-0.29)	0.95
#10	(519.25,617.50)	(519.38,617.08)	(0.13,-0.42)	0.44

Table 2.3. Image Rectification Summary.

#11	(679.50,670.25)	(678.92,670.40)	(-0.58,0.15)	0.6
#12	(682.77,672.23)	(684.06,672.13)	(1.29,-0.10)	1.3
#13	(616.46,716.31)	(615.43,715.28)	(-1.03,-1.03)	1.46
#14	(623.50,729.00)	(624.12,729.34)	(0.62,0.34)	0.7
#15	(551.15,699.92)	(550.37,701.10)	(-0.78,1.18)	1.42
#16	(377.00,718.00)	(377.80,717.07)	(0.80,-0.93)	1.22
#17	(398.44,888.22)	(397.31,888.08)	(-1.13,-0.14)	1.14
#18	(404.22,883.22)	(405.21,883.72)	(0.99,0.50)	1.11

Table 2.3. Continued

areas were present in both the Horseshoe Bay and Prentiss Bay imagery. These areas served as ground-based calibration surfaces through which image radiance data were transformed into absolute reflectance.

In order to derive a reflectance coefficient (ρ^a) for the gravel calibration surface within the Prentiss Bay imagery, near simultaneous, SE-590 measurements were taken of it ($E_{\uparrow\text{gravel-pbw}}$) and the in-situ reference panel ($E_{\uparrow\text{msu}}$) under cloudless skies. The gravel SE-590 radiance measurements ($E_{\uparrow\text{gravel-pbw}}$ and $E_{\uparrow\text{msu}}$) were recorded several weeks prior to the imaging overpass at Prentiss Bay. Although it was my intent, it was not possible to capture gravel reflectance data during the Prentiss Bay imaging overpass because 3DI, Inc. flew the mission during an unexpected break in cloud cover. The moisture level within the gravel region was similar during both the imaging overpass and the in-situ measurements, allowing the previously

collected reflectance data to be utilized. The near-simultaneous SE-590 measurements of the gravel and reference panel radiance allowed $\rho^a_{\text{gravel-pbw}}$ to be calculated with Equation 2.1.

$$\rho^a_{\text{gravel-pbw}} = E\uparrow_{\text{gravel-pbw}} / E\uparrow_{\text{msu}} * \rho^a_{\text{msu}} \text{ (for bands 1 through 252)} \quad (\text{Eq. 2.1})$$

$E\uparrow_{\text{gravel-pbw}}$	=	Prentiss Bay gravel radiance
$E\uparrow_{\text{msu}}$	=	In-situ reference panel radiance
$\rho^a_{\text{gravel-pbw}}$	=	Prentiss Bay gravel reflectance coefficient
ρ^a_{msu}	=	In-situ reference panel reflectance coefficient

A similar procedure was followed in order to derive a reflectance coefficient ($\rho^a_{\text{gravel-hbw}}$) for the gravel calibration surface within the Horseshoe Bay imagery (Equation 2.2). Members of the ITRES Inc. field crew captured a series of gravel ($E\uparrow_{\text{gravel-hbw}}$) and Spectralon ($E\uparrow_{\text{spec}}$) radiance measurements using an ASD FieldSpec-Jr spectroradiometer at Horseshoe Bay during the imaging campaign.

$$\rho^a_{\text{gravel-hbw}} = E\uparrow_{\text{gravel-hbw}} / E\uparrow_{\text{spec}} * \rho^a_{\text{spec}} \text{ (for bands 1 through 252)} \quad (\text{Eq. 2.2})$$

$E\uparrow_{\text{gravel-hbw}}$	=	Horseshoe Bay gravel radiance
$E\uparrow_{\text{spec}}$	=	Spectralon reference panel radiance
$\rho^a_{\text{gravel-hbw}}$	=	Horseshoe Bay gravel reflectance coefficient
ρ^a_{spec}	=	Spectralon reflectance coefficient

In order to create reflectance coefficient values appropriate for each image bandset, $\rho^a_{\text{gravel-pbw}}$ and $\rho^a_{\text{gravel-hbw}}$ were spectrally resampled into the bandsets shown in Table 2.2 to yield three synthetic reflectance coefficients, ρ^a_{AISA} ,

$\rho^{a_{\text{CASI118}}}$ and $\rho^{a_{\text{CASI48}}}$. These values, which corresponded well with published gravel reflectance values (Bowker et al., 1985, Clark et al., 1993), range from approximately 15 to 40 percent across the wavelength domain of both the AISA and CASI-II instruments.

The gravel calibration surfaces were among the brightest features (highest reflectance) throughout the spectral range of the imagery. Two Regions-of-Interest were delineated that encompassed the areas over which the in-situ radiance data ($E_{\uparrow_{\text{gravel-hbw}}}$ and $E_{\uparrow_{\text{gravel-pbw}}}$) were captured. The band-specific mean reflectance (i.e. $E_{\uparrow_{\text{mean-pbw}}}$, and $E_{\uparrow_{\text{mean-hbw}}}$) and associated standard deviation (i.e. $E_{\uparrow_{\text{std-pbw}}}$, and $E_{\uparrow_{\text{std-hbw}}}$) were extracted using the ENVI Region of Interest (ROI) module for the Prentiss and Horseshoe Bay gravel ROIs. The band-specific standard deviation values were all at or below five percent. Generally, calibration surfaces are considered homogeneous, flat reflectors if their associated standard deviations are less than five percent. The technical specifications for the well-calibrated Landsat 7, ETM+ imager requires a radiometric precision of +/-5 percent.

The division of each band-specific $E_{\uparrow_{\text{mean}}}$ value by its band-specific reflectance coefficient (i.e. $\rho^{a_{\text{AISA}}}$, $\rho^{a_{\text{CASI118}}}$ or $\rho^{a_{\text{CASI48}}}$) generated radiance values ($E_{\uparrow_{100}}$) equivalent to those expected from a calibration panel exhibiting 100 percent reflectance, and quantified the total per band irradiance striking the

two gravel calibration surfaces. A pseudo-calibration surface was then created within the “no-data” region of each image by interactively typing in these band specific E_{100} values within the ENVI Spatial Pixel Editor. The resulting cluster of pixels was easily identified against the backdrop of the solid black “no-data” region of each image. Based on the assumption that the now quantified irradiance (E_{100}) values are constant within any one band and image, percent reflectance values were calculated for each image pixel by dividing the radiance value recorded in each (E_{pixel}) by the appropriate, band-specific, pseudo-calibration (E_{100}) value utilizing the ENVI Flat Panel Calibration module. An example of the series of calculations utilized to transform the raw pixel radiance values into absolute percent reflectance for the Prentiss Bay imagery is summarized in Table 2.4.

2.2.4 Imagery Principal Components Rotation

In remote sensing, feature extraction involves the identification of those statistical characteristics of the remotely sensed data that capture the most systematic variation (Campbell, 1996; p. 288). Systematic variations, as opposed to non-systematic variations and/or data noise, ultimately provide the foundation upon which remote sensing targets are differentiated. A feature-extraction tool commonly applied throughout the scientific community is Principal Components Analysis (PCA). PCA has been used to generate orthogonal channels or components that are more interpretable and

Band	$E\uparrow(\text{mean})$	Rho $\rho_a(\text{AISA})$	$E\uparrow100$ $E\uparrow(\text{mean})/\rho_a(\text{AISA})$	$E\uparrow\text{pixel}$ (e.g.)	%or (*100) $(E\uparrow\text{pixel}/E\uparrow100)$
1	7864	0.9077	8663.52	89	1.03
2	12753	0.9223	13827.46	214	1.55
3	13701	0.9264	14788.92	689	4.66
4	13523	0.9268	14591.66	703	4.82
5	13207	0.9292	14213.24	558	3.92
6	12651	0.9305	13595.55	409	3.01
7	11806	0.9306	12686.71	324	2.55
8	11306	0.9308	12146.91	255	2.10
9	11376	0.9305	12225.32	223	1.82
10	11438	0.9313	12281.23	197	1.60
11	11123	0.9312	11945.10	204	1.70
12	9702	0.9307	10424.68	289	2.78
13	10197	0.9305	10959.21	626	5.71
14	10125	0.9302	10884.50	1158	10.63
15	8861	0.9282	9546.72	2245	23.52
16	9573	0.9275	10321.42	3072	29.77
17	9504	0.9273	10248.72	3428	33.44
18	5833	0.9256	6302.10	2248	35.67
19	8051	0.9236	8716.95	3298	37.83
20	7686	0.9227	8330.25	3150	37.82
21	6330	0.9225	6861.95	2606	37.98

Table 2.4. Image Percent Reflectance Methodology

dimensionally reduced with respect to the raw imagery (Jensen, 1996; p. 518; Singh and Harrison, 1985; and Kauth and Thomas. 1976). PCA has also been used to address a fundamental problem with multi/hyperspectral imagery -- extensive inter-band correlation or data redundancy (Lillesand and Kiefer, 2000; p. 518). The goal of image-based PCA is to compress all of the information (correlation/variance) contained in an original image into fewer, independent (orthogonal) channels or principal components. If the vast majority (>99%) of

the meaningful variance were compressed into relatively few, uncorrelated dimensions, the efficiency of image processing and classification would be greatly increased through referencing these dimensions instead of the original data. A detailed description of the statistical framework used to perform PCA is beyond the scope of this research, but a more complete explanation can be found in Davis (1986).

The baseline Prentiss and Horseshoe Bay imagery were transformed into their principal components via ENVI's Image Transformation module (Appendix E; Figures E-4 and E-5, respectively). Covariance-based image transformations are the norm because they focus on major target differences, resulting in more "class" separation. During preliminary PCA runs, the number of dimensions generated was set equal to the number of bands associated with the imagery. Beginning with the first dimension, each was systematically displayed in order to visually assess their spatial coherence. Those dimensions that displayed little spatial coherence (salt-and-pepper images) were deemed non-meaningful due to the random distribution of the data (i.e. noise) information contained in that dimension. Based on these efforts, it was determined that 6 dimensions regularly contained meaningful (i.e. spatially coherent) data within this research as shown in Figure 2.1.

A final PCA rotation was completed on the Prentiss Bay 1-meter, 1-Horseshoe Bay 1-meter and Horseshoe Bay 4-meter images, yielding a single output file containing six components (Figure 2.1). The statistics files associated with each PCA run are presented in Appendix A. Greater than 99% of the original variance is captured in the first six components of each PC image set, indicating that the dimensionality of the original imagery had been effectively reduced into these few, independent data channels. Often, false-color images generated from combinations of components depict more subtle differences in color shading and distribution than traditional color-composite images (Jensen, 1996, page 179). Dimensions 2, 3, and 4 did the best job of visually enhancing the botanical differences found within the Prentiss and Horseshoe Bay imagery.

2.2.5 Accuracy Assessment Regions-of-Interest

In-situ reflectance measurements were collected for the predominant species, species assemblages, and cover types at the Prentiss and Horseshoe Bay study sites. Care was taken to ensure that each measurement was at the approximate center of a botanically homogeneous region covering multiple image pixels. A real-time, differentially corrected GPS (RT-DGPS) receiver was used to record the approximate center and boundary of each region to sub-meter accuracies, providing the bulk of the ground-truth botanical data utilized for classification accuracy assessments. Additional field-verified locations were delineated within the Horseshoe Bay imagery that were not recorded during

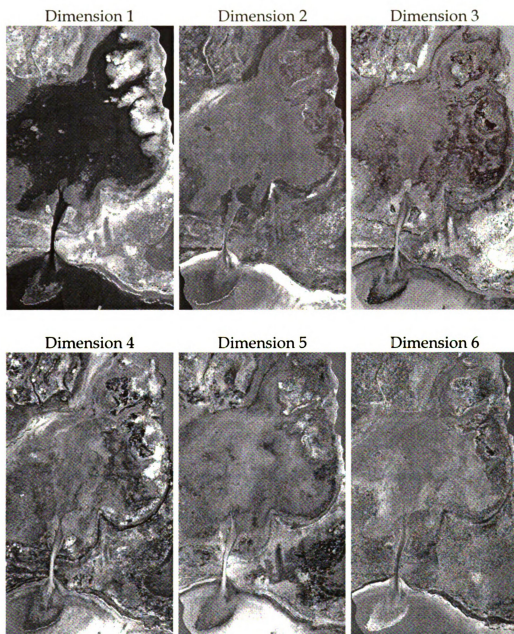


Figure 2.1. Horseshoe Bay; Dimensions 1-6 PCA Images

initial site visits. The accuracy assessment/training regions used throughout Investigations 1 through 3 are shown in Tables 2.5 and 2.6. In addition, the locations of the training ROIs shown in Table 2.6 are displayed on Figure E-2, Appendix E.

Each image-based ROI was further divided into an easterly and westerly region. This division created two adjacent ROIs, each representing the spectral characteristics of the original ROI from which they were derived, and independently provided both training (i.e. supervised classification) and accuracy assessment pixels. Classification results were compared via confusion matrix parameters (e.g. Kappa Coefficients) that were generated with the ENVI Post-Classification module with respect to the easterly ground-truthed ROIs.

The accuracy assessments utilized in this research are based solely on the botanical ROIs summarized in Table 2.5 and 2.6. Ideally, the entire wetland would have been ground-truthed allowing a more formal, randomly generated, accuracy assessment (i.e. 1% of pixels) to be applied across the entire image. Such an approach was logistically impossible. However, the ROI-based accuracy assessments presented in this research remain valid as well as relevant because they allow multiple classification results to be compared with respect to their ability to differentiate known botanical communities.

<u>ROI</u>	<u>Matrix Code</u>	<u>Scientific Name</u>	<u>Pixel #</u>
1:	Stricta	<i>Carex stricta</i>	68
2:	stricta50/lasiocarpa50	<i>C. stricta/Carex lasiocarpa</i>	46
3:	lasio/acutus10	<i>C. lasiocarpa/Scirpus acutus</i>	44
4:	lasio/typha50	<i>C. lasiocarpa/Typha</i>	40
5:	roadside-veg	<i>n/a</i>	48
6:	asphalt	<i>n/a</i>	50
7:	typha80	<i>Typha Angustifolia</i>	62
8:	acutus50/typha50	<i>T. angustifolia/S. Acutus</i>	56
9:	acutus40/soil60	<i>Vallisneria Americana</i>	46
10:	Dolomite	<i>n/a</i>	44
11:	Chara	<i>Chara sp.</i>	44
12:	Soil70/typha15/acutus15	<i>T. angustifolia/S. Acutus</i>	42
13:	Nuphar-12in	<i>Nuphar advena</i>	44
14:	Potamogeton-15i	<i>Potamogeton natans</i>	44
15:	2muck-20cm	<i>n/a</i>	56
16:	acutus-sparse	<i>Scirpus acutus</i>	50
17:	vallisneria	<i>Vallisneria Americana</i>	94
18:	pine	<i>Pinus sp.</i>	50
19:	shadow	<i>n/a</i>	46
20:	acutusclumps-dense	<i>Scirpus acutus</i>	100

Table 2.5. Prentiss Bay Regions-of-Interest.

2.2.6 Image Classifications

Image classification, both supervised and unsupervised, is the process of establishing a link between an informational category of interest and a related spectral class. Unsupervised classification is based on the fact that most remotely sensed images are composed of spectral classes that are reasonably uniform with respect to reflectance (brightness) across one or more spectral channels, and can therefore be defined, labeled, and mapped (Campbell, 1996;

<u>ROI</u>	<u>Matrix Code</u>	<u>Scientific name</u>	<u>Pixel #</u>
1:	Chara	<i>Chara sp.</i>	96
2:	phragmites-clump	<i>Phragmites australis</i>	100
3:	scival-dense	<i>Scirpus validus</i>	108
4:	scirpusclump	<i>Scirpus validus</i>	100
5:	typha-soil2	<i>Typha angustifolia</i>	100
6:	sagrigida60/40	<i>Sagittaria rigida</i>	52
7:	beach sand	n/a	54
8:	shallowh20/sand	n/a	80
9:	Hetdub	<i>Heteranthera dubia</i>	66
10:	Sagrigida	<i>Sagittaria rigida</i>	84
11:	valisneria	<i>Vallisneria americana</i>	72
12:	deeph20	n/a	94
13:	scivalbrown	<i>Scirpus validus</i>	62
14:	leersia	<i>Leersia oryzoides</i>	54
15:	muck	n/a	54
16:	saggram/chara	<i>Sagittaria graminea/Chara sp.</i>	60
17:	Typhah20	<i>Typha angustifolia</i>	64
18:	Nuphar	<i>Nuphaadvena</i>	164
19:	Eleocharis	<i>Eleocharis sp.</i>	88
20:	Impatiens	<i>Impatiens capensis</i>	200
21:	bluejoint	<i>Calamagrostis canadensis</i>	232
22:	cutgrass-eleocharis	<i>L. oryzoides</i>	226
23:	Eleocharis-sand	<i>Eleocharis sp.</i>	50
24:	typha-phrag-scivalmix	<i>Typha/Phragmites/Scirpus</i>	90

Table 2.6. Horseshoe Bay, 1-meter Regions-of-Interest.

p. 318). The primary advantage of all unsupervised classification strategies is that no extensive prior knowledge of the informational categories found in an image is required.

In supervised classification, on the other hand, the spectral characteristics and/or location of informational classes are known prior to image classification through a combination of fieldwork, image analysis, and personal experience (Jensen, 1996; p. 197). The major advantage of supervised classifications is that the spectral classes can be tailored to the desired informational categories (Campbell, 1996; p. 328). A major disadvantage of a supervised classification is that a fixed classification structure is imposed on the data, one that may not match the natural classes that exist within the n-dimensional data space of the imagery (Campbell, 1996; p. 328).

2.2.6.1 ISODATA Classification (Investigation 1)

The unsupervised classification tool used in component one of this research was the ISODATA (Iterative Self-Organizing Data Analysis Technique) classifier available in the ENVI Classification module (Jain, 1989; Sabins, 1987; Tou and Gonzalez, 1974). It is an iterative process that begins by initially establishing a minimum and maximum number of spectral class centroids that are evenly distributed throughout the n-dimensional (n = number of bands) data space (RSI, 1999; p. 560). A 48 class ISODATA classification was generated

from the Horseshoe Bay, 1-meter imagery using the parameters shown in Figure 2.2. The 24 regions-of-interest summarized in Table 2.6 were used as ground-truth data to which the ISODATA results were compared.

In most instances, there were only one or two ISODATA clusters that captured the vast majority of any particular ground-truth class. When faced with class overlap, the ISODATA cluster was assigned to the ground-truth class having the largest proportion of pixels within the cluster. This labeling prioritization method ensured that the final cluster assignments represented the best possible classification (i.e. highest possible percent correctly classified). Upon completion of all class assignments the confusion matrix parameters referenced in the results section of this chapter were generated. The evaluation of one or more confusion matrix parameters allowed the performance (ROI botanical accuracy) of the ISODATA classification of the Horseshoe Bay, 1-meter image to be assessed and compared to similar Maximum-Likelihood and SAM classifications.

2.2.6.2 Maximum-Likelihood Classification (Investigation 1)

The first of two supervised classification tools used in this component of the research was the Maximum-Likelihood classifier available in the ENVI Classification module. Maximum-Likelihood decision rule values range from 0

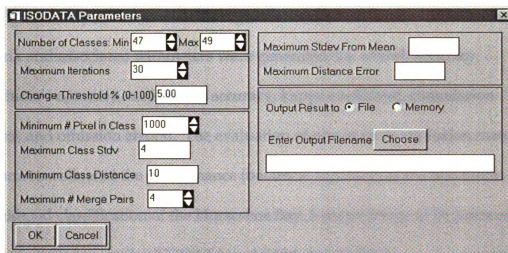


Figure 2.2. Isodata Classification Parameters

to 1, and represent the probability that a single pixel will be classified into any one spectral class. The 24 westerly ROIs (Table 2.6) served as the training data, generating a 25-class classification image (one being unclassified). A probability threshold of 0.70 was established that caused only those pixels with probabilities of 70% or greater to be included in any one spectral class. Pixels with probabilities lower than this threshold for all classes were unclassified. A probability threshold of 85% is commonly applied to remotely sensed data within the context of land use and land cover assessment (Anderson et al., 1976). Due to the general spectral complexity associated with coastal wetlands and the high precision of the classification categories (species or closely related assemblages) associated with coastal wetlands, a relaxed threshold of 70% seemed justified.

The easterly ROIs were used for ground-truth data from which a confusion matrix and associated parameters were generated (i.e. overall accuracy, producer's accuracy, consumer's accuracy, kappa coefficient, commission errors, and omission errors). The evaluation of one or more confusion matrix parameters allowed the performance (botanical accuracy) of the Maximum-Likelihood classification of the Horseshoe Bay, 1-meter image to be assessed and compared to similar ISODATA and SAM classifications.

2.2.6.3 Spectral-Angle-Mapper Classification (Investigation 1)

The second supervised classification routine utilized was the ENVI Spectral Angle Mapper (SAM), which is a physically- based spectral classification tool that uses spectral angles defined in n-dimensional data space to match pixel spectra to reference spectral signatures (RSI, 1999; p. 556). It is an automated method for comparing image spectra to individual spectra or a library of spectral signatures (Kruse et al., 1993).

A 24-class, SAM classification image was generated using the ROI-based methodology analogous to that outlined in the previous section. Two operational parameters were entered that governed the characteristics of the final SAM classification image. The maximum-value parameter was selected which causes the classification to include only those pixels with a rule value (angular sum = α) lower than a specified threshold. Varying α across a range of

0.1 to 0.4 radians generated a series of preliminary SAM image classifications. An α value of .25 was selected for use throughout this research because it resulted in a limited number of unclassified pixels while maintaining the ability to delineate similar spectra.

Analogous to the methodologies outlined in the previous section the easterly ROIs were treated as ground-truth data from which a confusion matrix and associated parameters were generated. The evaluation of one or more confusion matrix parameters allowed the performance (botanical accuracy) of the SAM classification of the Horseshoe Bay, 1-meter image to be assessed and compared to similar ISODATA and Maximum-Likelihood classifications.

2.2.6.4 PC-rotated Classifications ((Investigation 2)

Figure 2.1 illustrates that the first six principal components extracted from the hyperspectral imagery contain information linked to the spatial distribution of the botanical communities, and likely contain information vital to the differentiation of wetland vegetation. Two Maximum-Likelihood classifications were generated from the PC-rotated Horseshoe Bay imagery. The first utilized all 6 PCA dimensions (Figure 2.1) while the second used only PCA dimensions 2,3,4,5, and 6. Classification results generated without the 1st dimension (i.e. n-dimensional albedo) addressed whether or not this dimension is relevant to the differentiation of wetland plant communities. The Maximum-

Likelihood classifier was again configured to yield 24 botanical classes based on the operational parameters outlined in section 2.2.6.2.

Two SAM classifications were also generated from the Horseshoe Bay, PCA-transformed imagery similar to the classifications outlined in section 2.2.6.3. The first utilized all 6 PCA dimensions (Figure 2.1) while the second used only PCA dimensions 2,3,4,5, and 6. Confusion matrix parameters from the baseline (Investigation 1) and PC-rotated (Investigation 2) classifications were generated with respect to the 24 ground-truth ROIs shown in Table 2.6. These parameters allowed the relative differences in botanical classification accuracies between the first two investigations to be directly compared.

2.2.6.5 Prentiss Bay Classifications (Investigation 3)

The classification methodologies presented in the previous sections utilized the Horseshoe Bay, 1-meter CASI-II imagery. Investigation 3 utilized the 1-meter AISA imagery of Prentiss Bay in order to test whether classifier performance was consistent across multiple sensor technologies (CASI-II vs. AISA) and study sites. The regions-of-interest outlined in Table 2.5 were used in combination with the Prentiss Bay AISA imagery to generate a series of classifications analogous to those generated from the Horseshoe Bay imagery (sections 2.2.6.2 through 2.2.6.4). The ISODATA classification of the Prentiss Bay imagery significantly under-performed the two supervised classification

methodologies and was dropped from further consideration. The 20 westerly ROIs (Table 25) served as training data, generating a 21-class classification image (one being unclassified). The easterly ROIs were used as ground-truth data from which a confusion matrix and associated parameters were generated. The evaluation of one or more confusion matrix parameters allowed the relative performance (i.e. botanical accuracy) of analogous Prentiss Bay (i.e. AISA) and Horseshoe Bay (i.e. CASI-II) classifications to be compared.

2.3 Results and Discussion

Error matrices provided the foundation for comparing the many classification outcomes generated as part of this research, and provide a foundation for both descriptive and analytical statistical techniques (Congalton, 1991). Kappa Coefficients and overall-accuracy values best provide a measure of how well a classification performed regarding the ground-truth data (Table 2.5 and 2.6). Kappa Coefficients are an adjusted accuracy measure in which an estimate of chance agreement has been subtracted from the baseline overall-accuracy (Campbell, 1996; p. 390).

When classification outcomes are to be directly compared, it is prudent to verify if their associated Kappa Coefficients are statistically significantly different. Each confusion matrix generated for this research was manipulated in

a spreadsheet to generate the four independent theta coefficients (Hudson and Ramm, 1987; Congalton et al., 1983), which are intermediaries needed to calculate the Kappa variance and ultimately a Z-score (Congalton et al., 1983). Z-scores (equation 2.3) were used to establish whether the Kappa values from any two classifications were statistically different from each other at or above the desired confidence limit (i.e. 95%). Unless otherwise indicated within the classification summary tables, the results of all viable classification pairings were statistically different at or above the 95% confidence limit.

$$Z = (K_1 - K_2) / [(\text{sqrt}(V_{K1} + V_{K2}))]$$
Eq. 2.3

Where:

Z = z-score

K_i = Kappa Coefficient for classification i (Cohen, 1960)

V_{ki} = Variance associated with Kappa Coefficient i

The classification results associated with Investigations 1 through 3 are summarized in Table 2.7, which is partitioned into sections associated with each investigation. In most instances, there is only a minor difference between an overall-accuracy value and its paired Kappa Coefficient, indicating that chance agreement played an extremely small role in the classification results presented in Table 2.7.

2.3.1 ISODATA – Investigation 1

The first confusion matrix shown in Appendix B (i.e. sag1m-ISODATA-48classes) presents the results of the single ISODATA classification outlined in Chapter 2. The overall accuracy for this optimal ISODATA classification is 62.72%, which is approximately 25 percent lower than the best-performing, supervised classification outcome. Because the generated matrix parameters were the result of the prioritization methodology described in section 2.2, their class-specific meaningfulness is reduced in comparison to the other classification matrices. For example, one could conclude from the provided producers-accuracy values that the ISODATA classifier was able to definitively identify open water areas (i.e. column 12), but was completely unable to identify class 11, a deep submergent (i.e. *Vallisneria americana*). Examination of columns 11 and 12 reveals that 100 percent of the pixels in both the 11th and 12th ground-truth class fell within a single ISODATA class. Therefore, unless they were combined into a more heterogeneous class (e.g. water-dominant), either 36 or 47 pixels must represent a classification error. The prioritization scheme described in section 2.2 mandated that the highest magnitude value (i.e. 47) was assigned to the overlapping ISODATA class so that the ISODATA matrix represents the “best” classification outcome. Further class breakdown or “cluster-busting” is generally used to increase the interpretability of overlapping data, and is an iterative process of applying binary masks (0=other,

Classification Code	Overall Accuracy	Kappa Value	Inv.
Sag1m_MAXLIKE_70_24classes.cls	86.81%	0.86	I-1
Sag1m_SAM_25_24classes.cls	76.85%	0.7555	I-1
Sag1m_ISODATA_48classes.cls	62.72%	0.6023	I-1
Sag1m_PCA654321_MAXLIKE_70_24classes.cls	89.79%	0.8921	I-2
Sag1m_PCA65432_MAXLIKE_70_24classes.cls	82.55%	0.8158	I-2
Sag1m_PCA654321_SAM_25_24classes.cls	65.87%	0.6409	I-2
Sag1m_PCA65432_SAM_25_24classes.cls	60.85%	0.5878	I-2
prentiss_PCA654321_MAXLIKE_70_20classes.cls	85.50%	0.8441	I-4
**prentiss_SAM_25_20classes.cls	71.75%	0.6966	I-4
**prentiss_PCA65432_MAXLIKE_70_20classes.cls	70.45%	0.6816	I-4
prentiss_PCA654321_SAM_25_20classes.cls	65.99%	0.6344	I-4
prentiss_SAM_PCA65432_25_20classes.cls	56.51%	0.5311	I-4
prentiss_MAXLIKE_70_20classes.cls	44.42%	0.4046	I-4

** = lack statistical significance (95%) when paired

Table 2.7. Classification Accuracy Summary.

1=difficult to interpret classes) and re-classifying the original image with respect to these masks (Jensen, 1996; p. 238). This process is generally repeated until no newly interpretable classes are identified. Such an approach was applied to the baseline ISODATA classification in the hopes of improving the interpretation of several classes. Unfortunately, this process only acted to partition the “confused” classes into a greater number of classes, and did little to improve their delineation. Thus, only the baseline ISODATA results were presented. The presented ISODATA classification represents the best-performing, unsupervised classification with respect to the restructured

preliminary matrix. Because ISODATA under-performed the other classifiers, the specifics of its matrix were not further explored.

2.3.2 Maximum-Likelihood – Investigation 1

The Maximum-Likelihood classifier assigns each pixel into a spectral class based on the Euclidean distance between it and all class centroids (means) within n-dimensional data space (Jensen, 1996; p. 228). Within regions of overlap, Maximum-Likelihood considers the frequency distribution (assumed to be normal) related to each spectral class, and performs class assignments through the examination of relative probabilities. The unaltered confusion matrix associated with the baseline, Horseshoe Bay, Maximum-likelihood classification (i.e. sag1m_MAXLIKE_70_24classes.cls) is shown in Appendix B.

The overall classification accuracy is 86.81%, which is nearly 10 percentage points higher than the second best, Investigation 1 classifier (i.e. SAM). The highlighted diagonal entries represent the number of ground-truth pixels that were correctly classified. The comparison of these values to the bold-typeface, column totals illustrates the consistent classification accuracies associated with the Maximum-Likelihood classifier as applied in this research. The producers-accuracy values shown indicate that 13 of 24 classes were classified at levels higher than 95%, indicating that these botanical ROIs were well differentiated.

Examination of Table 2.7 reveals that Maximum-Likelihood is the best performing classifier throughout Investigation 1, but a few classes displayed extremely poor classification outcomes. Figure 2.3 presents nine spectral signatures captured with a hand-held spectroradiometer in order to better illustrate the weaknesses of Maximum-Likelihood. If the area of Figure 2.3 is viewed as a decision-space, then the magnitude (i.e. vertical) separation of the 3rd and 4th signature is small although their shapes are different. The magnitude-based decision rules utilized by Maximum-Likelihood would likely confuse these two classes despite their different shapes because of their “magnitude -overlap”.

Class 15 (i.e. muck) within the sag1m_MAXLIKE_70 confusion matrix further illustrates this idea of magnitude-based, class confusion. This training class was void of vegetation, and exhibited suppressed reflectance across the visible and NIR (signature 1 in Figure 2.3). The matrix values associated with this class reveal that one 1 of 27 pixels was correctly classified, a producers-accuracy of 3.7%. The 26 remaining pixels fell in six other classes, all of which were submergent or standing water/emergent classes. The spectral nature of these six classes was also suppressed due to the presence of significant amounts of water and dark substrates (i.e. muck, not sand). Within the context of the decision space, they are all within the same magnitude-class as the muck training class, and were subsequently cross-classified. The relatively subtle

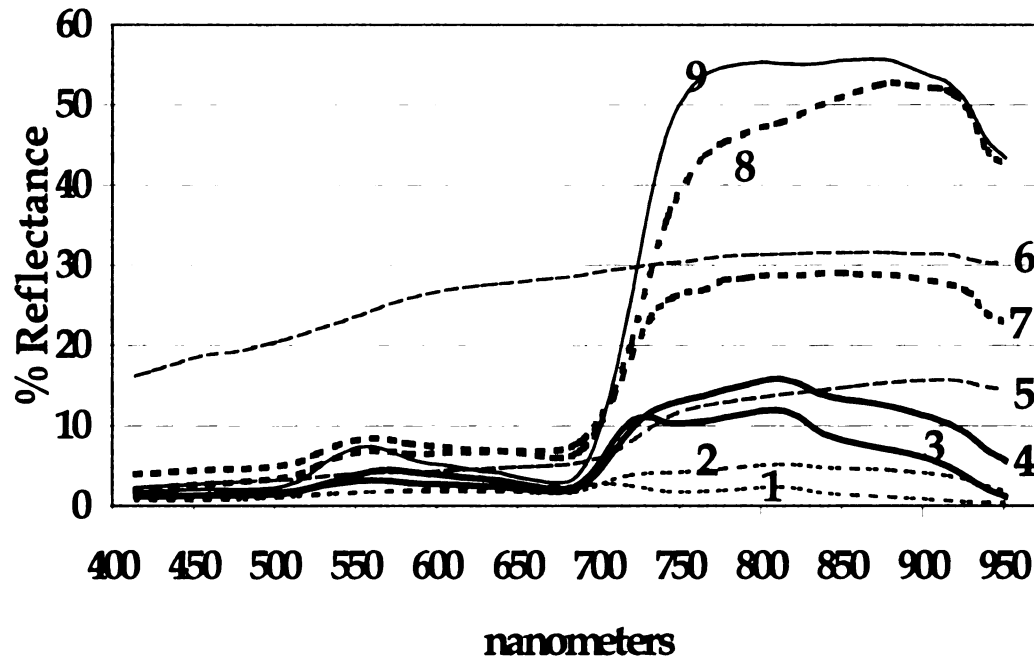


Figure 2.3. Nine Representative Spectra.

reflectance features that separate these signatures are not large enough within the context of the total decision space (i.e. 0-60% reflectance, 18 bands) to be differentiated by the Maximum-Likelihood classifier.

2.3.3 Spectral Angle Mapper – Investigation 1

The confusion matrix associated with the baseline, Horseshoe Bay, SAM classification (i.e. sag1m_SAM25_24classes.cls) is also shown in Appendix B. The overall classification accuracy is 76.85%, which is nearly 10 percentage points lower than the results associated with the Maximum-Likelihood classification. Again, the highlighted diagonal entries represent the number of

ground-truth pixels that were correctly classified. The comparison of these values to the bold-typeface, column totals illustrates the classification accuracies associated with the SAM classifier as applied in this research.

The producers accuracy values shown indicate that 6 of 24 classes were classified at levels higher than 95%, which is half of that generated from the Maximum-Likelihood classifier. Overall, 15 of 24 classes displayed accuracies below those of the Maximum-Likelihood classifier, with only 4 classes indicating significantly improved classification results. SAM cross-classified groups with similar greenness without regard to the magnitude-related differences that the Maximum-Likelihood classifier capitalized on to generate better results. “Relative-greenness” errors might be expected within the context of this research, since many wetland plants exhibit the characteristic peak-and-valley shape. A shape-based classifier like SAM would likely not perform well when confronted with training classes containing similar shapes. If this is true, two patterns should be evident in the baseline SAM confusion matrix: 1) classes that displayed better (i.e. > 6 pixels) classification results under SAM would be those that the Maximum-Likelihood classifier confused using magnitude-based decision rules alone, and 2) those classes that displayed significantly worse (i.e. > 6 pixels) classification results under SAM should be similarly-shaped classes that were able to be better separated with magnitude-based, Maximum-Likelihood decision rules.

Four classes (13, 15, 16, and 23) displayed significant classification improvement (i.e. > 6 pixels) over the Maximum-Likelihood classification. Of these four, class 23 best illustrates the strength of the SAM classifier as configured in this research. Class 23 represents a short stature, emergent species (*Eleocharis sp.*) distributed over a sandy substrate. This class is very similar from a biophysical perspective to class 22, which is the same species and substrate with a grass species (*Leeria oryzoides*) sparsely intermixed. One would expect these two signatures to be similar in both shape and magnitude considering their related cover types. SAM was able to effectively separate these two classes that Maximum-Likelihood classified poorly. This illustrates the power of SAM with respect to subtle, relative-greenness reflectance features that alter the shape (i.e. angular summation) across n-dimensional space.

Class 21 illustrates the inability of the SAM classifier to capitalize on magnitude differences. This class is one of several graminoid species that dominated the drier, sandy areas of Middle-Ground Island during the 2000 and 2001 growing seasons. As one might expect, many of these grass species display relatively green, similarly shaped curves due to their biophysical similarities. The Maximum-Likelihood classifier was able to separate this class (*Calamagrostis canadensis*) from its closely related neighbors with little error. The SAM classifier, on the other hand, confused this class with other relatively green signatures, one of which was an emergent, non-graminoid (i.e. Class 10).

The magnitude suppression that generally is associated with water-present, emergent signatures had little bearing on the SAM classification outcome that only references spectral shape. Thus, despite being completely separated in magnitude (i.e. y-axis shift), the SAM classifier cross-classified these similarly shaped classes (i.e. 21 and 10). The overwhelming majority of the errors found in the baseline SAM matrix are attributable to these types of greenness classification errors.

Maximum-Likelihood classifications are better suited for coastal wetland applications due to the magnitude separation (i.e. y-axis) of the predominant plant communities and genera. The strength of the SAM classifier is found in its ability to distinguish classes based on subtle shape changes, albeit without reference to demonstratively important, magnitude differences. A viable approach might utilize the SAM classifier to help separate only those classes that Maximum-Likelihood was unable to differentiate, potentially taking advantage of the relative strengths of both methodologies.

2.3.4 PC-rotated Classifications - Investigation 2

The confusion matrices from Investigation 2 are presented immediately following their associated baseline results in Appendix B. The classification accuracy associated with the Maximum-Likelihood classifier increased by approximately 3 percent to an overall-accuracy of 89.79% after PC-rotation of

the imagery. PCA acts to redistribute target variance across orthogonal, none-related dimensions. This redistribution is evident within the producers-accuracy values shown in the PCA654321, Maximum-Likelihood matrix. Only 4 classes (4, 6, 16 and 23) displayed improvements in this PCA-based classification when compared to the analogous Maximum-Likelihood classification of the baseline imagery. These classes experienced very significant improvements, but at the expense of 8 other classes whose producers-accuracies were slightly reduced. This result is consistent with the more equal distribution of target variance that is characteristic of PCA.

In order to better illustrate the role PCA plays with respect to the classification results presented in this research, 24 PCA-transformed, spectral signatures are shown in Figure 2.4. The data were truncated to not include dimensions 5 and 6 because there was little dimensional variation beyond dimension 4, which is consistent with the variance percentages presented in Appendix A. The characteristic peak-and-valley shape of botanical spectra is no longer present in the PC-rotated signatures. The signatures have been redistributed across the six PC dimensions, with the first three containing most of the visible variation (see Appendix A). The fan-like arrangement of signatures found between the first two dimensions represents a more equitable distribution of target radiance, and little signature overlap is present. Reduction in signature overlap would likely improve Maximum-Likelihood

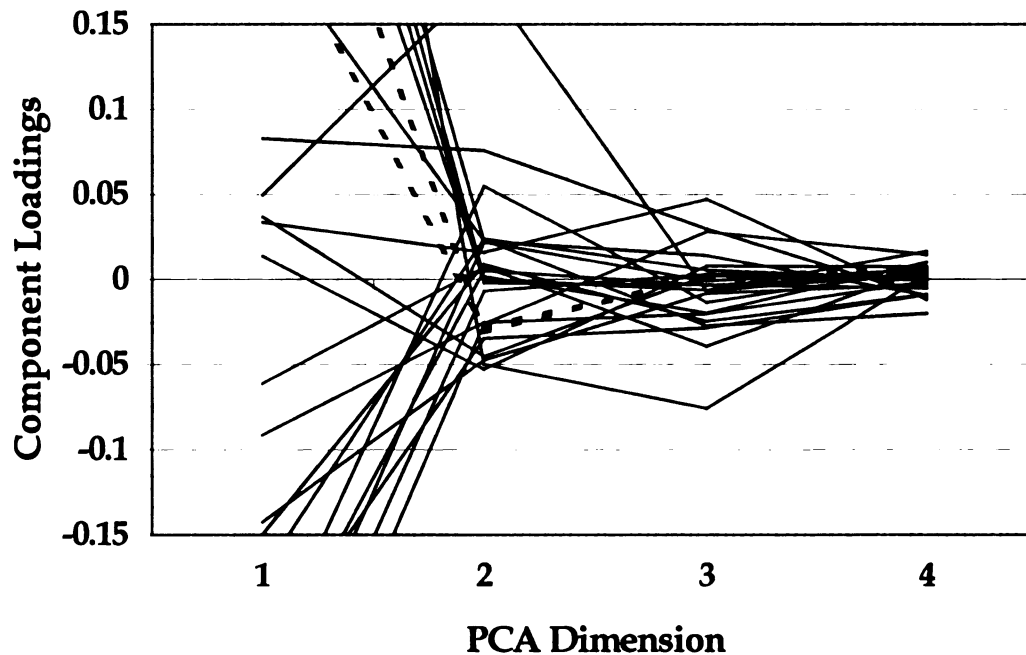


Figure 2.4 PC-transformed Spectral Signatures.

(i.e. magnitude-based) classification results while having little effect on SAM
(i.e. shape-based) results.

The unrotated, Maximum-Likelihood classification resulted in very high classification accuracies. Thus, one can conclude that the overwhelming majority of the ground-truth spectral classes were distinguishable based on reflectance magnitude differences. This being the case, the PC-rotation was not likely to improve classification accuracies greatly, as evident by the slight improvement of approximately 3%.

The shape or angular complexity (i.e. vectors between successive bands) has been reduced to the hinge-points associated with the 2nd and 3rd PC-dimensions. A shape-dependent classification tool like SAM would suffer from this reduction of angular complexity. The overall-accuracy of the SAM classification of the PC-rotated imagery was reduced to 65.87%, placing it among the worst performing classification results found throughout Investigations 1 and 2.

Maximum-Likelihood and SAM classifications generated from PC-rotated imagery without the contribution of dimension 1 significantly under-performed their 6-dimension un-rotated counterparts (i.e. 7% and 5%, respectively). It was initially hypothesized that the first PC dimension could be removed without significantly impacting botanical differentiation because PC1 captured the predominant commonality found in the various cover types. Removal of this “commonality” dimension, it was surmised, would place added emphasis on the lower-order dimensions that capture subtle-differences information. Obviously, this hypothesis must be rejected. PC1 is required in order to optimize either Maximum-Likelihood or SAM classifications.

2.3.5 Prentiss Bay Classifications – Investigation 3

The third tier of results presented in Table 2.7 summarizes the classification accuracies related to all of the Prentiss Bay classifications. The baseline

confusion matrices associated with Investigation 3 are shown in Appendix B. The “best” classification methodology identified within Investigations 1 and 2 (Horseshoe Bay) was the Maximum-Likelihood classifier applied to the PC-rotated imagery, although only a few percentage points separated the overall-accuracies associated with the baseline (86.8%) and PCA654321 (89.8%) Maximum-Likelihood classifications. In contrast, the overall accuracy of the Prentiss Bay Maximum-Likelihood classification was 44.42%. This was the lowest accuracy level recorded for all of the Prentiss Bay image classification trials. This surprising lack of performance initially called into question the “best” classifier identified in Investigations 1 and 2. In light of these results, three SAM classifications were generated via the Prentiss Bay imagery s (i.e. baseline, PCA654321, and PCA65432) as a means to cross-validate the findings of Investigations 1 and 2. The overall-accuracies and Kappa values of the SAM classifications were very similar to the SAM results from Horseshoe Bay. These similarities indicate that there is a characteristic inherent to the AISA imagery that caused Maximum-Likelihood to perform so poorly.

It was established earlier that dimensions generated via PCA are independent (i.e. orthogonal), as well as less noisy because systematic noise is sequestered into one or more lower-order dimensions (Lillesand and Kiefer, 2000; p. 520, Jensen, 2000; p. 179). Thus, significant Maximum-Likelihood improvements should result from PC-rotation in reference to systematically

noisy imagery like the baseline, Prentiss Bay data. The overall-accuracy associated with the Maximum-Likelihood classification of the 6-dimension (i.e. PCA654321) Prentiss Bay imagery was 85.50%. Although not as high as its Horseshoe Bay counterpart, this level of accuracy is comparable to the I-1 results. The primary role of the Prentiss Bay image analyses within this research was to provide a second set of imagery (differing in both sensor type and location) in order to test the transferability of select methodologies. The overall PC-rotated accuracies presented in Table 2.7 indicate that the methodologies applied to the Horseshoe Bay imagery are indeed applicable at ecologically different locations. Investigation 3 also pointed out that the characteristics and idiosyncrasies of each sensor can potentially play a significant role in classification performance. This recognition reinforces the importance of PCA in wetland image classification.

2.4 Summary and Conclusions

It was established in previous chapters that coastal wetlands could be botanically complex, exhibiting a rich mosaic of plant species/assemblages that are distributed along the predominant hydrologic gradient. It is this characteristic that typically makes wetlands a challenging remote sensing target due to the relative spectral similarity of the predominantly vegetated landscape. Botanical training sites (Regions-of-Interest) were delineated that represented the predominant cover types found in each study site during the 2000 and 2001

field campaigns. These ultimately served as the basis for multiple classification comparisons.

The probability-based Maximum-Likelihood classifier was the best performing classifier with respect to the differentiation of the field-delineated ROIs. Approximately 87% of the accuracy assessment pixels (easterly ROIs) were correctly classified by Maximum-Likelihood, which was nearly ten percent higher than the comparable SAM classification. It was shown that probability-based classifiers are magnitude-dependent (y-axis separation), and their associated errors are typically associated with within-class misclassifications. Maximum-Likelihood displayed the greatest potential for differentiating the complex botanical communities found in the Lake Huron wetlands analyzed in this study. From a practical standpoint, the Maximum-Likelihood classifier would be ideal for delineating major botanical classes when some degree of within-class error (e.g. confusion of similarly structured emergent species) can be tolerated.

The baseline SAM classifier under-performed the Maximum-Likelihood classifier by nearly ten percent. This physically-based classification tool tended to confuse classes that displayed similar greenness (i.e. shape of the reflectance signature), and differed from Maximum-Likelihood in that it is insensitive to magnitude differences. Both the Les Cheneaux and Saginaw Bay imagery was

taken as the botanical community neared the end of its growing season, which likely contributed to the success of the SAM classifier because the plant community was in various stages of dieback. Imagery taken when the community was at “peak green” would likely lead to an increase in greenness confusion by the SAM classifier.

The strengths of both classification tools could be used in combination to enhance classification accuracies. Maximum-Likelihood should be used to parse an image into the predominant classes. Then, complex classes could be isolated via image masking in order to capitalize on the ability of the SAM classifier to differentiate similar spectra based on relatively subtle spectral features that are lost in the magnitude-based approach. This is certainly an area that needs to be explored further within the context of coastal wetlands.

Covariance-based PCA rotation proved to consistently enhance the performance of the probability-based classifiers. From a practical standpoint, this research indicates that PCA rotation should routinely be utilized in combination with probability-based classification tools. The resulting dimensionally-reduced signatures are better differentiated by the magnitude-sensitive classifiers because the image spectra are more equitably distributed (i.e. more magnitude separation). A more detailed examination of Figure 2.4 revealed that biophysically relevant clusters of spectra do indeed exist,

especially between the second and third dimensions. These clusters (e.g. see dashed spectra) represent similar within-class spectra that proved to be the underlying weakness of the Maximum-Likelihood classifier. It is these tightly clustered groups within the rotated spectra that would best be classified via SAM.

The dimensional reduction that assisted the probability-based classifier (i.e. Maximum Likelihood) significantly reduced the effectiveness of the SAM classifier. The angular coefficients that form the foundation of the SAM classifier are determined by summing the angular complexity of spectra across all bands. A reduction in bands would inherently reduce the likelihood that diagnostic differences would be maintained. The inability of the SAM classifier to utilize PC-rotated imagery creates a logistical concern when the strengths of both it and a probability-based classifier are to be combined. Ultimately, rotated and non-rotated imagery would have to be maintained and identically masked in order to implement a combined (Maximum Likelihood and SAM) classification strategy.

The Prentiss Bay imagery was incorporated into this research in order to test the transferability of “methods” developed with respect to the Horseshoe Bay, 1-meter imagery. Generally, the outcome of like-configured Prentiss and Horseshoe Bay classifications were very similar, and trends were common

throughout. The PC-rotated Maximum-Likelihood and un-rotated SAM classifications as outlined in this research were not site dependent, and could likely provide the basis for basin-wide wetland mapping, especially in combination.

Although not completely understood, it seems likely that some type of systematic radiometric noise was inherent to the AISA imagery, as evident by the poor SAM and Maximum-Likelihood classification results generated via the raw AISA imagery. PC-rotation is known to sequester such systematic noise into lower-order dimensions, and this was indeed the case in this research as evident by the sharp increase in the accuracy of the Maximum-Likelihood classification (41 percentage points) after PC-rotation of the AISA imagery. These results suggest that results generated from a probability-based classifier in conjunction with both raw and rotated imagery could function as a viable test for subtle, system-level noise.

Chapter 3: Principal components and second derivative analyses of hyperspectral reflectance data from freshwater coastal wetlands.

3.1 Introduction and Rationale

In the 1970s, state and federal agencies increasingly looked towards aerial photography for the purposes of wetland mapping and inventory (Gross et al., 1989; p. 475). Film types that are sensitive to NIR electromagnetic energy are generally preferred for wetland applications because they are more effective in detecting standing water and determining biomass, as well as differentiating wetland and upland vegetation (Hardisky et al., 1986). Aerial photography (1:1000 to 1:15,000 scales) has been found to be a fast, accurate, and relatively inexpensive method by which wetland boundaries, botanical changes, and aerial extent can be recorded (Mitsch and Gosselink, 2000; p. 107). Two characteristics limit the applicability of aerial photography to detailed vegetative mapping strategies: 1) the limited amount of spectral information contained in each image (Jensen et al., 1986), and 2) its non-digital format (Hardisky et al., 1986).

The launch of the Landsat-1 satellite (1970s) marked the practical beginning of spaceborne, earth resource remote sensing. Over the ensuing thirty years, a variety of systems, with varied spatial and spectral resolutions, have been

developed. Orbiting satellite-based sensors can provide near-simultaneous coverage of wetland imagery over large geographic areas recorded in digital format (Gross et al, 1989; p. 476). Satellite platforms continue to provide an overwhelming array of earth resource data when fitted with remote sensing systems, and the status of these technologies continues to change as scientific advances yield improved spacecraft and sensors (Lillesand and Kiefer, 2000; p. 373). However, regarding their utility for detailed wetland characterization, current systems are limited by their spatial and/or spectral resolutions. These limitations become obvious in the context of the two fundamental assumptions of this research: 1) the spatial heterogeneity of coastal wetlands is best captured by digital imagery with a spatial resolution of 5 meters or smaller, and 2) differentiation of wetland plant communities is best achieved through the analysis of hyperspectral reflectance records. Accepting these assumptions means that aerial photography and currently available satellite imagery are sub-optimal for detailed wetland mapping.

The development of imaging spectrometers created interest in utilizing spectral reflectance data of vegetation canopies measured from the ground to aid in remotely differentiating plant communities. In fact, many next-generation, satellite-based systems (e.g. COIS, Hyperion, MODIS or Warfighter-1) incorporate hyperspectral sensors in order to address the spectral limitations of aerial photography and current satellites systems (ASPRS, 1995; Stoney and

Hughes, 1998; Thenkabail et al., 2000). A major advantage of imaging spectrometry lies in the potential for integrated analysis comparing calibrated remotely sensed imagery with field spectral measurements (Goetz 1992; Kruse et al, 1993). The use of systematic differences in canopy pigmentation and related chemistry to classify to the botanical species level has recently emerged as a promising new approach.

Recent literature has shown that narrow, strategically placed bands may be crucial in providing additional information with significant improvements over broad bands in quantifying biophysical characteristics of agricultural crops (Thenkabail et al., 2000). Although not widespread, the wetland literature contains recent examples of investigations that utilized hyperspectral systems to map and monitor plant communities (Savastano, 1984; Zacharis, 1992; Forsyth, 1998; Borstad Associates, 1995; Jupp, 1994; Ritter and Lanzer, 1997; Brown and Borstad, 1999; Wang, 2000). Common to these investigations is the exploitation of improved spatial or spectral resolutions to more effectively differentiate wetland vegetation, although none explore the independent contribution of spatial and spectral resolution.

Derivative techniques have long been applied in remote sensing, and have been found to eliminate background signals, differentiate overlapping signals,

and reduce the affects of turbidity in aquatic chlorophyll investigations (Demetriades-Shah, 1990). Higher-order (i.e. 2nd-order) derivatives become important within the context of remote sensing because relative reflectance amplitudes (vertical stretch) increase with derivative order (Fell and Smith, 1982).

In remote sensing, feature extraction involves the identification of those statistical characteristics of remotely sensed data that capture the most systematic variation (Campbell, 1996; p. 288). Systematic variations, as opposed to non-systematic variations (i.e. noise), ultimately provide the foundation for target differentiation. Within multispectral data, often there is significant correlation between the information contained in closely adjacent bands. This is especially true with hyperspectral data sets composed of narrow, contiguous bands. In principle, feature extraction can significantly reduce the magnitude of a dataset by isolating essential components (i.e. information) while discarding redundant or noisy data (Campbell, 1996; p. 288).

A feature extraction tool commonly applied throughout the scientific community is Principal Components Analysis (PCA). PCA has been effectively applied in the analysis of multispectral data, resulting in more interpretable

data via the reduction of large image data sets into relatively few meaningful dimensions (Jensen, 1996; p. 172). In essence, the purpose of PCA is to compress all the information (correlation/ variance) contained in an original data set into fewer, independent (orthogonal) channels – the principal components (Lillesand and Kiefer, 2000; p. 518). A detailed description of the statistical framework used to perform PCA is beyond the scope of this research, although a more complete explanation can be found in (Davis, 1986).

The goal of this component of my research is to perform derivative and Principal Components Analysis in order to identify those (hopefully few) recorded bands that are most appropriate for the differentiation of vegetation types within the coastal wetlands of the Great Lakes. This goal addresses the second research objective outline in Chapter 1; Quantitatively examine the properties of in-situ reflectance data to discern the optimal spectral framework of wetland imagery.

3.2 Methods

3.2.1 Spectral Data Pre-Processing

In-situ reflectance measurements were collected for the predominant species, species assemblages, and cover types at both the Prentiss and Horseshoe Bay study sites. All spectral data were collected during the 2001

growing season (July-September). These nadir measurements were taken with an SE-590 spectroradiometer, outfitted with an 11° field-of-view optic (Spectron Engineering, Inc. Denver, Colorado), approximately 1 meter above the canopy. At a sensor height of 1 meter, a circular area with a diameter of 18 centimeters was sampled. The SE-590 recorded 252 contiguous bands from 365 to 1,125 nanometers, with an approximate bandwidth of 3 nanometers. Prior to the field campaign, the SE-590 was cross-calibrated with a newly-calibrated FieldSpec-Pro spectroradiometer from Analytical Spectral Devices (www.asdi.com) to ensure the integrity of the spectral signatures being captured.

The SE-590 was pre-programmed to capture eight consecutive measurements within a few seconds; these were then internally averaged to yield raw radiance data. Nearly 100 spectra were recorded as summarized in Table 3.1. Whenever feasible, duplicate or triplicate measurements were made and averaged in order to characterize additional target variability. The SE-590 was connected via its RS-232 port to the serial port of a laptop computer running a custom software program. This software package allowed the reflectance data (raw radiance) from the plant canopy and a reflectance standard (i.e. reference panel) to be stored in a text-based export file after being normalized for differences in integration time.

<u>Site/Date:</u>	<u>Code:</u>	<u>Description:</u>
Horse/824-23	HB-1	AVG <i>H. dubia</i>
Horse/824-23	HB-2	<i>H. dubia</i> (surface)
Horse/824-23	HB-3	AVG <i>Chara</i> sp. (10 in)
Horse/824-23	HB-4	AVG <i>S. rigida</i> / <i>Chara</i> sp. (30/70)
Horse/824-23	HB-5	AVG <i>S. rigida</i> / <i>H. dubia</i> (30/70)
Horse/824-23	HB-6	AVG <i>S. rigida</i> / <i>Chara</i> sp. 60/40
Horse/824-23	HB-7	AVG <i>S. rigida</i> / <i>Chara</i> sp. (80/20 -15 in water)
Horse/824-23	HB-8	AVG sand/ <i>Chara</i> sp. 8 in (95/5 18 in.)
Horse/824-23	HB-9	Sand (clouded H20)
Horse/824-23	HB-10	Sand/ <i>Chara</i> sp. 8 in (95/5 18 in.)
Horse/824-23	HB-11	AVG <i>V. americana</i> /Sand (70/30 - 12 in.)
Horse/824-23	HB-12	AVG <i>L. oryzoides</i> (90% cover)
Horse/824-23	HB-13	<i>U. dioica</i>
Horse/824-23	HB-14	<i>I. capensis</i> (orange blooms)
Horse/824-23	HB-15	AVG <i>S. validus</i> (80% - bloom)
Horse/824-23	HB-16	<i>S. validus</i> / <i>Eleocharis</i> sp. (75/25 - browning)
Horse/824-23	HB-17	<i>S. validus</i> /Sand (30/70)
Horse/824-23	HB-18	<i>S. validus</i> /sand (30/70 - 2 in.)
Horse/824-23	HB-19	<i>Chara</i> sp. (3 in.)
Horse/824-23	HB-20	AVG <i>Chara</i> sp./ <i>S. graminia</i> (80/20 - 6 in.)
Horse/824-23	HB-21	AVG <i>S. validus</i> (85% - clumps in 8 in.)
Horse/824-23	HB-22	<i>T. angustifolia</i> (75% - 4 in. sandy)
Horse/824-23	HB-23	AVG <i>T. angustifolia</i> / <i>S. rigida</i> /algae (40/40/20)
Horse/907-9	HB-24	AVG <i>P. australis</i> (brown heads)
Horse/907-9	HB-25	<i>Bidens</i> sp.
Horse/907-9	HB-26	AVG <i>E. maculatum</i> (headed out white)
Horse/907-9	HB-27	<i>T. angustifolia</i> (50% green, windblown)
Horse/907-9	HB-28	AVG <i>S. americana</i> (70% cover)
Horse/907-9	HB-29	AVG <i>S. latifolia</i> (large leaf)
Horse/907-9	HB-30	AVG <i>P. amphibium</i> / <i>S. latifolia</i> (30/70)
Horse/907-9	HB-31	<i>Bidens</i> sp./ <i>P. australis</i>
Horse/907-9	HB-32	AVG gravel at Ramp
Pre/703-25	PB-1	AVG <i>T. angustifolia</i> (deadfall)
Pre/703-25	PB-2	AVG <i>S. acutus</i> / <i>T. Angustifolia</i>

Table 3.1. Collected In-situ Spectral Signatures.

Pre/703-25	PB-3	AVG <i>S. acutus</i> (deadfall)
Pre/703-25	PB-4	AVG <i>N. advena</i> (mud, no H20)
Pre/703-25	PB-5	AVG <i>Chara</i> sp./ <i>P. natans</i>
Pre/703-25	PB-6	<i>S. acutus</i> (H20)
Pre/703-25	PB-7	AVG <i>N. advena</i> (H20)
Pre/703-25	PB-8	AVG <i>P. natans</i> (H20)
Pre/703-25	PB-9	H20 (stirred)
Pre/703-25	PB-10	H20 (clear)
Pre/703-25	PB-11	Dolomite
Pre/703-25	PB-12	Muck/mud
Pre/703-25	PB-13	Blowdown
Pre/703-25	PB-14	AVG <i>C. lasiocarpa</i>
Pre/703-25	PB-15	AVG <i>C. stricta</i>
Pre/703-25	PB-16	<i>Potentilla</i> sp.(scrub)
Pre/703-25	PB-17	<i>C. lasiocarpa</i> / <i>S. acutus</i>
Pre/703-25	PB-18	<i>Salix</i> sp. (shrub)
Pre/703-25	PB-19	<i>Juncus</i> sp.
Pre/703-25	PB-20	<i>S. latifolia</i> (mud)
Pre/703-25	PB-21	mud
Pre/703-25	PB-22	gravel
Pre/703-25	PB-23	Asphalt
Pre/703-25	PB-24	<i>Helianthus</i> sp.
Pre/703-25	PB-25	<i>Scirpus</i> sp.
Pre/827-39	PB-26	<i>C. viridula</i> /dry muck soil (80/20)
Pre/827-39	PB-27	<i>C. viridula</i> /dry muck soil (90/10)
Pre/827-39	PB-28	<i>J. canadensis</i> / dry muck soil (70/30)
Pre/827-39	PB-29	<i>J. canadensis</i> /dolomite rock (80/20)
Pre/827-39	PB-30	<i>C. viridula</i> /muck soil (10/90)
Pre/827-39	PB-31	<i>C. viridula</i> /saturated muck soil (5/95)
Pre/827-39	PB-32	<i>S. acutus</i> (50/50 green/dead)
Pre/827-39	PB-33	<i>S. acutus</i> (90/10 green/dead - 1 in.)
Pre/827-39	PB-34	<i>S. acutus</i> (70/30 green/dead)
Pre/827-39	PB-35	<i>C. acutus</i> (60/40 green/dead)
Pre/827-39	PB-36	<i>T. angustifolia</i> (medium density, sat. soil)
Pre/827-39	PB-37	<i>T. angustifolia</i> /H20 (50/50, 80/20 green/dead)

Table 3.1. Continued.

Pre/827-39	PB-38	AVG <i>P. natans</i> /muck soil (85/15 no H2O)
Pre/827-39	PB-39	<i>Nuphar advena</i> /muck soil (80/20 4 in. H2O)
Pre/827-39	PB-40	<i>N. advena</i> /muck soil (60/40, 4in H2O)
Pre/827-39	PB-41	<i>S. acutus</i> (dense, muck soil, 4 in. H2O)
Pre/827-39	PB-42	<i>S. acutus</i> (medium, muck, 4 in. H2O)
Pre/827-39	PB-43	H2O (sandy/muck substrate, 2 in. depth)
Pre/827-39	PB-44	<i>P. natans</i> / <i>N. flexilis</i> (60/40 - 4 in. H2O)
Pre/827-39	PB-45	<i>N. flexilis</i> (95/5 - 8in H2O)
Pre/827-39	PB-46	H2O (muck, 8-10 in. depth)
Pre/827-39	PB-47	<i>S. acutus</i> (medium, 8 in. H2O)
Pre/827-39	PB-48	<i>T. angustifolia</i> (sparse, 8 in. H2O)
Pre/827-39	PB-49	<i>T. angustifolia</i> / <i>S. acutus</i> (sparse, 6 in. H2O)
Pre/827-39	PB-50	<i>C. lasiocarpa</i> / <i>Cladium mariscoides</i> / <i>S. acutus</i>
Pre/827-39	PB-51	<i>C. lasiocarpa</i> (20 <i>S. acutus</i> stems/m ²)
Pre/827-39	PB-52	AVG <i>C. lasiocarpa</i> (20/80 green/dead)
Pre/827-39	PB-53	<i>C. lasiocarpa</i> (10/90 green/dead)
Pre/827-39	PB-54	<i>C. stricta</i> (15/85 green/dead)
Pre/827-39	PB-55	<i>C. stricta</i> (20/80 green/dead)
Pre/827-39	PB-56	<i>C. stricta</i> (30/70 green/dead)
Pre/827-39	PB-57	<i>C. stricta</i> (40/60 green/dead)
Pre/827-39	PB-58	<i>Alnus sp.</i> / <i>C. stricta</i> (90/10)
Pre/827-39	PB-59	<i>C. stricta</i> (5/95 green/dead)
Pre/827-39	PB-60	<i>C. lasiocarpa</i> (30 <i>S. acutus</i> stems/m ²)
Pre/827-39	PB-61	<i>C. lasiocarpa</i> (sparse <i>T. angustifolia</i>)
Pre/827-39	PB-62	<i>Solidago rigida</i>
Pre/827-39	PB-63	road gravel
Pre/827-39	PB-64	Asphalt

Table 3.1. Continued

The reference panel used for the in-situ data collection was a 14-inch square aluminum panel coated with polytetrafluoroethylene (PTFE). Reference panel (ρ_{msu}) measurements were made before and after each series of measurements by holding the SE-590 sensor (nadir-looking) 0.5 meters above the panel to ensure that the 11° field-of-view fell completely upon the surface of the relatively small reference panel. These panel measurements served as endpoints for a linear interpolation that provided a reference panel measurement specific to each botanical measurement and unique solar angle.

The captured radiance values were transformed into values of absolute reflectance by reference to radiance measurements taken from a calibrated reference panel (Equation 3.1). A reflectance coefficient ($\rho^{\alpha}_{\text{msu}}$) was generated

$$\rho_{\text{in-situ}} = E_{\uparrow \text{in-situ}} / E_{\uparrow \text{interpolated}} * \rho^{\alpha}_{\text{msu}} \quad (\text{for bands 1 through 252}) \quad (\text{Eq. 3.1})$$

$E_{\uparrow \text{in-situ}}$ = In-situ target radiance
 $E_{\uparrow \text{interpolated}}$ = Linearly interpolated reference panel radiance
 $\rho^{\alpha}_{\text{msu}}$ = Reference panel reflectance coefficient
 $\rho_{\text{in-situ}}$ = In-situ target percent reflectance

for the in-situ reference panel utilized in this investigation via radiance measurements ($E_{\uparrow \text{msu}}$) taken of it and a Spectralon panel ($E_{\uparrow \text{spec}}$) under controlled darkroom lighting. A simple regression ($R > .99$) established that the reflectance properties of Spectralon and the aluminum panel were indeed linear. A 2nd-order polynomial was then fit to published Spectralon reflectance

coefficients ($\rho_{\text{spec}}^{\alpha}$ @ 100nm increments). The resulting polynomial equation was used in conjunction with SE-590 upwelling radiance (E_{\uparrow}) measurements of both the reference and Spectralon panels to calculate $\rho_{\text{msu}}^{\alpha}$ that is needed to transform raw radiance signatures into percent reflectance. Because no effort was made to characterize the bi-directional reflectance of these surfaces, three steps were taken throughout both the calibration work and the in-situ data collection in order to minimize its affects: 1) all in-situ data were collected within 2.5 hours before or after solar noon, 2) only nadir, in-situ measurements were taken, and 3) sensor/beam geometries were held as constant as practical during all calibration measurements.

After each signature was transformed into percent reflectance, it was imported into a spectral library within ENVI (i.e. Environment for Visualizing Imagery) image processing software. Alphanumeric botanical keys were created (e.g. HB1; Table 3.1), each corresponding to a specific in-situ measurement, so that the integrity of the botanical data was more easily maintained during the migration into ENVI. The transformed data were then resampled to emulate the spectral characteristics of the hyperspectral imagery (i.e. 48 bands, approx. 7nm wide) utilized in the second component of this research. The 96 baseline spectral libraries (Table 3.1, 252 bands) were resampled within the spectral tools module of ENVI, utilizing the band center/FWHM of the 48-hyperspectral bands. These resampled data, examples

of which are shown in Figure 3.1, provided the foundation for more detailed data analyses.

3.2.2 2nd Derivative Approximations

Signatures like those shown in Figure 3.1 are made up of a series of line segments established by reflectance values recorded at each band center. Second-derivative values do not exist for line segments, so some type of an approximation must be used. Second-derivative approximations identify spectral locations where the slope of the reflectance curve experiences a relatively abrupt change (i.e. points of inflection). Fundamentally, spectral regions of abrupt change are inherently more diagnostic than areas with

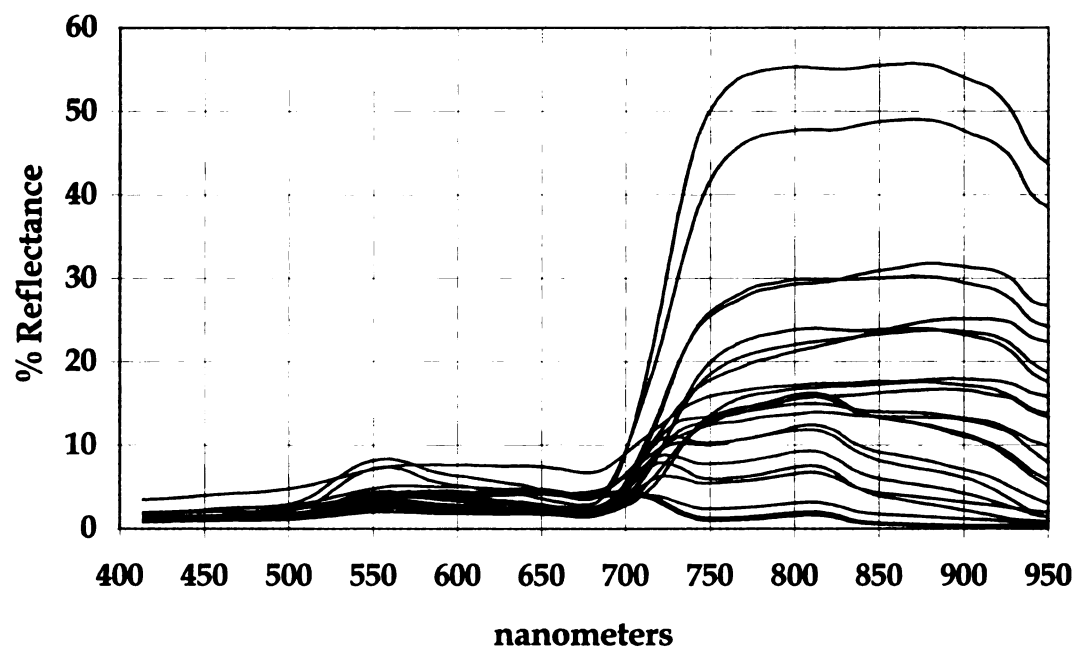


Figure 3.1. Representative Spectral Signatures

uniform slopes. A slope-based, numerical method was used to transform the botanical spectra (Figure 3.1) into 2nd derivative approximations.

A modified version of the slope-based, two-step, derivative-approximation method presented by Tsai and Philpot (1999) was utilized in this research (Figure 3.2). The first step determined the slope of a line segment by simply dividing reflectance value differences by the wavelength interval separating them (rise/run) as indicated by Equation 3.2.

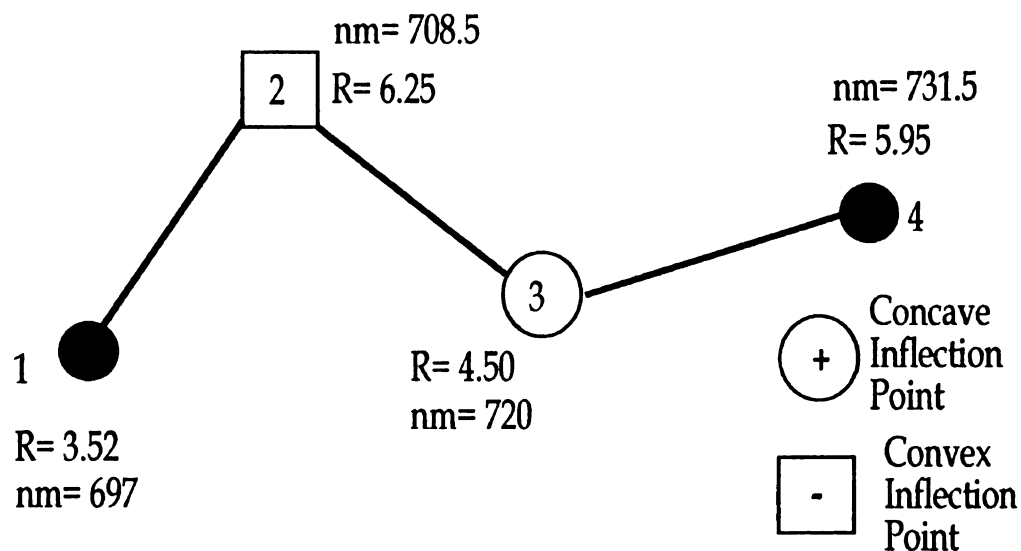
$$d^{1st} = (\rho_{n+1} - \rho_n) / (\lambda_{n+1} - \lambda_n) \quad \text{where } n = \text{band number} \quad (\text{Eq. 3.2})$$

d^{1st} = 1st-derivative (line segment slope)

ρ = absolute (percent) reflectance

λ = wavelength (nm)

Second derivatives were calculated similarly, although the equation was modified so that the wavelength domain across all three data points was included (Equation 3.3). In addition, a multiplier (0.5) was incorporated in the denominator to enhance any reflectance amplitude differences (vertical separation), making the visual differentiation of overlapping spectral signatures easier. Due to the structure of equations 3.2 and 3.3, the spectral data associated with the first and last band numbers are lost during the calculation of the 2nd derivative approximation. This 2nd derivative method was structured so that the derivative values generated fell exclusively on the center band of the band-triplet referenced in each derivation (see Figure 3.2).



1st Derivative
(Slope)
Line segment
1-2

$$\longrightarrow \frac{(6.25 - 3.25)}{(708.5 - 697)} = 0.2608$$

1st Derivative
(Slope)
Line segment
2-3

$$\longrightarrow \frac{(4.50 - 6.25)}{(720 - 708.5)} = -0.1521$$

1st Derivative
(Slope)
Line segment
3-4

$$\longrightarrow \frac{(5.95 - 4.50)}{(731.5 - 720)} = 0.1260$$

2nd Derivative Approx.
(Slope of Slope)
Line segment
@Point #2

$$\longrightarrow \frac{(-0.1521 - 0.2608)}{(720 - 697) 0.5} = -0.4129$$

2nd Derivative Approx.
(Slope of Slope)
Line segment
@Point #3

$$\longrightarrow \frac{(0.1260 + 0.1521)}{(731.5 - 708.5) 0.5} = 0.2781$$

Figure 3.2. Derivative Calculation Schematic.

$$d^{2nd} = (d^{1st}_{n+1} - d^{1st}_n) / 0.5(\lambda_{n+2} - \lambda_n) \quad \text{where } n = \text{band number} \quad (\text{Eq. 3.3})$$

d^{1st} = 1st derivative

d^{2nd} = 2nd derivative approximation

λ = wavelength (nm)

The derivative values for each of the 96 spectra (Table 3.1) were placed in a single spreadsheet to facilitate their analysis. Each paired column of derivative and band-center values were simultaneously sorted in ascending order with respect to derivative magnitude. This sorting method ensured that the band center associated with each derivative value remained linked to that specific value, thereby preserving the integrity of each data couplet. A second spreadsheet function was then applied so that the appropriate sign (+/-) of each derivative was applied to its linked band center. The 20 largest-magnitude derivatives (i.e. 10 positive and 10 negative) were extracted from the sorting spreadsheet and placed into Appendix C. High magnitude derivative values identify regions of diagnostic spectral change, and they should represent those bands that are most appropriate for the differentiation of the input spectra (i.e. wetland vegetation).

3.2.3 Principal Components Analysis

The statistical software package SYSTAT (www.spssscience.com) was utilized to transform the 48-channel, in-situ data into their principal components (i.e. dimensions). SYSTAT's data reduction module accepts a

variety of two dimensional data arrays, the dimensions of which outline the dependent (rows) and independent (columns) variables of interest. Band number was established as the independent variable in order to characterize the explanative power of all 48 bands with respect to the sampled, botanical community (dependent variable). The information contained in each resampled spectral library was exported via an ASCII text file into an EXCEL spreadsheet, with each column relating to the spectral characteristics of one botanical target and each row referencing a specific band center (wavelength). This structure was opposite that needed by SYSTAT in order to test the relationship between the dependent and independent variables outlined above. Thus, the spreadsheet containing all 96 spectral signatures (Table 3.1) was transposed in order to yield the appropriate column (band number) and row (botanical reflectance) data structure. Eight rows of data containing the spectral information derived from non-vegetative targets such as shallow water and gravel were eliminated. The remaining 88 rows, signatures taken of areas with at least some visible vegetation, were subjected to Principal Components Analysis.

Correlation-based PCA references standardized input variables that have a mean of zero and a variance of one. Standardization tends to inflate the contribution of variables whose variance is small, and reduce the influence of variables whose dimensions are large (Davis, 1986; p. 536). PC analyses based

on correlation matrices generate dimensions that emphasize those spectral features that best capture predominant target *similarities* (Davis, 1986; p. 536). Covariance-based PCA, on the other hand, is typically used when the relative magnitudes of the variables are important because its un-standardized format enhances magnitude differences and reduces the potential for an insignificant variable to exert a strong influence on the results (Davis, 1986; p. 536). Principal components analyses based on covariance matrices generate dimensions that emphasize those spectral features that best capture predominant target *differences*. It was unclear which methodology (covariance or correlation) was most applicable to band identification within the context of this research. It was assumed that both provide a different, but meaningful, perspective.

PCA was applied to the in-situ data in order to identify those bands (i.e. independent variables) that are most appropriate (i.e. have the highest component loadings) for capturing the predominant spectral differences within the 88 reflectance signatures. The 88-signature data array was directly read by SYSTAT and an unrotated PCA output was generated using both the correlation and covariance methodologies. The primary outputs of interest were the two SYSTAT output arrays defined by the number of extracted factors (dimensions) and related component loadings. The number of output factors

generated by PCA is typically held equal to the number of substantively meaningful independent patterns (extracted features) among the variables tested (Rummel, 1970). Generally, factors (dimensions) are considered meaningful if their associated eigenvalues are at or above a value of one. However, in order to remain consistent with the image-based PCA described in Chapter 2, the first six factors were extracted without examination of their associated eigenvalues.

The component loadings associated with each individual factor (dimension) were copied into a spreadsheet along with their related band number. This copying routine created an intermediate-calculation spreadsheet that contained a series of columnar loading/band number data couplets, one couplet for each of the 12 extracted dimensions (i.e. two sets of six). PCA component loadings represent a measurement of the relative degree to which each band explains the relationship between any one factor and the body of dependant variables. Therefore, a band associated with a relatively high loading explains much of the correlation/covariance captured by any one of six dimensions (factors). If a factor captured that portion of the overall data variance that is inherently related to the differentiation of botanical targets, then those bands loading highest on that factor would be well suited for botanical differentiation. These PCA-derived, band center/loading couplets provided the foundation for two

independent methodologies aimed at identifying key band-centers (i.e. wavelength domains) highlighted via PCA.

The band center/loading couplets were further manipulated to yield a graphical representation of these data. An XY-plot was generated that depicted component loading values versus wavelength (i.e. band centers). This methodology allowed the visual inspection of the loading response-curves associated with the 12 extracted dimensions. The co-plotted, response curves (i.e. loading graphs) resembled a series of spectral signatures in that they displayed spectral features (e.g. peaks, valleys, local-minima, local-maxima) across the visible and NIR wavelengths. Key wavelength features identified through the visual examination of loading curves (especially those common to several dimensions) should be most applicable to the differentiation of the botanical community from which the PCA-based signatures were generated.

The second methodology applied 2nd derivative approximations to the component loading spectra in order to identify the band centers associated with the predominant spectral features exhibited by these curves. The band centers associated with the ten highest-magnitude, 2nd derivative approximations (i.e. 5 largest positive and 5 largest negative) were extracted for each dimension after the sorting routine described above. This extraction resulted in 120 band centers (i.e. 12 dimensions x 10 values) that were then sorted in ascending order. This

allowed a histogram-like graph of these values to be generated so that the most botanically relevant (i.e. most frequently occurring) bands could be easily identified. Key wavelength features identified through the derivation of the loading curves (especially those common to several dimensions) should be particularly useful in differentiating the botanical community from which the signatures were generated.

3.2.4 Image Classifications – Bandset Optimization

Chapter four explored the relative performance of a series of classification methodologies in order to identify that which was most robust in reference to the differentiation of vegetative wetland ROIs. A Maximum-Likelihood classification generated with respect to PC-rotated imagery proved to be the best-performing methodology. In some instances, the strengths of the SAM improved the differentiation of similar spectral classes (i.e. 1-meter ROIs). No attempt was made to spectrally alter the 1-meter imagery in order to improve or streamline classification results.

The 1-meter AISA and CASI-II imagery referenced throughout chapter 2 were inappropriate for the spectral image manipulations associated with chapter 3 because their bandsets incorporate a series of non-contiguous bands (i.e. spectral gaps) across the visible and NIR regions of the spectrum. Unlike these 1-meter images, the 4-meter, CASI-II imagery (Table 2.1) contained 48

contiguous bands across the visible and NIR portions of the spectrum within no spectral gaps. Band location and width could therefore be altered without fear of encountering a spectral gap.

Table 3.2 summarizes the 21 ground-truthed, ROIs delineated within the 4-meter, Horseshoe Bay imagery. Although similar, these ROIs differ in number and pixel count from those delineated within the 1-meter, Horseshoe Bay imagery due to the method through which they were derived. When displayed, the geo-rectified 4-meter and 1-meter Horseshoe Bay imagery overlapped each other for that portion of Horseshoe Bay captured in both data sets. This overlap allowed the centroids of all pixels found in each of the 24, 1-meter ROIs (Table 2.6) were converted to an ENVI vector (point) layer. This layer was then displayed on top of the 4-meter imagery, which allowed the 4-meter pixels that fell within the boundary of the core 1-meter ROIs. In a few instances, core regions were not available in the 4-meter imagery due to the lack of image overlap. Whenever possible, these training classes were reestablished elsewhere in the 4-meter image based on knowledge of the botanical communities acquired during site visits.

The limited number of pixels identified via this vector-overlay procedure was insufficient with respect to the two constraints associated with the Maximum-Likelihood classifier, because it needs at least $n + 1$ pixels in each

training ROI, where n is the number of image bands. The 4-meter Horseshoe Bay imagery has 48 bands, so at least 49 pixels were needed in each training class ROI. The second constraint associated with ENVI's Maximum-Likelihood classifier is the need for a substantial amount of training class variance. To address these constraints, a false color composite of the 4-meter imagery was displayed in ENVI along with the core 1-meter pixels identified via the vector-overlay procedure. ENVI's interactive histogram module was then activated so that the relative intensity of the three color-channels (i.e. red = 916.7nm, green = 685.5nm, and blue = 560.1nm) could be manipulated. Each core ROI (Table 2.6) was expanded by incorporating neighboring pixels that were visually similar as revealed by color intensity manipulations. This process created 20 larger ROIs necessary for the Maximum-likelihood classifier while preserving, as best as possible, the spectral integrity of each training class. An additional class (wave foam) was added because preliminary, 4-meter classifications indicated that these pixels remained unclassified. These 21 4-meter ROIs (Table 3.2) provided the training classes for a series of supervised image classifications generated with respect to spectrally manipulated 4-meter images. Due to the nature of PCA, rotated imagery could not be used in this investigation because a complete 48-band image (i.e. non-rotated) was required. The lack of RT-DGPS ground-verification of these expanded 4-meter ROIs mandated the development of an alternative accuracy assessment strategy. A pixel-based, accuracy assessment procedure was developed with respect to the image subset

<u>ROI</u>	<u>Matrix Code</u>	<u>Scientific name</u>	<u>Pixel #</u>
1	Chara	<i>Chara sp.</i>	231
2	scirpus-dense	<i>Scirpus validus</i>	124
3	scirpus-clump	<i>Scirpus validus</i>	217
4	typha-soil2	<i>Typha angustifolia</i>	53
5	sagrigida60/40	<i>Sagittaria rigida</i>	69
6	Beachsand	<i>N/a</i>	216
7	shallowh20	<i>N/a</i>	144
8	hetdubia-delta	<i>Heteranthera dubia</i>	63
9	sagrigida-delta	<i>Sagittaria rigida</i>	92
10	Vallisneria	<i>Vallisneria Americana</i>	207
11	deeph20	<i>N/a</i>	318
12	scival-brown	<i>Scirpus validus</i>	96
13	saggram/charaROI	<i>Sagittaria graminea/Chara sp.</i>	82
14	typha-cut-island	<i>Typha angustifolia</i>	116
15	Nuphar	<i>Nuphar advena</i>	79
16	Eleocharis	<i>Eleocharis sp.</i>	97
17	Impatians	<i>Impatians biflora</i>	261
18	bluejoint grass	<i>Calamogrostis Canadensis</i>	101
19	cutgrass-eleocharis	<i>Leersia sp./Eleocharis sp.</i>	93
20	typha-phrag-scivalmix	<i>Typha sp./Phragmites australis/Scirpus sp.</i>	101
21	wave foam	<i>N/a</i>	60

Table 3.2. Horseshoe Bay, 4-meter Regions-of-Interest.

(250 x 450 pixels) displayed in Figure 3.3. A single Maximum-Likelihood and SAM classification was generated from the unaltered 4-meter imagery, and all of the 112,500 classified pixels contained in this rectangular region were treated as ground-truthed data in contrast to the field-delineated ROIs presented with respect to Investigations 1-3. These 112,500 evaluation-standard pixels were assumed to accurately represent the botanical communities found within the evaluation rectangle. This assumption could be made because its botanical

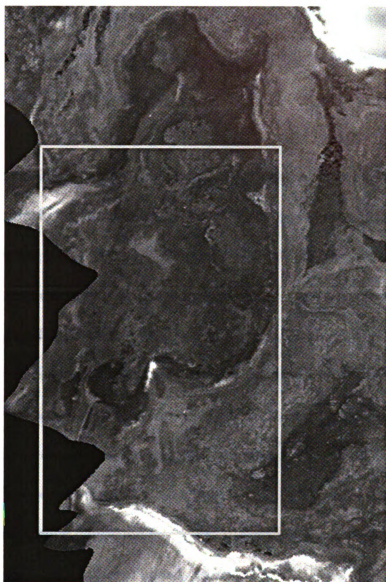


Figure 3.3. 4-meter, Horseshoe Bay Rectangular Image Subset.

validity is functionally irrelevant with respect to the focus of Investigation 4. The class specific pixel counts established via the 4-meter, baseline (i.e. 48 bands) classifications served as benchmarks so that the relative change associated with subsequent spectral manipulations could be assessed despite the lack of ground verification.

Within all of ENVI's classification modules, bands can be interactively selected for use during an image classification. Through the use of this interactive selection tool, a series of independent classifications were generated by systematically reducing the number of bands referenced during otherwise similarly configured Maximum-Likelihood and SAM classifications. The first image manipulation reduced the number of bands to seven, as guided by the predominant wavelength domains (i.e. occurrence peak) identified via the in-situ PCA and 2nd derivative methodologies. The results of these efforts identified the best performing band from each occurrence peak. A series of classifications were then generated by systematically replacing each of the optimal bands with their adjacent bands. In some instances, adjacent bands were weighted equally, or nearly so, with respect to the PCA/derivative results. Subsequent classifications were generated to further explore the trade-off between relative classification change and spectral resolution (i.e. bandset optimization). The maximum number of bands utilized was 30, which is approximately 10 more bands than found in the 1-meter AISA and CASI-II

imagery. The minimum number of bands was 4, which was selected in order to emulate the number of bands utilized by the IKONOS sensor (Table 2.2).

Classification performance was assessed through the comparison of relative change (i.e. classification resiliency) with respect to the Maximum-Likelihood and SAM evaluation-standard classification images, and confusion matrices were generated similar to Investigations 1-3. Only three matrix parameters were referenced throughout Investigation 4, overall accuracy, kappa, and the producer's accuracies for each of the 21 classes. These parameters allowed both the cumulative and class-specific classification resiliency (i.e. relative level-of-change) associated with each bandset manipulations to be addressed. The comparison of these values provided the means through which the optimal bandset associated with my Great Lakes coastal wetland imagery was identified.

3.2.5 Image Classifications – Bandwidth Optimization

A second bandset characteristic somewhat independent of band number/position is the spectral width of any one band. Assume that the PC and 2nd-derivative analyses (referencing 48 bands) correctly identified both 708.5 and 731.5 nm as the two most desirable band locations. If the bandwidths of these two bands were increased to approximately 25 nanometers, they would overlap. From a practical standpoint, sensors are not configured to capture

bands with significant spectral overlap due to the blurring of the spectral information specific to each band. If bands were allowed to overlap without removal, it is equivalent to applying a spectral smoothing (i.e. band averaging) filter across the bands. As stated in Chapter 1, wide bands tend to mask relatively subtle spectral features that potentially separate botanical classes that might only be visible with two or more bands of narrower widths. Thus, bandwidth potentially plays a critical role in the optimization of a coastal wetland remote sensing methodology.

A series of synthetically generated text files (Table 3.3) were created in which the FWHM and band number associated with the optimal bands identified via the PCA/derivative methodologies were systematically altered (e.g. 2x bandwidth). The 12x resampling resulted in bands with a width of approximately 70 nanometers, which is equivalent to the average bandwidth associated with the visible-light bands (i.e. bands 1, 2, and 3) of both the IKONOS and ETM+ sensor. Bands that are located relatively close to each would inherently be first affected by increases in bandwidth. Overlapping bands were eliminated according to their 2nd derivative occurrence frequencies. As one might expect, the potential for such band eliminations increases as the FWHM envelope around each of the optimal bands expands.

A Maximum-Likelihood and SAM classification image was generated with respect to the bandwidth-manipulated imagery using training ROIs outlined in Table 3.2. Again, where band overlap occurred, the band with the lower 2nd derivative frequency was eliminated. These classification results were compared via three confusion matrix parameters (i.e. kappa coefficients, overall-resiliency and producers-resiliency) to unaltered (bandwidth increases) classification referencing the identified optimal bands. Thus, relative classification change provided insight into the optimal bandwidth for the classification of my Great Lakes wetland imagery.

Band	original	2x	3x	4x	6x	8x	12x
Center	FWHM	FWHM	FWHM	FWHM	FWHM	FWHM	FWHM
425.4	5.7	11.4	17.1	22.8	34.2	45.6	68.4
514.9	5.8	11.6	17.4	23.2	34.8	46.4	69.6
560.1	5.8	11.6	17.4	23.2	34.8	n/a	N/a
685.5	5.9	11.8	17.7	23.6	35.4	47.2	70.8
731.5	5.9	11.8	17.7	23.6	35.4	n/a	N/a
812.3	5.9	11.8	17.7	23.6	35.4	47.2	70.8
916.7	5.9	11.8	17.7	23.6	35.4	47.2	70.8

Table 3.3. Bandwidth Manipulation FWHM Parameters

3.2.6 Image Classifications – IKONOS Spectral Simulation

The spatial resolution of monochromatic IKONOS imagery, which is the highest resolution (for multispectral imagery) currently available from a satellite platform, is 4 meters. Each of the four IKONOS monochromatic bands encompass a large portion of their respective wavelength domains, blue

(710nm), green (890nm), red (660nm) and NIR (960nm). If it is true that relatively narrow, strategically placed bands are needed to better differentiate coastal wetland plant communities, then the usefulness of IKONOS or similar broadband imagery falls under question.

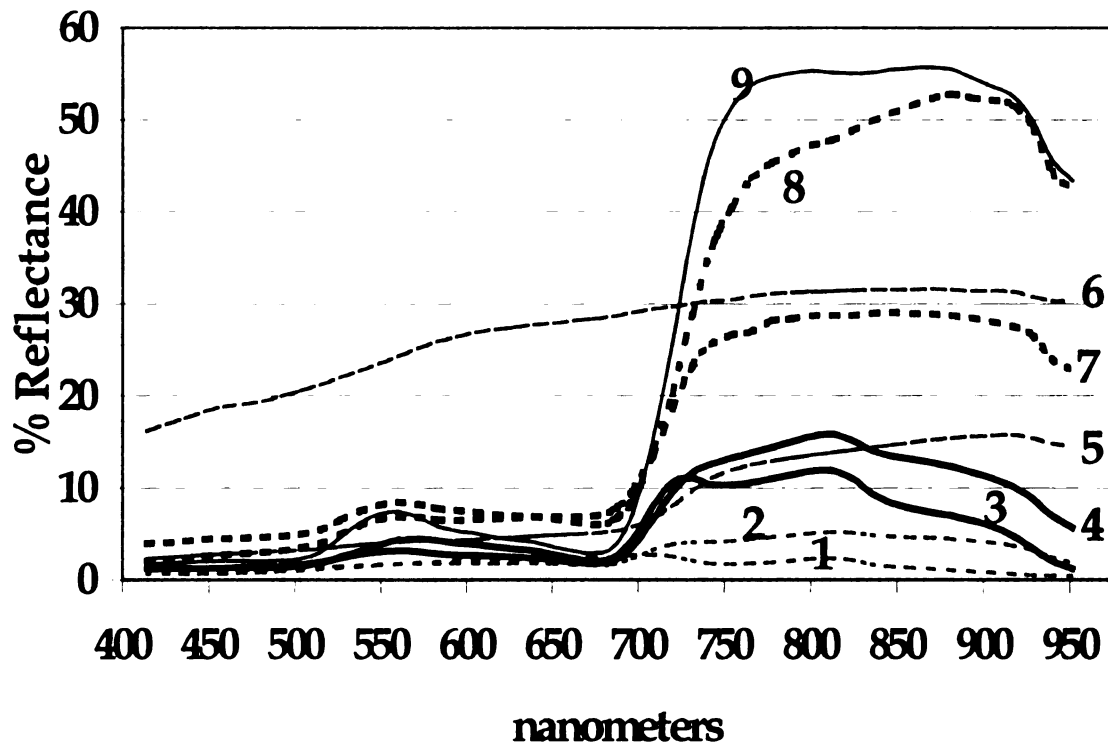
The 48-band, CASI-II imagery was spectrally resampled in reference to an ASCII text file that contained the band center and FWHM information identical to the IKONOS sensor (see Table 2.2). This process created a 4-band, pseudo-IKONOS image that emulated the bandset of the IKONOS sensor (i.e. bandwidth and band number). A Maximum-Likelihood and SAM classification was generated from this pseudo-IKONOS image using the 21 training ROIs outlined in Table 3.2. Analogous to previous sections, a confusion matrix was generated from these two classification results with respect to their appropriate evaluation standard, and kappa coefficients, overall-resiliency and producers-resiliency were extracted. These confusion matrix parameters reflect the *additive* effect of both bandwidth and band number manipulations and are directly comparable to the 4-band classification outlined in section 3.3.3. The evaluation of these confusion matrix parameters provided insight into the viability of using airborne, IKONOS-like imagery for the classification of Great Lakes wetland imagery.

3.3 Results and Discussion

3.3.1 Representative Spectral Clusters

The 96 spectral signatures referenced in Table 3.1 were simultaneously displayed in order to visually identify groups or clusters of spectra. The identification process was conducted without knowledge of the botanical class each spectral signature represented in order to reduce bias during the selection process. A representative signature was then pulled from each cluster, and their appropriate botanical information was examined. This process was not intended to rigorously group spectra based on a statistical clustering method. Rather, the intent was to explore the in-situ data to see if easily identifiable clusters existed, and if these clusters were indeed related to the characteristics of the botanical community.

Nine spectra were gleaned from the original 96 signatures, and their associated botanical information was compared (Figure 3.4). The patterns of these nine spectra encompassed the broad botanical classes making up Great Lake coastal wetland plant communities (e.g. dense-submergent, emergent, senescing emergent, substrate dominated). Since this visual inspection revealed botanically-related clusters, one would expect more advanced spectral tools and classifiers to be able to similarly, or more effectively, parse the in-situ and closely related image-ROI spectral data. The spectra shown in Figure 3.4 represent a gradient of botanical signatures ranging from un-vegetated shallow



(1 = un-vegetated shallow water; 2 = sparse submergent vegetation in shallow water; 3 = submergent vegetation in shallow water; 4 = emergent/submergent vegetation in shallow water; 5 = necrotic vegetation; 6 = gravel; 7, 8 and 9 = high biomass vegetation).

Figure 3.4. Nine Representative Spectra

water (1) to dense, herbaceous vegetation (9). When the IFOV of the SE-590 recorded the radiance (E_{\uparrow}) over a target dominated by water, the entire signature was suppressed (i.e. 1, 2, 3 and 4). Water-dominated targets should display a minimal amount of reflectance throughout the NIR region since water absorbs these wavelengths. Signature 2 represents a target that is predominantly water, but enough plant biomass was present (*Najas flexilis*) to increase NIR reflectance above that of a substrate-only, shallow water target (1).

Eelgrass/ musk-grass (*Vallisneria americana*/*Chara sp.*) beds (3) covered much of the shallow inundated regions of Horseshoe Bay during the 2000 and 2001 growing seasons. This signature was representative of shallow areas predominantly covered by submergent vegetation. Indicative of this spectral class is the double-hump pattern between 700 and 850nm. Note that signature 4 displays a similar shape, although its double-hump is suppressed somewhat by reflectance in the NIR wavelengths due to the presence of emergent and submergent biomass. Also note that reflectance in the green region (i.e. 560 nm) is slightly elevated due to the presence of more green biomass at or near the surface. An area composed of emergent *Sagittaria rigida* and submergent *Heteranthera dubia*, which covered much of the delta south of Dynamite Cut (Horseshoe Bay), was the source for signature 4.

Signatures 5 and 6 were displayed with similar line types because they exhibited relatively flat reflectance curves. Gravel (6) displays relatively constant reflectance across the visible and NIR wavelengths. Signature 5 is representative of areas dominated by senescing or necrotic vegetation. Note that it too displays relatively constant reflectance throughout the visible and NIR region, although there is still evidence of plant biomass as indicated by the steep increase in NIR reflectance beginning just beyond 700nm.

Signatures 7, 8 and 9 represent landscape facets that are completely vegetative in nature. Signature 9 exhibits the characteristic peak-and-valley reflectance pattern of high-biomass green vegetation. This signature (*Impatiens capensis*) represents one extreme of the botanical gradient, and is typified by the steepness and length of the red-edge (690-750nm). Signature 8 represents the dominant, tall-stature emergent vegetation found throughout the Great Lakes (*Typha sp./Scirpus sp.*). This signature is strikingly different from 5, (same genera, mostly non-living, brown biomass), indicative of its level of greenness. Signature 8 differs from signature 9 in three key areas: 1) flatter reflectance pattern across the visible domain; 2) lack of a pronounced red absorption feature (690-700nm); and 3) a more moderate transition into the high reflectance of the NIR. All of these traits are indicative of a significant spectral contribution from substrate, necrotic/senescent biomass, or both.

The scope of this research was not to explore every spectral nuance found in the raw in-situ data. These nine characteristic spectra suggest that digital spectral methodologies should be able to separate these signatures. In addition, the presented spectra establish a direct link between spectral reflectance properties and the biophysical characteristics of wetland plant communities. The remote sensing community is far from being able to link any one species to a specific spectral feature, but patterns exist that allow the connection between biophysical traits and remotely-sensed data.

3.3.2 2nd Derivative Summary

Figure 3.5 displays the 2nd derivative approximations of the raw signatures shown in Figure 3.1. The relative magnitudes of these 2nd derivative approximations (Appendix C) are indicative of the reflectance symmetry (i.e. parity of 1st derivative absolute values) found at the triplet center. A high magnitude value indicates distinct reflectance asymmetry at the hinge point (i.e. a diagnostic change in reflectance). The sign (+/-) of the 2nd-derivative approximations found in Appendix C indicates whether the spectral feature is local reflectance maxima or absorption minima. A positive value indicates that the band-triplet forms a localized concave or bowl-like spectral feature. Conversely, a negative 2nd-derivative value indicates a convex spectral feature. In order to form a concave feature (i.e. positive derivative value), the reflectance of the center band must be less than the reflectance vector (i.e. trend) established by its two neighboring bands (i.e. an absorption feature). A convex band triplet (i.e. negative derivative value) describes a local reflectance peak. If two band-triplet line segments have identical slopes, the calculated 2nd derivative approximation would have a value of zero. Thus, 2nd derivative values near zero are associated with a band triplet reflectance values that are either generally increasing, steadily decreasing or display very weak absorption or reflection features. The largest 2nd derivative approximations shown indicate that there was a relatively large change in reflectance within a band triplet. The five highest positive and negative 2nd-derivative approximation values

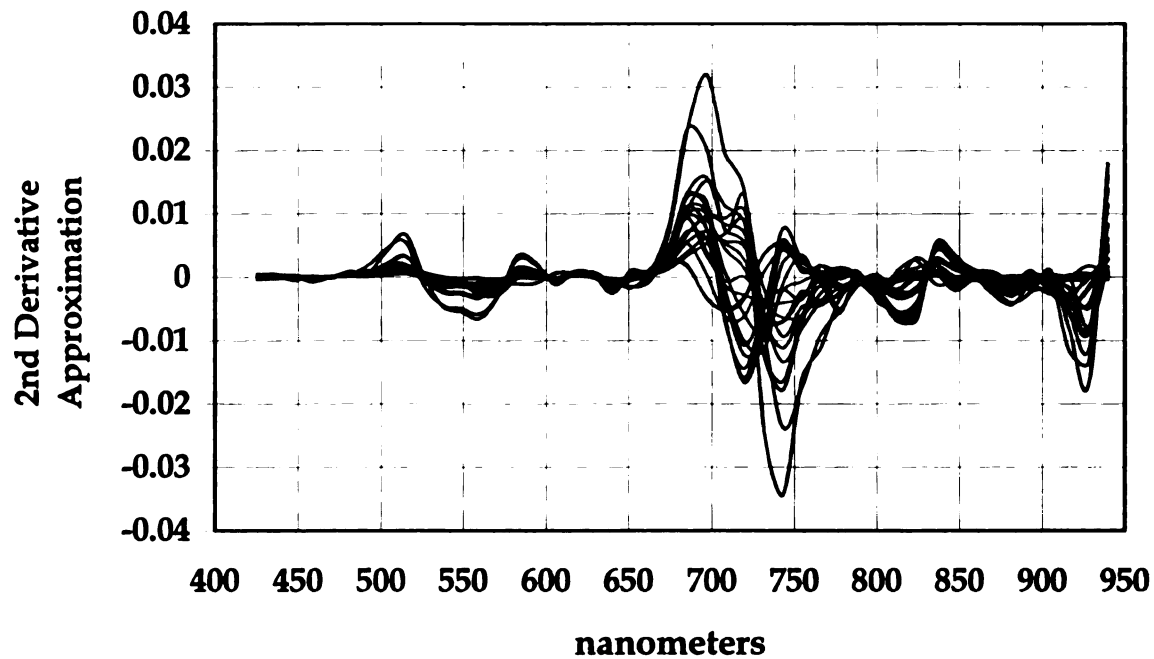


Figure 3.5. Representative 2nd Derivative Plots

generated from the in-situ data are shown in bold typeface in Appendix C.

These 10 rows mark points of inflection that are associated with the predominant absorption (+) or reflection (-) features for any given spectra. It should be emphasized that the 2nd-derivative approach outlined in this research is only applicable to contiguous, symmetric (hyperspectral) reflectance data.

The data contained in Appendix C were further refined to yield a derivative summary table. The values encountered in each of the bold rows (5 negative, 5 positive) were independently recorded, and redundant values were retained only with respect to the row in which they first appeared, creating a magnitude-ranked list of positive and negative values. The 11 wavelengths (i.e.

band centers) found within the first column of Table 3.4 represent the largest magnitude derivatives gleaned from all 88 botanical signatures. The bold typeface entries in successive columns reveal those band locations that were introduced upon examination of the next lower magnitude level. Thus, four new band centers (674.1nm, 766.1nm, 823.9nm and 835.5nm) were introduced through the compilation of the second tier (1 positive, one negative) of derivative approximations. This table summarizes the most important band centers with respect to the 88 in-situ spectra from the perspective of magnitude only. Eight band clusters or wavelength domains were subsequently identified via gaps along the wavelength continuum. The 5th cluster was further divided into its visible and NIR portions because of the marked difference in vegetative reflectance between these two wavelength domains. The resulting 9 clusters delimit the wavelength zones that were identified as most significant. It is likely that these are the spectral regions that are the most useful for differentiating wetland plant communities.

Several of the wavelength zones delineated in Table 3.4 are associated with well-known biophysical attributes. Zone one contains absorption features from a variety of plant pigments: chlorophyll-a at 420nm; chlorophyll-b at 435nm; beta-carotene at 425nm and 450nm; alpha-carotene at 420nm and 440nm; and zanthophyll at 425nm and 450nm (Kumar, 2001). Zone two contains bands that have been related to water turbidity (Shafique et al., 2001). The third zone is

<u>1</u>	<u>1-2</u>	<u>1-3</u>	<u>1-4</u>	<u>1-5</u>	<u>Freq.</u>	<u>Notes</u>
685.5	674.1	447.7	425.4	425.4	1	
697	685.5	514.9	436.5	436.5	2	Chlorophyll absorption (1)
708.5	697	651.2	514.9	503.6	20	Turbidity/ (2)
720	708.5	674.1	560.1	514.9	1	Suspended solids (510nm)
731.5	720	685.5	651.2	548.8	7	
743	731.5	697	674.1	560.1	1	Peak green reflectance (3)
754.6	743	708.5	685.5	594.1	1	(4)
812.3	754.6	720	697	651.2	3	Water absorption (5)
916.7	766.1	731.5	708.5	674.1	57	Senescent vegetation (672nm)
928.3	812.3	743	720	685.5	87	Chlorophyll absorption (6)
939.7	823.9	754.6	731.5	697	80	Senescent vegetation (690nm)
	835.5	766.1	743	708.5	59	Suspended solids (705nm) (7)
	916.7	812.3	754.6	720	52	Senescent vegetation (705nm)
	928.3	823.9	766.1	731.5	77	Water absorption (720/731nm)
	939.7	835.5	777.7	743	79	
		847.1	812.3	754.6	62	
		905.1	823.9	766.1	33	O ₂ absorption (766nm)
		916.7	835.5	777.7	11	
		928.3	847.1	800.8	1	
		939.7	905.1	812.3	21	Water Absorption (8)
			916.7	823.9	12	
			928.3	835.5	17	
			939.7	847.1	3	
				870.3	1	(9)
				881.9	1	
				893.4	2	
				905.1	2	
				916.7	55	
				928.3	62	
				939.7	71	

Table 3.4. In-situ 2nd Derivative Summary

associated with the green reflectance peak from vegetation. The spectral region comprising zone four is sensitive to yellow-green or yellow reflectance. The single band comprising zone five (651.2nm) has been related to a weak water absorption feature and with absorption by monochromatic chlorophyll-a (Shafique et al., 2001). Reflectance in zone six is dominantly controlled by chlorophyll absorption. As such, these bands are sensitive to the relative amount of green vs. brown biomass in each pixel. Carter (1993) found a significant sensitivity to plant senescence at 672nm and 690nm.

In the first NIR zone (708.5 - 777.7nm), several biophysical controls may modulate reflectance. Shafique et al. (2001) found weak relationships between reflectance at 705nm and concentrations of total suspended sediments and trichromatic chlorophyll-a. The strongest, short-wavelength water absorption feature is centered at 722nm. Since green vegetation strongly reflects the NIR wavelengths, the 720nm band is undoubtedly sensitive to the amount of standing water within a pixel. The 766.1nm band may be overly influenced by the strong oxygen absorption feature located between 760 - 765nm. Zone eight encompasses a spectral region of maximum reflectance by green vegetation, although a weak water absorption feature occurs near the 812.3nm band. Many of the submergent vegetation types achieve their peak reflectance in this zone. Zone eight is also where many of the senesced, large-stature emergent genera achieve their peak reflectance.

Overall reflectance from water is very low throughout the NIR portion of the spectrum. A distinct, strong, in-vivo water absorption feature is obvious in vegetation spectra at 960nm. Its affect helps to suppress vegetative reflectance across zone nine. Dehydration usually accompanies senescence, so reflectance associated with zone nine is related to the amount of brown biomass in the pixel.

The results presented in Table 3.4 were based solely on relative magnitude, without reference to the frequency of occurrence for any single band-center. Some of the presented band-centers occurred only once among all 88 signatures, and, therefore are not likely to be as botanically important as ones that occurred frequently. The histogram presented as Figure 3.6 was constructed from 880 of the 960 derivative values (i.e. 88 vegetative spectra x 10 values) shown in Appendix C; these 880 values did not contain any non-vegetative spectra. The values were sorted with respect to wavelength in order to record the number of occurrences associated with each of the band centers. This frequency analysis highlighted several key band locations or wavelength clusters. Assuming that these 88 signatures captured the spectral essence of the typical coastal-wetland plant communities, then the bands highlighted in both Table 3.4 and Figure 3.6 represent the most powerful bands with respect to botanical differentiation.

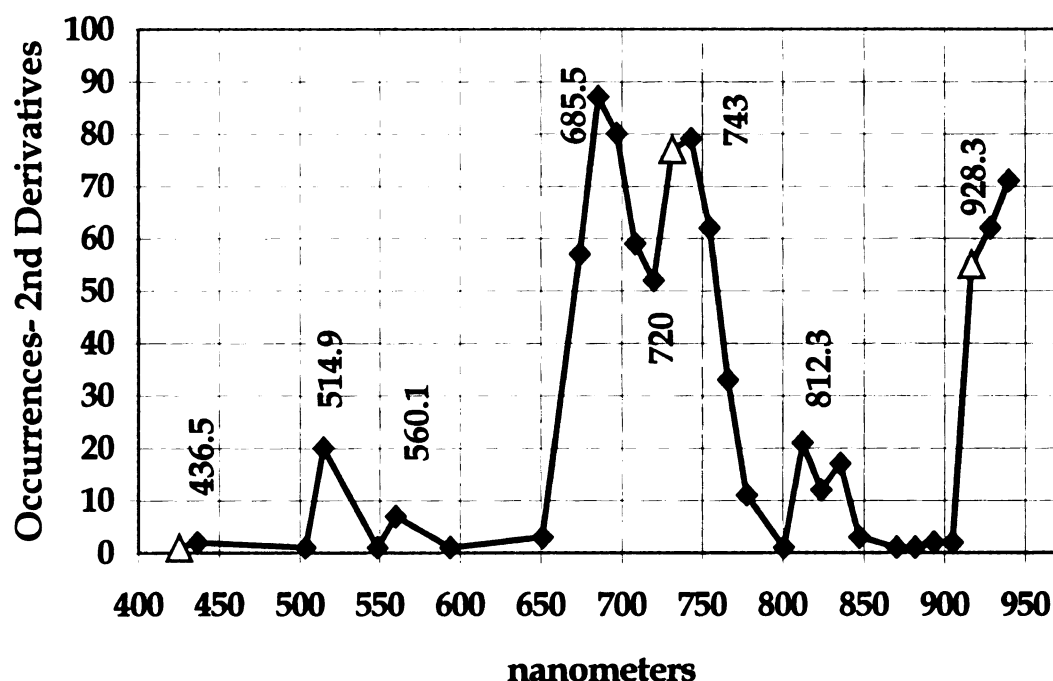


Figure 3.6. Frequency of 2nd Derivative Occurrences

It was beyond the scope of this research to systematically examine the raw spectra and their related derivatives in order to identify unique patterns that could be linked to the biophysical nature of the sampled plant community. However, patterns have emerged that link certain derivative signatures with particular wetland cover types and their associated biophysical characteristics. Pure water displays a narrow absorption feature centered at 722nm, so it would be expected that the signatures of targets dominated by standing water (e.g. submergent species) would exhibit an absorption feature associated with this wavelength. In contrast, the presence of green biomass causes pronounced NIR reflectance. Therefore, a strong absorption feature at 720nm (the actual band center used on the CASI-II instrument) in *combination* with elevated NIR

reflectance (i.e. 731.5nm) could be used to identify submergent vegetation.

Signature 3 [eelgrass/ musk-grass (*Vallisneria americana*/*Chara sp.*)] (Figure 3.4) exhibits a double-hump pattern that is associated with the contrast in reflectance properties of the 720nm and 731.5nm bands, a pattern highlighted by derivation. Much more work is needed to explore the species-specific nuances of the derivative approximations shown in Appendix C.

3.3.3 PCA Loading Curve Inspection

When applied to the in-situ reflectance spectra, Principal Components Analysis (PCA) generated band-specific component loadings. These component loadings measured which independent variables (the bands) were involved with which meaningful dimension and to what degree; they can be viewed much like correlation coefficients (Rummel, 1970). Since the meaningful dimensions functionally encapsulated all (>99%) of the spectral variance of the botanical spectra (dependent variables), the loadings identified the descriptive power of all 48 bands within the context of the six meaningful dimensions.

Within the derivative methodologies described in the previous section, each individual signature was treated as an independent entity, so the results associated with a particular signature could be evaluated. This is not the case with component loadings, since they are generated with respect to the

combined characteristics (variance) of the dependent variables. Because the dependent variables (i.e. botanical spectra) are treated jointly within PCA, it is extremely data dependent. It is therefore impossible to isolate the component loading associated with a specific spectral signature. Factors scores, which were also generated, are specific to each individual dependent variable (spectra). PC factor scores describe the proportionally weighted involvement of each dependent variable (i.e. botanical spectra) in each meaningful dimension (Rummel, 1970). Factor scores only explain the relationship between the orthogonal factors and a specific spectral signature, without reference to individual independent variables (i.e. bands). Since the goal of my in-situ PC analyses is to help identify those bands that best differentiate botanical classes (analogous to derivative methodologies), factor loadings, and not factor scores, are directly applicable.

Appendix D contains the raw SYSTAT output from both the correlation- and covariance-based PCA transformations, including dimension specific statistics (e.g. variance explained) and band-specific component loadings. The first strategy applied to the baseline PCA data shown in Appendix D was graphical in nature. Figure 3.7 contains the raw (i.e. unsorted) component loadings generated with respect to the 88-member in-situ data (i.e. gravel-like signatures removed). The 12 curves correspond to the 6 extracted dimensions associated with both the covariance- and correlation-based PCA methods. No

attempt was made to emphasize the meaningfulness of either PCA methodology, and it was assumed that the results generated from both methodologies were meaningful with respect to the identification of key band centers. One or more of these signatures mimic the characteristic peak-and-valley reflectance pattern associated with vegetative spectra. This is strong evidence that these dimensions are closely linked to the botanical nature of the input signatures.

Superimposed on Figure 3.7 are a series of bars labeled according to the band center over which they are centered. The bars were systematically placed in order to identify the most visually-significant spectral features common throughout the 12 meaningful dimensions. In some instances, a bar could be shifted in order to encompass an adjacent spectral feature and band-center. For example, one could argue that the 708.5nm band could be shifted to the right, and relabeled as 720 nm. However, the displayed bars identify (by visual inspection means) the most significant wavelength domains with respect to the various spectral features exhibited by the component loading curves. This was not a rigorous mathematical process to identify significant spectral features. However, the band-centers identified by this simple method correspond well with those bands having the highest occurrence values shown in Figure 3.6. At a minimum, the features identified by the visual inspection of the component loading curves are likely to be botanically relevant bands.

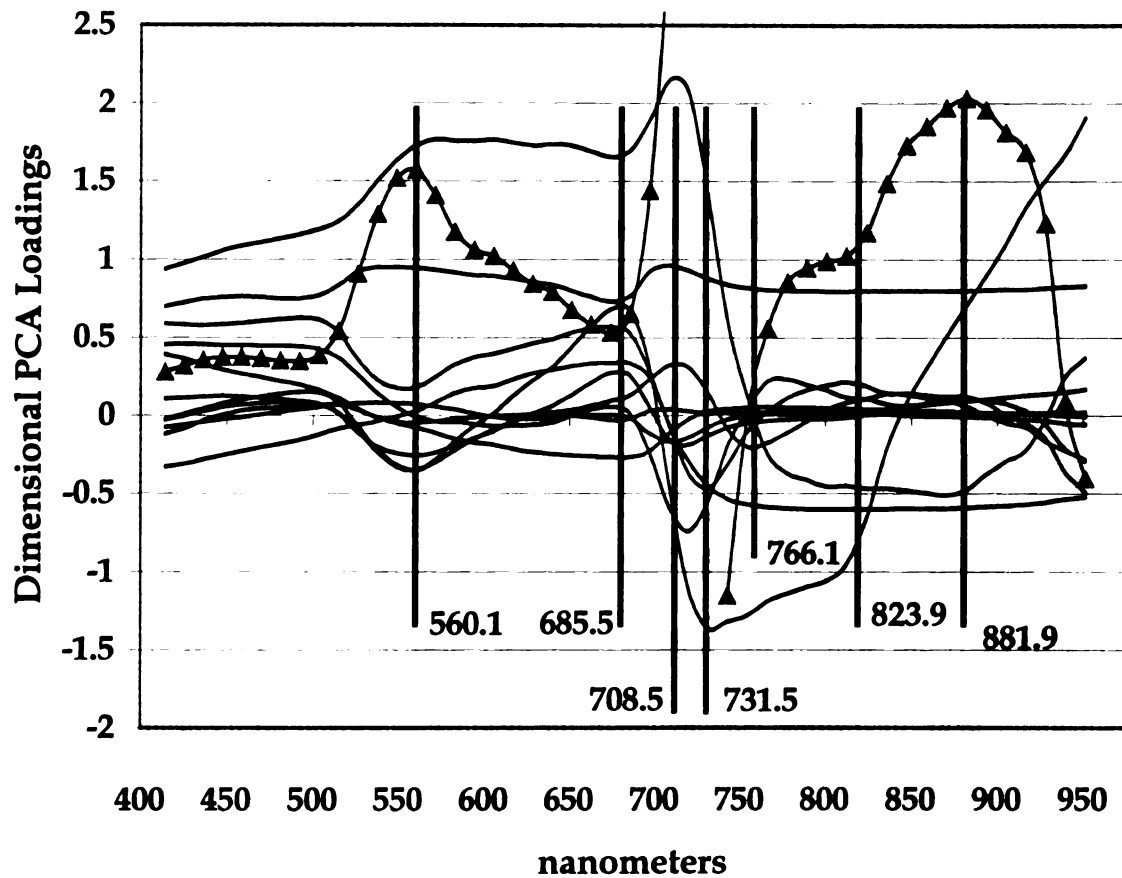


Figure 3.7. Key Wavelength Domains - Dimensional PCA Loadings.

(Note: Covariance PC1 (▲) has been broken at 710nm and shifted downward approximately 13 loading units so it could be displayed)

3.3.4 Loading Curve Derivation

A second strategy was applied to the PCA output arrays shown in Appendix D. This more formal mathematical approach was designed to address any shortcomings associated with the visual methodology described in the preceding section. The component loading curves were subjected to the 2nd derivative approximation methodology outlined in section 3.3.2. Analogous to the approach used to generate Figure 3.6, the 10 highest-magnitude, derivative

values (i.e. 5 + and 5 -) were compiled so that a frequency histogram could be constructed (Figure 3.8). The overall patterns exhibited are very similar to the patterns shown in Figure 3.6. Six occurrence-peaks are common to both graphs, centered at approximately 515nm, 560nm, 685nm, 720nm, 823nm, and 940nm nanometers. These six band centers wavelength domains are essential with respect to both the PCA and derivative analyses.

Table 3.2 presented nine distinct wavelength domains that contained botanically relevant information. Viewing Figures 3.6, 3.7 and 3.8 with respect to these independent wavelength regions, the optimal band (i.e. most occurrences) in each region was systematically selected. In addition, the relative strength of each region can be assessed based on their relative frequency of occurrence. Applying this strategy, the 685.5nm and 720nm band centers are the two most important bands within the context of this research. These are followed in significance by the 607nm and the 731.5nm bands. Assuming the 88 in-situ signatures utilized to generate Table 3.2 and related 2nd derivative figures sufficiently captured the spectral essence of a typical Great Lakes coastal wetland plant community, then the redundancies found in these data suggest that the identified band-centers are the most botanically relevant.

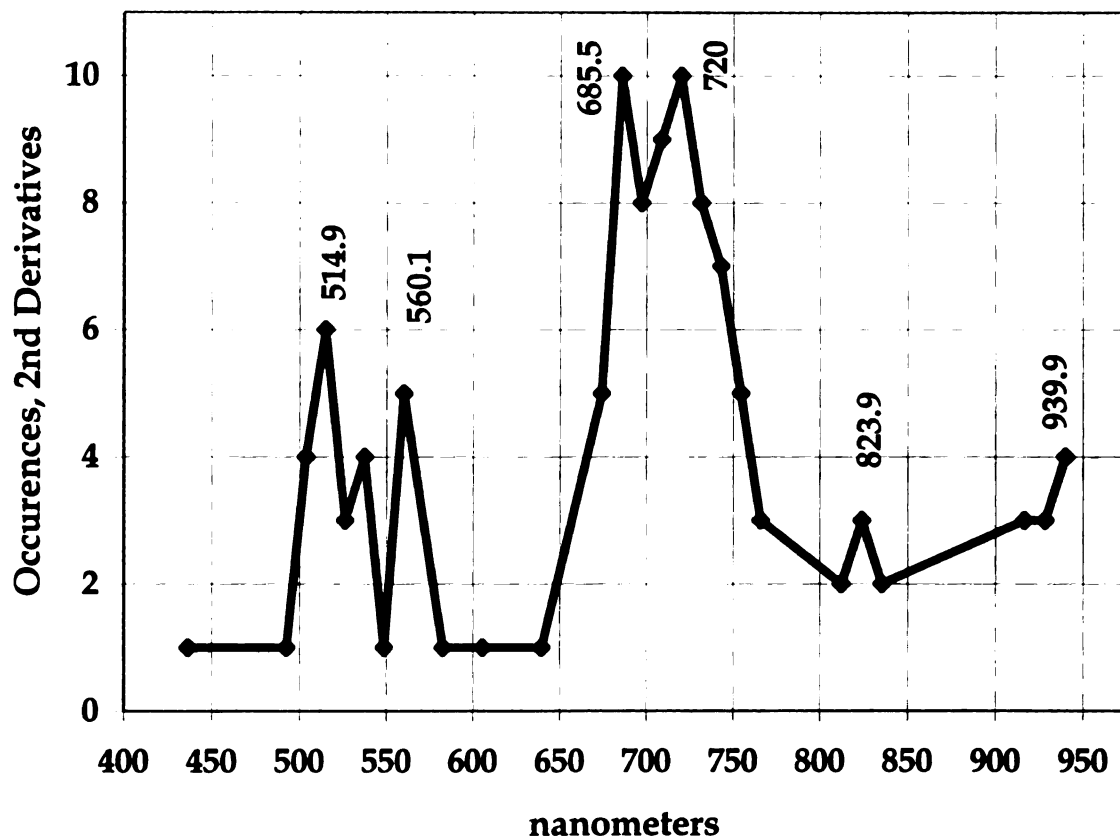


Figure 3.8. Frequency of 2nd-Derivative Occurrences of Loading Curves.

3.3.5 Correlation-based, PCA Factor Interpretation

Kauth and Thomas (1976) derived a modified Principal Components rotation (Tasseled Cap) for Landsat MSS data in which the majority of target variance is captured in the first two dimensions (Lillesand and Kiefer, 1994; p. 577). These two dimensions have become widely recognized as Brightness and Greenness. Brightness, which is also called n-dimensional albedo, is the weighted sum of all bands in reference to the principal variation of soil reflectance. The second component, greenness, contrasts reflectance in the

visible versus NIR wavelength regions, and is strongly correlated with the amount of green vegetation in the scene. One could argue that the second dimension should be called non-greenness, since the component loadings (i.e. transformed eigenvectors) are negative for the NIR bands. Green vegetation (with its maximum reflectance in the NIR) is inversely related to the second dimension. Further studies have assigned meaning to a limited number of additional dimensions (i.e. 3rd = wetness) with respect to 6-band Landsat TM data (Crist and Cicone, 1984).

As presented in earlier sections, the results of PCA are inherently dependent on whether a covariance or correlation matrix is used. Covariance-based PCA, (i.e. non-standardized) is more sensitive to the extremes of the data, because it both preserves and utilizes the entire magnitude range of the data. In contrast, correlation-based PCA (i.e. standardized) suppresses patterns within the magnitude range of the data, and places more emphasis on data similarities. Because of this fundamental difference, the factors generated via both methodologies are discussed separately.

Figure 3.9 displays the correlation-based dimensions generated from the 88 spectra referenced throughout this research. These curves are identical to those presented in Figure 3.7, but the scale was changed to aid in their interpretation. In order to better interpret the biophysical meaning of the correlation-based

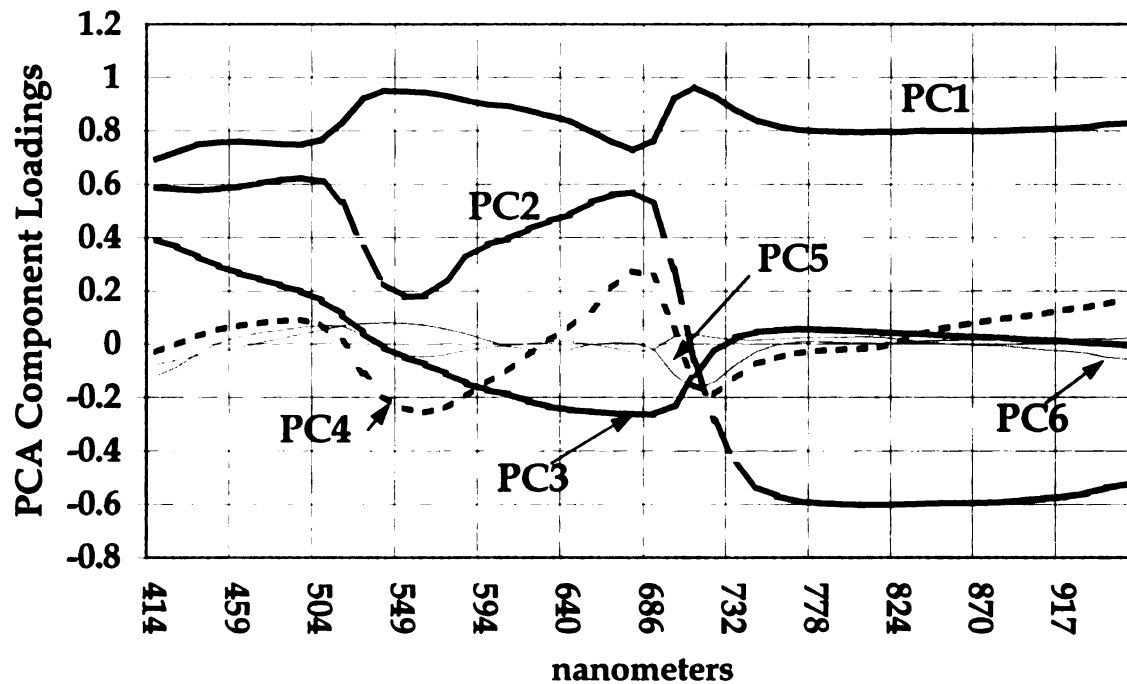


Figure 3.9. Correlation-based, PCA Component Loading Curves.

dimensions, it is helpful to visualize a hypothetical reflectance continuum for the 88 spectral signatures. Three broad categories of cover types are found in Horseshoe Bay -- water, soils and vegetation, and the original 96 signatures captured the essence of each. If placed along a continuum of relative reflectance across all 48 bands, dry, sandy substrates would be the most reflective surfaces across all bands. Water-dominated targets, on the other hand, would be the least reflective surfaces across all 48 bands. Eight signatures were removed from the original 96 because they were non-vegetative; these contained the extremes of this hypothetical continuum. The remaining 88 vegetative signatures would fall somewhere in between these two

extremes, depending on the level of vegetative biomass, both green and dead, and its associated percent cover. A sparsely-vegetated, sandy shoreline would be near the bright end of this continuum.

The characteristic that all of the signatures have in common (i.e. high correlations among all the variables) is their brightness along this continuum. Not surprisingly, the 1st dimension that captured 68.28% of the total variance, can be interpreted as n-dimensional brightness. However, it is n-dimensional brightness within the context of a vegetation-dominated data set or landscape. Note that the highest loads are associated with the green peak (549nm) and the NIR maxima (710nm). The amount of vegetation present is playing a secondary role in this dimension. Examination of the factor scores associated with this dimension further demonstrated that it is related to brightness, albeit seen through a vegetative filter. The variables that scored lowest were the pure water, (i.e. very dark pixels). Variables with relatively high biomass, either terrestrial or emergent/submergent, displayed the highest scores.

The loading plot associated with the second dimension is reminiscent of an inverted peak-and-valley reflectance signature typical of vegetation. This dimension, which captured 29.69% of the total variance, is associated with greenness. Healthy green vegetation has two reflectance peaks, one centered near 560 nm (i.e. green) and the other associated with the NIR wavelengths.

Note that in Figure 3.8, these wavelengths coincide with the lowest relative loadings. To illustrate the non-greenness attribute associated with this second dimension, note that the most “green vegetation” signature (*Impatiens capensis*) of all the in-situ data (*Impatiens capensis*) produced the largest, negative component score for component 2.

The component loadings associated with the 3rd dimension, which captured 2.83% of the total variance, are also closely linked to the biophysical characteristic of the plant communities sampled. The shape of the 3rd-dimension curve (Figure 3.9) is a mirror- image of one from a very yellow reflector (i.e. steadily increasing reflectance across the longest of the visible wavelengths yellow, orange and red). Note that all of the loadings for components 3-6 are near zero in the NIR. This is because the contributions of the NIR wavelengths have already been accounted for in the first two components. Although PC3 captured a relatively small percentage of the overall data variance, this dimension appears to emphasize target “non-yellowness”. In the 3rd dimension, factor scores for blooming goldenrod (*Solidago sp.*) and sunflower (*Helianthus sp.*) were the two highest magnitude, negative values on this dimension.

The 4th dimension (1.60% of the total variance) appears to represent target brownness or dead biomass. Note the relatively high contribution of

orange/red (i.e. 650-690nm) reflection coupled with a lack of green (550nm) and a distinct drop in NIR reflectance on the shoulder (700-720nm) of the NIR region. Brown biomass, especially if moist, would exhibit such a reflectance pattern. Brown (necrotic) biomass spectra from multiple genera and blooming common reed (*Phragmites australis*) were associated with the highest magnitude, positive factor scores on PC4. Note that the blooms of the common reed were a deep brown color during spectral sampling, which further substantiates the notion that dimension 4 is related to spectral brownness. Many of the submergent cover types, especially those with relatively sparse vegetation, displayed the highest negative factor scores on PC4. These spectra would have some brownness due to the spectral contribution of their substrate, but would certainly have some green and NIR reflectance making their reflectance spectra distinctly “not brown”. This dimension (PC4) might be useful in identifying low-biomass submergent plants.

The loading pattern of PC5 suggests that this dimension is associated with targets exhibiting a minor green reflectance peak coupled with a sag in NIR reflectance just in the NIR-shoulder region (700-720nm). Although the sixth dimension was included in previous discussions, no attempt was made to interpret its biophysical meaning due to the relatively low amount of target variance it captured and its near-zero loading pattern.

3.3.6 Covariance-based, PCA Dimension Interpretation

Figure 3.10 depicts the loading patterns of the covariance-based dimensions generated from the 88 spectra referenced throughout this research. Again it is helpful to think of a reflectance continuum to aid in interpreting these patterns. The continuum described previously with reference to the correlation-based results was oriented in order to best capture similarities associated with the variables. A covariance continuum, in contrast, is oriented to enhance the most-striking differences among the variables. The highest magnitude reflectance change found throughout the 88 spectra contrasts minimum reflectance in the short-wavelength visible with maximum reflectance in the NIR. The most luxuriant vegetation targets would represent one extreme along this covariance continuum. Non-vegetative, flat reflectors (e.g. open water or muck) represent the other extreme along this covariance continuum. The NIR portion of the first covariance dimension was eliminated from Figure 3.10 in order to display the remaining five dimensions at a scale that would enhance the interpretability of the patterns.

The loadings associated with the first covariance dimension mimic the characteristic, peak-and-valley reflectance signature typical of vegetation. This dimension, which captured 96.87% of the total variance, can only be interpreted as being sensitive to green foliar biomass. Healthy, green vegetation has two reflection peaks, one centered near 560 nm (i.e. green peak) and the other

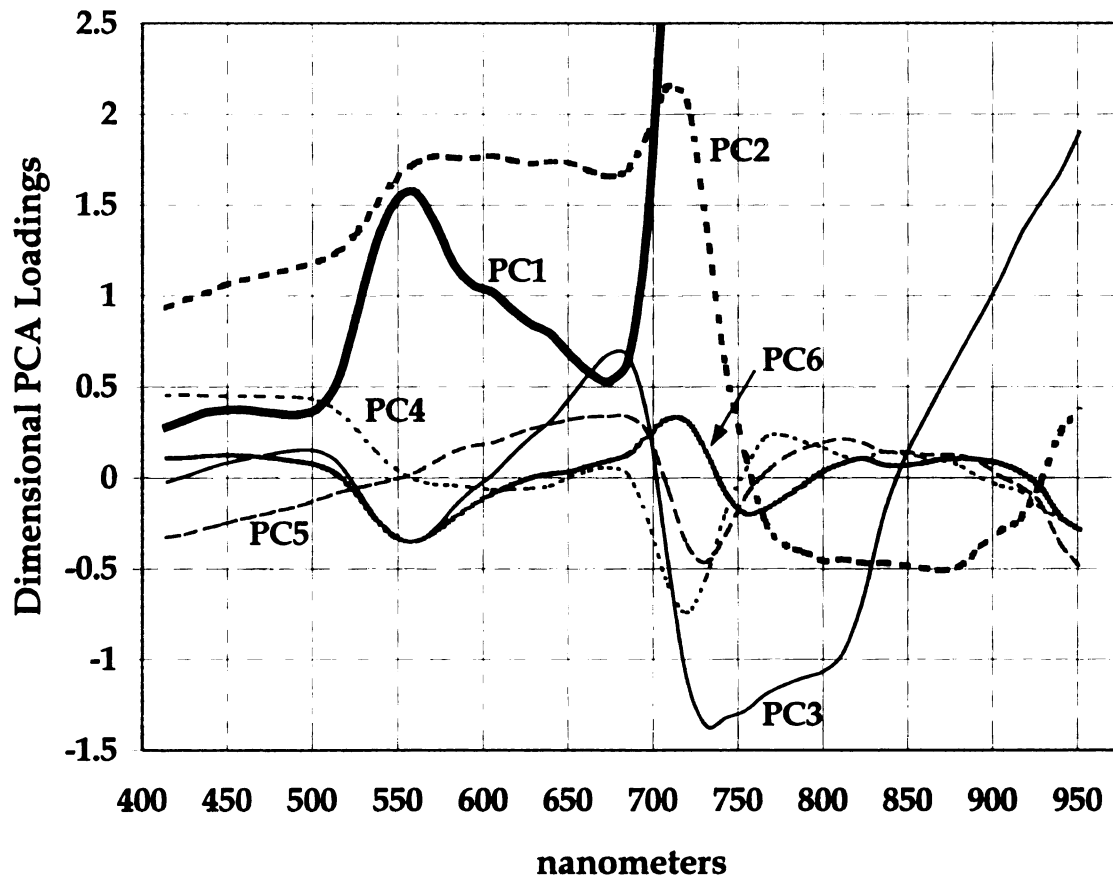


Figure 3.10. Covariance-based, PCA Component Loading Curves

associated with the NIR wavelengths. The overwhelming majority of target variance was captured by this dimension, indicating that the contrast between visible and NIR reflectance can be the foundation for differentiating virtually all of the 88 spectral signatures. The most “green” signature (*Impatiens capensis*) found throughout all of the in-situ data produced the largest, positive factor score on $PC1_{cov}$. Water covered sand, an extremely flat reflector (i.e. no visible/NIR contrast), exhibited the highest magnitude negative scores on $PC1_{cov}$.

The covariance-based, 2nd dimension seems to be indicative of targets with mildly elevated reflectance in the yellow-green portion of the spectrum coupled with a minor red-absorption feature and a reflectance peak at the NIR shoulder. Also striking in this pattern is the rapid decline in reflectance at wavelengths beyond about 725nm and relatively stable reflectance across the visible wavelengths. This dimension is associated with floating-leaf vegetation. A water-dominated, but relatively green, target such as *Nuphar advena* would exhibit such a spectral signature. The absorption of the NIR wavelengths beyond 725nm is due to standing water in the field-of-view. The presence of interspersed green biomass in the form of floating leaves is responsible for the subtle, broad yellow-green peak coupled with red-light absorption and the short-wave NIR reflectance maximum. The highest positive scores related to this dimension were the water-dominated, floating-leaf communities.

The 3rd covariance dimension, which captured 0.82% of the total variance, appears to be related to dry, brown biomass. Note the lack of green reflectance (negative loadings around 550nm) coupled with increasing reflectance across the orange/red (i.e. 650-690nm) portion of the spectrum and the distinct drop (to a maximum negative load) in NIR reflectance. Another notable feature of the loading pattern of PC3_{cov} is the increasing reflectance in the NIR beyond about 825nm. This increase suggests that the brown biomass is desiccated and that little or no water is showing through from below. Brown (necrotic)

biomass spectra from multiple genera were associated with the highest positive factor scores on PC3_{cov}. The submergent and water-dominant emergent cover types were associated with the highest negative factor scores on this third covariance dimension. In addition, the most-green signatures (e.g. *Impatiens capensis*) found throughout the 88 spectra were also negatively associated with this dimension. The patterns associated with the first three covariance dimensions suggest a practical use. To differentiate wetland plant genera, one approach could involve finding differences associated with their greenness, brownness, and substrate co-dominance.

Generically, the percentage of variance explained by lower-order PC dimensions (i.e. dimensions 4, 5, and 6), especially covariance-based, is minimal. The patterns associated with these lower-order dimensions are inherently difficult to interpret because they must be viewed as being completely independent of the higher-order patterns. For example, the covariance-based PC1_{cov} dimension is clearly linked to healthy green biomass. Therefore, all lower-order dimensions (2 through 6) must be interpreted independently of target “greenness” because this multispectral attribute has been sequestered into only the first dimension. Interpretations of the loading patterns associated with PC4_{cov}, PC5_{cov} and PC6_{cov} were not practical because of the level of inconsistency associated with their factor scores and the inability to assign meaning independent of their higher-order counterparts.

3.3.7 Bandset Optimization – Investigation 4

Three pools of data were generated via the in-situ PCA and 2nd derivative methodologies to identify key band locations (Figures 3.6, 3.7, and 3.8; Table 3.4). This information was utilized to systematically reduce the number of bands referenced during the Maximum-Likelihood and SAM classifications of the 4-meter, CASI-II imagery. Analogous to earlier sections, the classification error matrices (Appendix B) were summarized and presented in tabular form (Table 3.4). The three sections in Table 3.5 reference the three components of Investigation 4, and were sorted in descending order so that the relative performance of each classification outcome could be easily compared. The overall-resiliency values found in Table 3.5 reflect a pixel-by-pixel assessment of classification change resulting from bandset manipulations. Again, the calculation of a variance value for each Kappa Coefficient allowed a Z-test (Congalton et al., 1983) to be conducted between all paired classification outcomes. A select group of classifications in Investigation 6 were not statistically different from one another at the 95% confidence limit, and their classification identifiers were preceded with one or more asterisks (see Table 3.5 footnote). The bulk of the results presented in Table 3.5 references only SAM classifications. Maximum-Likelihood, which is a probability-based classification tool, responded poorly to the band reduction strategies. A limited number of Maximum-Likelihood classifications were generated and their associated results were only briefly discussed. Thus, bandset reduction

Investigation 4A Classification	Overall Resiliency	Kappa Statistic
SAM4ikonos	67.74%	0.6522
SAM4band	79.64%	0.7807
SAM7-939	82.49%	0.8111
SAM7-720	83.52%	0.8223
*SAM7-674	85.35%	0.842
*SAM7-743	85.65%	0.8452
**SAM7-548	86.09%	0.8501
***SAM7band	86.27%	0.8519
***SAM7-823	86.26%	0.8519
SAM30band	90.15%	0.8937
SAM24band	94.09%	0.9362
Max7band	59.46%	0.5609
Max24band	73.72%	0.7148
Max30band	78.72%	0.7683
Investigation 4B Classification	Overall Resiliency	Kappa statistic
MAX-2x	60.23%	0.5691
MAX-6x	62.58%	0.5950
*MAX-8x	55.84%	0.5223
*MAX-12x	55.76%	0.5216
SAM-2x	86.44%	0.8538
SAM-6x	87.33%	0.8633
SAM-8x	84.87%	0.8364
SAM-12x	83.96%	0.8265
Investigation 4C Classification	Overall Resiliency	Kappa statistic
SAM_pseudoIKONOS	71.54%	0.6926
IKONOS_SAM_16classes	77.78%	0.7605
<p>*, *** = statistically identical ** = different from SAM7band @ .70 confidence limit</p>		

Table 3.5. Summary of Investigation-4 Classifications

strategies are accompanied with an initial reduction in accuracy due to the need to focus on the SAM classifier.

3.3.7.1 Optimal Band Location – Investigation 4A

Seven predominant wavelength domains were identified via all four band-location approaches (i.e. Table 3.4, Figures 3.6, 3.7 and 3.8), and are distinctly visible in Figure 3.6. Seven bands were identified that outperformed all tested band combinations: 425.4, 514.9, 560.1, 685.5, 731.5, 812.3 and 916.7 nanometers, which became the benchmark (i.e. *SAM7band*) against which additional classifications were compared. Again, relevant confusion matrices are found in Appendix B. In some instances, the best performing band pulled from each wavelength domain was not the most frequently occurring band. The overall-resiliency value of the benchmark, 7-band SAM classification was 86.26%, indicating that approximately 13% of the pixels were classified differently upon the removal of 41 of 48 bands. Examination of the *SAM7band* producers-resiliency values in Appendix B reveals that eight classes, in three groups (2, 4, 16, 17, 18 and 19; 8; 11), represented the vast majority of classification change. The first group (highly green) displayed relatively poor classification results due to cross-classification among themselves. These classes are the most-green training classes, and one or more bands needed to improve their differentiation were removed. The second group (class 8), which represents a submergent species, similarly cross-classified with other submergents. The third group

(class 11), which was the deep-water class, cross-classified almost exclusively with the shallow-water class (i.e. class 7). These findings are consistent with the more detailed discussion of SAM classification results found in Chapter 2 that illustrated the fundamental weakness of the SAM classifier: within-class errors.

SAM is a non-probability-based classification tool that separates image spectra according to a cumulative angular coefficient that is derived from each spectral data point (i.e. hinge point). Fundamentally, there exists an inverse relationship between the number of bands and the probability of a key band associated with a subtle spectral feature needed to differentiate one or more classes being removed. If only two bands were used, each spectrum would be reduced to a single, decision-space vector, and all subtle features would be lost. Inversely, the utilization of the maximum number of bands would ensure all the recorded, subtle features would contribute during a SAM classification. A functional classification can be generated with a significantly reduced number of bands, but the ability to distinguish within-class species or cover types is reduced. As mentioned in Chapter 1, Wang et al. (2000) achieved an overall accuracy of 84% utilizing SAM to classify relatively broad botanical associations (e.g. reed association, *Carex* association) using hyperspectral imagery. The use of broad associations reduces the potential for within-class cross-classification because the classes have been homogenized. The eight classes that contributed most to the SAM7band classification change could have been regrouped into

several more broad associations in order to improve the overall classification outcome. However, to reduce classification errors associated with my more botanically detailed classes, more than these seven optimal bands are needed. Thus, a trade-off exists between the number of bands and the desired level of accuracy.

Additional 7-band SAM classifications were shown in Table 3.5 to illustrate how relative classification change was affected by utilizing alternative bands. For example, Figure 3.6 indicates that a band centered at 939.9nm would be the best choice within its occurrence peak. A 7-band classification that included 939.9nm instead of 916.7nm (i.e. SAM7-939) under-performed the SAM7band classification by approximately 4%. The band centers 812.3nm or 823.9nm are functionally equivalent, and can replace one another without any change in classification outcome. Similarly, 548nm can be incorporated without a significant reduction in classification change. The ability to shift to adjacent bands without experiencing major classification falloff attests to the level of information redundancy inherent to the occurrence peaks (Figure 3.6).

Two 4-band SAM classifications were also generated. The first incorporated, as closely as possible, the band centers (but not the bandwidths) of the IKONOS sensor (i.e. SAM4ikonos). Over 30 percent of the evaluation-standard pixels classified differently when only these 4 bands were utilized. In

contrast, a second 4-band classification (i.e. SAM4band) that referenced the best-performing band from the four highest-magnitude, occurrence peaks shown in Figure 3.6 (i.e. 514.9, 685.5, 731.5 and 916.7nm) exhibited an overall-resiliency of nearly 80%, approximately 13% higher than SAM4ikonos. Thus, with respect to classifying the representative botanical communities captured by the 4-meter Horseshoe Bay imagery, the IKONOS sensor band centers are not as useful as these four bands.

The final two SAM classifications shown in the first section of Table 3.5 were included to further emphasize the importance of band positioning. At first glance, one might assume an error occurred during the preparation of Table 3.5 because it seems logical that the 30-band classification should have outperformed its 24-band counterpart (i.e. SAM24band). However, as the results illustrate, this was not true. The bands incorporated into the 30-band classification (i.e. SAM30band) were the list of bands contained in the last column of Table 3.4. The 24-band classification more simply incorporated every other band beginning with 425.4nm. Subtle spectral features that contributed to the extremely high overall-resiliency of the SAM24band classification are associated with one or more bands found outside of the nine predominant wavelength domains. The derivative and PCA methodologies did indeed identify a subset of bands that are most responsible for the differentiation of the 21 training classes. Spectral features that remained unidentified via these

methodologies are needed to achieve very high classification-resiliency. A hyperspectral bandset, one systematically covering the visible and NIR wavelengths, is best with respect to the differentiation of the botanical ROIs referenced in Investigation 4.

The Maximum-Likelihood classifier significantly under-performed the SAM classifier within Investigation 4, thereby establishing that band reduction strategies are classifier specific. The nearly 30% difference in classification-resiliency between the SAM7band (86.26%) and the Max7band (59.46%) classifications initially questioned the transferability of the seven optimal bands identified above. However, the seven bands identified above also resulted in the best-performing Maximum-Likelihood classification. Note that the resiliency associated with the best-performing Maximum-Likelihood classification (i.e. Max30band) is largely equivalent to the SAM4band classification. It seemed surprising that a 4-band and 30-band classification of the same image would generate comparable results. However, Maximum-Likelihood is a probability-based classification tool unlike SAM, and it proved to be very sensitive to the removal of bands. In light of these results, the falloff in classification-resiliency must be associated with the inherent properties of the classifier itself.

Although it is difficult, if not impossible, for a person to visualize beyond three dimensions, computer-based tools like the Maximum-Likelihood and Mahalanobis-Distance classifiers are able to accomplish multidimensional evaluations. Probability-based classifiers establish a distribution of spectral classes within a decision-space defined by the number of bands (i.e. dimensions) utilized during the classification. Class distributions are stretched and pulled apart along the axis of 48, independent dimensions in the case of my 48-band imagery. As the number of bands is reduced, n-dimensional space is reduced, forcing the class means and their associated probability distributions into a more narrowly defined space. In light of this, the removal of 41 bands (i.e. Max7band) would likely have a significant impact on any probability-based classifier, especially Maximum-Likelihood.

3.3.7.2 Optimal Bandwidth – Investigation 4B

The seven optimal bands identified in Investigation 4A were found in distinct, well separated wavelength domains as evident in Figure 3.6. In fact, the wavelength interval that separates these 7 bands ranges from 45.2 to 125.4nm. Two pairs of band centers are separated by approximately 46nm: 514.9/560.1nm and 685.5/731.5nm. Only these two bands were close enough to one another to have their FWHM envelopes overlap when bandwidth was systematically increased to 8 and 12 times the original width. Thus, the first two SAM resiliency values shown in the second section of Table 3.5 represent

classifications where the increase in bandwidth resulted in no overlap, and subsequently no band elimination occurred (i.e. spectral smoothing).

The SAM-2x and SAM-6x classification results largely disproves the notion that bandwidth is a detriment to the classification of wetland imagery, as long as FWHM does not result in band overlap, and thereby band elimination. Note that both of these classifications exhibited overall-resiliency values equivalent or higher than the baseline, SAM7band classification. One could argue that bandwidth does indeed enhance classification resiliency with respect to the SAM classifier and strategically located bands, because the SAM7band and SAM-6x classifications are statistically different well above the 95 percent confidence limit.

The SAM-8x and SAM-12x results represent two 5-band classifications because bands 560.1 and 731.5nm bands were eliminated due to their FWHM overlap. Their overall-resiliency and Kappa values are surprisingly similar, although they are statistically different above a 95 percent confidence limit. The resiliency values associated with the 4-band and 7-band SAM classifications generated within Investigation-6A were 79.64% and 86.26%, respectively. As might be expected, the 5-band, Investigation 4B classifications fell between these two values. Despite their exaggerated bandwidth, these two classifications fell inline with their bandwidth-unaltered counterparts, which

further dismissed the notion that wide bands (without overlap) are a detriment to the differentiation of wetland botanical communities.

The Maximum-Likelihood classifications associated with Investigation 4B need only be briefly discussed for they exhibited the same patterns identified via the SAM results. The baseline (Max7band) and Max-2x classifications were functionally identical, while Max-6x exhibited slightly improved, but statistically different, results. The 8x and 12x, Maximum-Likelihood resiliency values were reduced as expected when two bands were eliminated. It has already been discussed that probability-based classifiers like Maximum-Likelihood are sensitive to the removal of bands.

3.3.7.3 IKONOS Spectral Simulation – Investigation 4C

The SAM4ikonos classification generated in Investigation 4A displayed an overall-resiliency was 67.74%. This classification only *spectrally* emulated the IKONOS sensor, for no band-widening was applied. The SAM_pseudo-IKONOS classification (53.01%) summarized in the third section of Table 3.5 both *spatially* and *spectrally* emulated the IKONOS sensor. A difference of 4% separated these two classifications that only differed with respect to relative bandwidth. It was demonstrated in Investigation 4A that shifting the band locations with respect to a 4-band classification can result in significant increases in resiliency (i.e. SAM4band vs. SAM4ikonos). It therefore seems

logical that the slight increase (i.e. 4%) in both the SAM and Maximum-Likelihood resiliency values associated with increased bandwidth (e.g. SAM4ikonos vs. SAM_pseudIKONOS) can be attributed to the spectral contribution of more diagnostic bands that fall within the FWHM envelope of the significantly wider IKONOS-like bands.

3.4 Summary and Conclusions

The 2nd derivative and PCA methodologies presented in this research were designed to aid in the identification of those bands that are most applicable to the differentiation of coastal wetland vegetation. This research established nine distinct wavelength domains (i.e. Table 3.4) with respect to the resampled in-situ spectra that emulated 48-band hyperspectral imagery taken of the study sites. The histograms presented in Figures 3.6 and 3.8 helped to further refine these nine domains by identifying their predominant band center (e.g. 425, 514, 560, 685, 731, 812 and 916nm). The redundancy found in the derivative and PCA methodologies should not be looked on negatively, for it functions to cross-validate the results generated via each methodology.

Under the constraints of today's technology, it is not possible to capture high spatial resolution imagery with a hyperspectral bandset. If the purpose of the imagery is to aid in the mapping of large homogeneous cover types, larger pixels can be recorded in order to allow many more bands to be recorded.

Coastal wetlands are often comprised of plant communities that are spatially complex, which dictates the use of high-resolution (i.e. 1-2 meters) imagery if the spatial integrity of these communities is deemed relevant. Unfortunately, small pixels come at the expense of spectral resolution, and only a limited number of bands would be available if small pixels were recorded.

This research established seven optimal bands (i.e. 425, 514, 560, 685, 731, 812 and 916nm) that generated classification results comparable to those generated from 48-band, hyperspectral imagery. The reduction of band number without significant classification change is important because it makes it practical to utilize small pixels without fear of sacrificing the ability to differentiate the botanical community. In addition, sensors that record a small number of bands found within the visible and NIR regions of the spectrum are relatively inexpensive to build. Certainly the “best” available spectral information is recorded by truly hyperspectral sensors, but the use of these relatively new technologies is prohibited by their high cost (approximately \$570/km²) for many potential end-users. The identification of a small number of wetland-relevant bands should significantly reduce the cost of image acquisition, which increases the number of potential “coastal” end-users considerably.

The optimal 7 bands identified in this research show interesting similarity to those identified in several recent vegetative studies, which might be expected because, at some level, all plant material have similar spectra. Thenkaboil et al. (2000) utilized detailed spectroradiometric data in order to recommend 12 bands for use in agricultural crop studies (i.e. biophysical parameters such as Leaf-Area-Index, Wet-Biomass, and Plant height). They placed maximum emphasis on three bands that represented maximum reflectance (550 and 920nm) and maximum absorption (682nm) exhibited by four agricultural crops. In contrast, Carter (1998) and Elvidge and Chen (1995) identified different key bands to be used with respect to pine vegetative indices, 674/780nm and 701/820, respectively. The similarities between these and other related studies suggest that key bands occur that potentially have widespread applicability. On the other hand, the differences (especially the pine studies) suggest that optimal band selection is landscape/target dependent since reflectance spectra differed even at the species level. These studies did not include imagery or its classification, which was the focus of this research. The derivative and PCA methodologies presented in this work show great promise with respect to identifying optimal bands for image-based wetland analyses. Much more work is needed in order to test the resiliency of these methodologies and the applicability of the methodologies put forth in this research across the overwhelming diversity of coastal wetlands.

The replacement of the optimal-7 bands with a neighboring band (except 812 vs. 823nm) caused a statistically significant reduction in classification resiliency. This suggests that movement of these key bands beyond a few nanometers in either direction would result in a less botanically robust classification. One should remember that these band locations were generated from data collected within botanically similar wetlands despite their location within different eco-regions. In addition, only late-August/early-September imagery was utilized throughout this research. It remains to be seen how static the band locations remain when these methodologies are applied across the entire growing season and/or within strikingly different wetland complexes (e.g. Chesapeake Bay).

It was demonstrated that the probability-based Maximum-Likelihood classifier is very sensitive to the removal of bands, and should therefore not be applied when constrained by a small number of bands. In contrast, SAM is largely insensitive to band removal, as long as key band centers that maintain the essence of vegetative spectral signatures are maintained. Although SAM is less sensitive to band removal, it did consistently under-perform Maximum-Likelihood as determined in Investigations 1 through 3. Somewhat surprisingly, bandwidth played a minor role with respect to overall classification resiliency. Classifications generated from width-altered imagery were equal to, or slightly better than, those generated from unaltered imagery.

This conclusion only holds true until the FWHM of adjacent bands began to overlap (i.e. 8x bandwidth).

The results of this research indicate that the IKONOS band centers are less than optimal with respect to the differentiation of coastal wetland vegetation (August/September imagery). SAM classification results using the four bands associated with the predominant occurrence peaks shown in Figure 3.6 outperformed classifications utilizing IKONOS band centers by nearly 10 percent. This spectral limitation in combination with the 4-meter spatial resolution of multispectral IKONOS imagery limits its applicability only to broad vegetative classifications where detailed spatial patterns are not the focus.

Chapter 4: A Classification-based Assessment of the Optimal Spatial Resolution of Coastal Wetland Imagery.

4.1 Introduction and Rationale

In the 1970s, state and federal agencies increasingly looked towards aerial photography for the purposes of wetland mapping and inventory (Gross et al., 1989; p. 475). Film types that are sensitive to NIR electromagnetic energy are generally preferred for wetland applications because they are more effective in detecting standing water and determining biomass, as well as differentiating wetland and upland vegetation (Hardisky et al., 1986). Aerial photography (1:1000 to 1:15,000 scales) has been found to be a fast, accurate, and relatively inexpensive method by which wetland boundaries, botanical changes, and aerial extent can be recorded (Mitsch and Gosselink, 2000; p. 107). A characteristic that limits the applicability of aerial photography to detailed vegetative mapping strategies is its non-digital format (Hardisky et al., 1986).

The launch of the Landsat-1 satellite in 1972 marked the practical beginning of spaceborne, earth resource remote sensing (Lillesand and Kiefer, 2000; p. 373). Over the ensuing thirty years, a variety of systems, with varied spatial resolutions, have been developed. Orbiting satellite-based sensors provide near-simultaneous wetland imagery over large geographic areas recorded in digital format (Gross et al., 1989; p. 476). Satellite platforms continue to provide

an overwhelming array of earth resource data when fitted with remote sensing systems, and the status of these technologies continues to change as scientific advances yield improved spacecraft and sensors (Lillesand and Kiefer, 2000; p. 373). However, regarding their utility for detailed wetland characterization, the current systems are limited by their spatial and/or spectral resolutions. These limitations become obvious in the context of a fundamental assumption of this research: the spatial heterogeneity of coastal wetlands is best captured by digital imagery with a spatial resolution at or below 5 meters. If this assumption is valid, the majority of currently available satellite imagery is not applicable to detailed wetland mapping.

The development of new-age airborne and satellite-based imaging systems is making imagery with high spatial resolution more affordable and easier to obtain. Although not widespread, the wetland literature contains recent examples of investigations that utilized hyperspectral systems to map and monitor plant communities (Borstad Associates, 1995; Brown and Borstad, 1999; Forsyth et al., 1998; Jupp et al., 1994; Ritter and Lanzer, 1997; Savastano et al., 1984; Wang et al., 2000; Zacharis et al., 1992). Common to these investigations is the exploitation of the improved spatial or spectral resolutions to more effectively differentiate wetland vegetation.

Remote sensing investigations incorporating airborne hyperspectral methodologies are ideally suited to address the spatial and spectral complexity of many wetland environments. The remote sensing community is hopeful that the improved resolving power of these new-age systems (i.e. spatial, spectral, and radiometric) will lead to significant improvements in the differentiation of wetland plant communities, thereby improving coastal mapping and monitoring efforts by improving the accuracy of image classifications. One fundamental question that remains unanswered is what spatial resolution is most appropriate for capturing the botanical complexities of Great Lakes coastal wetlands. Answering this question is an important step needed to advance the application of hyperspectral imagery in coastal environments.

The goal of the third component of this research is to generate and classify a series of spatially degraded, hyperspectral images in order to investigate the relationship between spatial resolution and botanical differentiation. This goal addresses the third research objective outlined in Chapter 1; quantitatively discern the optimal spatial framework of wetland imagery.

4.2 Methods

4.2.1 Image Spatial Degradation – Investigation 5

A spatial resolution of 5-meters has been established as a threshold at or above which detailed wetland remote sensing becomes limited at best

(ITRES, 2000). In order to evaluate classification change associated with spatial degradation (larger pixel size), the baseline Horseshoe Bay, 1-meter imagery was spatially manipulated. This imagery was incrementally resampled by increasing the functional pixel size by a factor of two, four, and eight, thereby generating imagery that effectively emulated that recorded at spatial resolutions of 2, 4 and 8 meters. These spatial resolutions were chosen for three reasons: 1) they represent a systematic degradation in spatial resolution through and beyond the established threshold; 2) they represented the incremental doubling of pixel size; and 3) the 4-meter pixel size matched the spatial resolution of the satellite-based IKONOS system. The 8-meter resampling was included to verify the inapplicability of low-resolution (i.e. > 4 meters) imagery to Great Lakes coastal environments.

The ENVI (version 3.2) Image-Resizing module was found to be inappropriate with respect to spatial (i.e. pixel size) degradation based on the algorithm it used. When an even-numbered resampling window is desired, there is no central pixel within the matrix of pixels to be mathematically combined to yield a larger, resampled pixel. In order to resample a 1-meter image into 4-meter imagery, sixteen 1-meter pixels would need to be combined in some manner to yield a single pixel that is four times larger in both the x (sample) and y (line) direction. Thus, the digital numbers (in my case percent

reflectance values) associated with a 4x4 matrix of 1-meter pixels would need to be averaged to yield a single digital number that would then be assigned to the larger output pixel. Unfortunately, when faced with an even-numbered input matrix (2x2, 4x4, etc.), ENVI assigns the mathematically unchanged value (no average calculated) found at the upper left input pixel in the window to the newly created, larger, output pixel. This methodology is fundamentally flawed because it fails to average all the reflectance values associated with the input matrix.

Supervised classifiers reference the digital number of each pixel within the image so that a classification value (training category) can be assigned. Pixels containing identical digital numbers would be assigned to the same classification category. Thus, the classification result generated from one, 4-meter pixel (e.g. DN=6.2) would be functionally and visually the same as that generated from sixteen, contiguous 1-meter pixels (all having the same value, DN = 6.2) occupying the same space. The process by which the 1-meter Horseshoe Bay imagery was transformed into synthetically coarser resolution imagery involved a series of image manipulations across three separate software packages. Only integer values are maintained when an ERDAS (*.lan) image is exported from ENVI. Subtle reflectance differences can lead to better differentiation of botanical targets and may be found within the decimal places of reflectance data. This necessitated multiplying the ENVI reflectance values

by 100. The core of the spatial resampling process summarized in Figure 4.1 was the *Blockmean* function in ArcInfo-GRID. This function partitions the input grid (1-meter pixels in my case) into blocks (2x2 4x4 and 8x8 in this study), calculates the mean value for all of the cells (pixels) in the block and writes this value to each cell in the corresponding blocks in the output grid (ESRI, 2001). Ultimately, three 1-meter, output images (synthetic-2m, synthetic-4m and synthetic-8m) were generated.

Because the original spatial resolution was preserved, the 24 ROIs that served as training data for Investigations 1 and 2 (Table 2.6) could also be used for Investigation 4. Similar to the approach taken in Chapter 3, these ROIs were used as training sites and both a SAM and Mahalanobis evaluation-standard was generated through the classification of the spatially unaltered, unrotated Horseshoe Bay imagery.

After the generation of the two evaluation-standards was completed, three identically configured SAM and Mahalanobis-Distance classifications were generated from the three spatially-altered images. Mahalanobis-Distance replaced Maximum-Likelihood in Investigation 5 because the spatial resampling methodology reduced training-class variance beyond the allowable Maximum-Likelihood threshold. No operational parameters were entered for the Mahalanobis-Distance classifications, which forced all pixels to be classified.

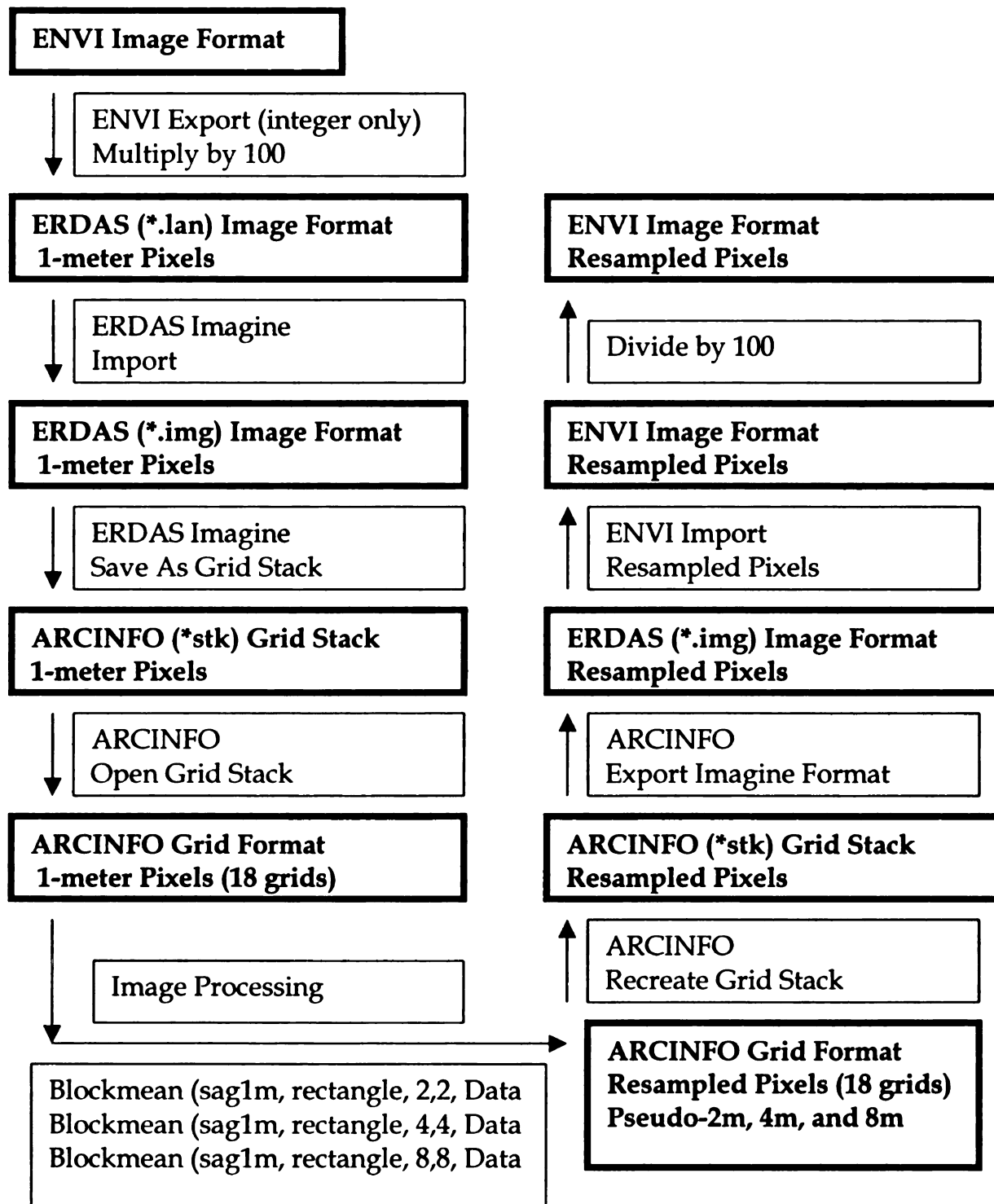


Figure 4.1 Spatial Manipulation, Image Processing Schematic

Confusion matrices were generated through the comparison of the 6 spatially-altered classification results (i.e. 2x2-SAM, 4x4-SAM, 8x8-SAM, 2x2-Mahal, 4x4-Mahal and 8x8-Mahal) with respect to their appropriate image-wide evaluation standards. Again, the assumption was made that the two evaluation-standards represent an unverified depiction of the botanical community of Horseshoe Bay. The botanical accuracy of this assumption is irrelevant with respect to the focus of this investigation because only relative change associated with spatial degradation was evaluated. The examination of the relative change with any output class reflects the classification change (i.e. class confusion) resulting from the spatial degradation. If the spatial manipulations had little affect on the classification results, the pixel counts within each class as summarized by the confusion matrix parameters would remain relatively constant. If significant changes in these values occurred, then it was presumed that the spatial resampling caused the spectral characteristics of a significant number of pixels to be classified differently or to be unclassified.

Fundamentally, as pixel size is increased within a heterogeneous region, the potential for two or more spectral classes to be included within a single pixel (mixed pixels) increases. Pixels associated with relatively large, homogeneous botanical zones (i.e. classes) would be affected the least. Inversely, botanical zones that have relatively small, areal extents would experience the greatest change (i.e. reduced producers accuracy) with respect to the evaluation

standards. At some level, the discrimination of botanical communities becomes impossible as the spectral nature of two or more spectrally distinct classes (pixels) are homogenized into a single, unclassifiable pixel. For example, linear bulrush (*Scirpus validus*) zones exist along the edges of dynamite cut, and are only a few meters in width. If the baseline pixel size is increased to eight meters, the spectral characteristics of this zone would be homogenized with neighboring cover types, rendering their identification difficult, if not impossible. The three classifications generated via both classifiers represent a systematic progression towards more spatially coarse imagery. Accordingly, the consecutive examination of their related confusion matrix parameters provided insight into the spatial resolution needed to differentiate the botanical communities in my Great Lakes wetland imagery.

4.3 Results and Discussion

4.3.1 Spectral Angle Mapper – Investigation 5

Table 4.1 contains the truncated confusion matrix parameters generated for the three SAM classification runs associated with Investigation 5. Each subsequent column represents classification change resulting from the systematic doubling of spatial resolution. The overall-resiliency and related Kappa values indicate a systematic increase in classification change (i.e. decrease in resiliency) resulting from the increase in functional pixel size. The

		<u>2x2-SAM</u>	<u>4x4-SAM</u>	<u>8x8-SAM</u>
Overall Resiliency:		77.09%	65.11%	50.31%
Kappa Coefficient:		0.7536	0.6251	0.4696
		Producers Resiliency (Percent)	Producers Resiliency (Percent)	Producers Resiliency (Percent)
<u>Image Class</u>				
0	Unclassified	11.62	0.86	0.1
1	chara	85.41	67.04	34.23
2	phragmites-clump	57.31	52.06	58.93
3	scival-dense	30.86	15.09	12.78
4	scival-clump	63.75	48.47	24.69
5	typha-soil2	84.09	76.43	69.51
6	sagrigida60/40	72.97	63.55	57.18
7	beachsand	82.7	73.12	61.76
8	shallowh20	64.52	51.81	42.08
9	hetdub	79.04	67.04	61.84
10	sagrigida	59.61	46.2	30.53
11	vallisneria	94.51	87.07	80.55
12	deeph20	93.98	88.85	87.45
13	scivalbrown	73.51	58.94	63.99
14	leersia	66.1	50.97	26.54
15	Muck	46.36	13.9	5.64
16	saggram/chara	87.71	81.84	71.08
17	typhah20	54.92	23.13	4.45
18	nuphar	56.85	34.09	26.18
19	eleocharis	51.17	36.8	29.83
20	impatians	68.18	48.46	32.05
21	bluejoint	56.72	43.84	29.49
22	cutgrass-eleocharis	78.19	64.48	37.01
23	eleocharis-sand	81.22	69.65	16.16
24	typha-phrag-scival	73.25	67.32	62.2

Table 4.1. Summary Table, SAM Spatial Degradations

Kappa and overall-resiliency values are very similar, indicating that chance agreement played little role.

The degradation to a 2-meter, functional pixel size caused approximately 23% of all pixels to be classified into a different class compared to the 1-meter evaluation standard. Spatial degradation to a 4-meter equivalent further reduced overall-resiliency to approximately 65%, indicating that 35% of all pixels were classified into a different class. Based on the assumption that the evaluation standard represents a snapshot of the botanical community, the vast majority of these errors would represent classification errors. Nearly half of all the pixels were classified differently as a result of increasing the functional pixel size to 8 meters. As expected, overall classification outcome is extremely sensitive to pixel size. The 2-meter results represent a change of 23%, which could be considered acceptable depending on the nature of the community being classified. However, few would argue that a 50% change would not hinder the detailed mapping of coastal wetlands.

A better appreciation for the role of pixel size with respect to wetland image classification is gained through the examination of the class-specific producers-resiliency values shown in Table 4.1. The producers-resiliency values found in the first column (i.e. 2x2-SAM) represent the percentage of class-specific pixels that remained consistent with the 1-meter, evaluation

standard. For example, only 6.02% of the evaluation-standard, deep-water pixels (i.e. class 12; deeph20) were classified differently (resiliency = 93.98%) when the functional pixel size was degraded to 2 meters.

Classes 11 and 12 represent cover types that were the least affected by spatial degradation. These classes (*Vallisneria americana* and deep-water, respectively) represent large homogeneous regions. In the interior of such a region, pixel size can be increased dramatically without fear of encountering a spectrally different cover type, and only its edges have any potential for spectral confusion. Due to the spectrally suppressive nature of water, it would take a considerable amount of a spectrally different cover type (e.g. emergent vegetation) to alter a classification result. Class 1 (*Chara sp.*) is also a spatially extensive class, but it was less resilient than classes 11 and 12. The *Chara* evaluation-standard pixels were largely found within the eastern half of Horseshoe Bay proper. Unlike the deep-water and *Vallisneria* classes, this region is significantly interspersed with pockets of deeper water, clumps of emergent vegetation, and floating leaf plants. Accordingly, the potential for spectral overlap as pixel size increases is much higher for this class. In the 2-meter results, only about 15% change occurred, which is among the best-performing classes. However, when pixel size was increased to 8 meters and the various cover types mentioned above are encompassed with one pixel, about 65% of the *Chara* pixels were classified differently.

The very low resiliency value associated with class 7 (beach sand) might at first seem surprising, considering that this class has been previously described as being a spectrally distinct, easily-classified cover type. So why did this class not exhibit resiliency as pixel size increased? The answer lies in its relative position within the landscape. The majority of the beach sand pixels in the evaluation standard are associated with narrow, linear sand deposits along the southern shoreline of Middle Grounds Island. This ribbon of sand is approximately 25 meters in width, and is interspersed with regions of vegetation and deadfall. At the 2-meter pixel size, this class displays a relatively minor change (82.7% resiliency), but its percentage of misclassification steadily increases with pixel size. The linear nature of the beach sand zone gives it a relatively low area-to-perimeter ratio. As pixel size increases, the edge pixels overlap considerably with the surrounding cover types, resulting in classification change.

4.3.2 Mahalanobis Classifications - Investigation 5

Table 4.2 contains the truncated confusion matrix parameters generated for the three Mahalanobis classification runs associated with Investigation 5.

Again, each subsequent column represents classification change resulting from the systematic doubling of spatial resolution. The overall-resiliency and related Kappa values show a systematic increase in classification change resulting from the increase in functional pixel size. Kappa and overall-resiliency values are

		<u>2x2-Mahal</u>	<u>4x4-Mahal</u>	<u>8x8-Mahal</u>
Overall Resiliency:		69.92%	42.51%	0.40%
Kappa Coefficient:		0.6771	0.3847	-0.0571
		Producers Resiliency (Percent)	Producers Resiliency (Percent)	Producers Resiliency (Percent)
<u>Image Class</u>				
0	Unclassified	0	0	0
1	chara	50.56	43.68	0
2	phragmites-clump	56.52	48.22	0
3	scival-dense	73.24	52.41	0
4	scival-clump	72.6	29.85	0
5	typha-soil2	58.26	13.47	4.66
6	sagrigida60/40	20.76	14.8	0
7	beachsand	95.76	55.81	0
8	shallowh20	76.46	37.75	0
9	hetdub	77.2	54.5	0
10	sagrigida	72.08	16.97	0
11	vallisneria	85.93	47.3	0
12	deeph20	96.6	86.84	0
13	scivalbrown	84.43	76.98	1.83
14	leersia	68.66	29.13	0
15	muck	35.66	6.15	0
16	saggram/chara	79.83	30.86	0
17	typhah20	64.1	30.9	0
18	nuphar	55.51	20.8	0
19	eleocharis	40.77	9.01	1.73
20	impatians	36.93	23.98	1.87
21	bluejoint	64.64	40.82	0
22	cutgrass-eleocharis	49.86	18.81	0
23	eleocharis-sand	63.2	35.8	0.01
24	typha-phrag-scival	77.41	68.85	0

Table 4.2. Summary Table, Mahalanobis-Distance Spatial Degradation.

very similar, indicating that chance agreement played little role. The degradation to a 2-meter, functional pixel size caused approximately 30% of all pixels to be classified differently compared to the 1-meter evaluation standard. At the 4-meter pixel size, nearly 58% of the pixels were classified differently. Assuming that the evaluation standard represents an accurate depiction of the botanical community, the majority of these pixels would represent classification errors. Virtually all of the pixels were classified differently as a result of increasing the functional pixel size to 8 meters. In fact, the negative Kappa Coefficient for the 8-meter classification indicates that it is less “accurate” than one generated randomly.

The overall classification outcome of the Mahalanobis classifier is extremely sensitive to spatial resolution changes, more so than the SAM classifier. The probability distribution centered on each training class mean was expanded as the spectral overlap of all image pixels were homogenized within the spatial degradation process. The homogenization of image reflectance values increases the spectral similarity of all classes, and only the most distinct or heterogeneous classes displayed any resiliency. This spectral smoothing process had a lesser effect on the physically-based (i.e. non-probability-based) SAM classifier discussed in the previous section. Because of the extremely poor results associated with the 8-meter classification, it seems likely that the amount of training class variance reached a level that rendered the classifier unusable.

A better appreciation for the role of pixel size with respect to the Mahalanobis-Distance classification is gained through the examination of the class-specific, producers-resiliency values shown in Table 4.2. The producers-resiliencies found in the first column (i.e. 2x2-Mahal) represent the percentage of class-specific pixels that remained consistent with the 1-meter, evaluation standard. For example, only 3.40% of the evaluation-standard, deep-water pixels (class 12; deeph20) were classified differently (resiliency = 96.6%) when the functional pixel size was degraded to 2 meters.

Just as in the analogous SAM examples provided earlier, classes 7, 11 and 12 represent the cover types least affected by spatial degradation. Classes 11 and 12 (*Vallisneria americana* and deep-water, respectively) represent large homogeneous regions, and pixel size can be increased dramatically without fear of encountering a spectrally different cover type. Due to the spectrally suppressive nature of water, it would take a considerable amount of a spectrally different cover type (e.g. emergent vegetation) to alter a classification result.

The best performing class with respect to the 2-meter Mahalanobis-Distance classification was class 7 (beach sand). Probability-based classifiers perform well on spectrally distinct classes (i.e. magnitude separation) like class 7, until the homogenization of reflectance overcomes the probability threshold. This is

evident by the significant resiliency falloff in class 7 between the 2- and 4-meter classifications. Class 24, an inherently mixed class, remained relatively unaffected by a decrease in spatial resolution from 2 to 4 meters.

Homogenization of this class through spatial degradation should have a relatively minor affect because it is “naturally” homogenized (i.e. mixed). The class-specific results associated with the 8-meter classification only serve as an indication that the variance threshold of this classifier was exceeded, and little botanically relevant information can be extracted.

It was previously established (ITRES, 2000) that a spatial resolution of 5 meters or less is appropriate for wetland mapping strategies. Interestingly, this research indicates that even 2-meter pixels failed to adequately capture (23% and 30% change) the spatial mosaic of plant species found in Horseshoe Bay. Less heterogeneous wetland plant communities could probably be classified adequately with 4-meter imagery, but pixel sizes above this level would not be recommended.

As described in the previous section, the falloff in classification resiliency is inherently tied to the spatial configuration of the plant community. Classification of an image taken of a 500 acre *Phragmites* marsh would be largely independent of pixel size (i.e. 1-10 meters) because of the lack of spatial heterogeneity. As the spatial complexity of the target increases, the spatial

resolution required to map it must also increase. Examination of Figure E-6 in Appendix E illustrates the inverse relationship between spatial heterogeneity and pixel size. A 50x50 pixel portion of the 1-meter, Horseshoe Bay SAM classification is shown along with its analogous 2x2, 4x4, and 8x8 spatially-altered counterparts. This series of images illustrates the systematic elimination of classes and the reduction of class interspersion. The light blue class best illustrates class elimination because it was completely absent in the 4- and 8-meter images despite being prevalent in the 1-meter baseline classification. The yellow class best illustrates the loss in class interspersion, because its rather complex spatial mosaic found in the baseline classification has been reduced to non-descript blocks in the coarser imagery. Obviously, the total acreage of this class has been inflated by the spatial degradation and the small-patch nature of this class has been totally lost.

4.4 Summary and Conclusions

Care was taken to ensure that the study sites used throughout this research reflect the potential botanical complexity (both spatial and spectral) of Great Lake coastal wetlands. Investigation 5 has demonstrated that high spatial resolution imagery (i.e. 1-2 meters) is paramount to accurately map and monitor these critical environments.

Chapter 5: CONCLUSIONS AND FUTURE RESEARCH

The entirety of this research focused on evaluating the applicability of high spatial and spectral resolution imagery with respect to the mapping and monitoring of Great Lakes Coastal wetlands. This focus was explored through a series of investigations that addressed three underlying themes: 1) classifier performance and transferability (Investigations 1-3), 2) optimal spectral resolution (Investigation 4), and 3) optimal spatial resolution (Investigation 5).

5.1 Classifier Performance and Transferability

It was established in previous chapters that coastal wetlands can be botanically complex, exhibiting a rich mosaic of plant species/assemblages that are distributed along the predominant hydrologic gradient. It is this characteristic that typically makes wetlands a challenging remote sensing target due to the relative spectral similarity of the predominantly vegetated landscape. Botanical training sites (Regions-of-Interest) were delineated that represented the predominant cover types found in each study site during the 2000 and 2001 field campaigns. These ultimately served as the basis for multiple classification comparisons.

The probability-based Maximum-Likelihood classifier was the best performing classifier with respect to the differentiation of the field-delineated ROIs. Approximately 87% of the accuracy assessment pixels (easterly ROIs) were correctly classified by Maximum-Likelihood, which was nearly ten percent higher than the comparable SAM classification. It was shown that probability-based classifiers are magnitude-dependent (y-axis separation), and their associated errors are typically derived from within-class misclassifications. Maximum-Likelihood displayed the greatest potential for differentiating the complex botanical communities found in the Lake Huron wetlands analyzed in this study. From a practical standpoint, the Maximum-Likelihood classifier would be ideal for delineating major botanical classes when some degree of within-class error (e.g. confusion of similarly structured emergent species) can be tolerated.

The baseline SAM classifier under-performed the Maximum-Likelihood classifier by nearly ten percent, but showed promise. This physically-based classification tool tended to confuse classes that displayed similar greenness (i.e. shape of the reflectance signature), and differed from Maximum-Likelihood in that it is insensitive to magnitude differences. Both the Les Cheneaux and Horseshoe Bay imagery was taken as the botanical community neared the end of its growing season, which likely contributed to the success of the SAM classifier because the plant community was in various stages of dieback.

Imagery taken when the community was at “peak green” would likely lead to an increase in greenness confusion by the SAM classifier.

The strengths of both classification tools could be used in combination to enhance classification accuracies. Maximum-Likelihood should be used to parse an image into the predominant classes. Then, complex classes could be isolated via image masking in order to capitalize on the ability of the SAM classifier to differentiate similar spectra based on relatively subtle spectral features that are lost in the magnitude-based approach. This is certainly an area that needs to be explored further within the context of coastal wetlands.

From a practical standpoint, this research indicates that PCA rotation should routinely be utilized in combination with probability- based classification tools. Fundamentally, PCA rotation concentrates target variance into a small number of independent channels. The resulting dimensionally-reduced signatures are better differentiated by magnitude-sensitive classifiers because the image spectra are more equitably distributed (i.e. more class separation).

The Prentiss Bay imagery was incorporated into this research in order to test the transferability of “methods” developed with respect to the Horseshoe Bay, 1-meter imagery. Generally, the outcome of like-configured Prentiss and

Horseshoe Bay classifications were very similar, and trends were common throughout. PC-rotated Maximum-Likelihood and un-rotated SAM methodologies as outlined in this research were not site dependent, and could likely provide the basis for basin-wide wetland mapping, especially in combination.

Although not completely understood, it seems likely that some type of systematic radiometric noise was inherent to the AISA imagery, as evident by the poor SAM and Maximum-Likelihood classification results generated from the raw AISA imagery. PC-rotation is known to sequester such systematic noise into lower-order dimensions, and this was indeed the case in this research as evident by the sharp increase in the accuracy of the Maximum-Likelihood classification (41 percentage points) after PC-rotation of the AISA imagery. Results generated from a probability-based classifier in conjunction with both raw and rotated imagery could function as a viable test for subtle, system-level noise.

5.2 Optimal Spectral Resolution

Under the constraints of today's technology, it is not possible to capture high spatial resolution imagery with a hyperspectral bandset. If the purpose of the imagery is to aid in the mapping of large homogeneous cover types, larger pixels can be recorded in order to allow many more bands to be recorded.

Coastal wetlands are often comprised of plant communities that are spatially complex, which dictates the use of high-resolution (i.e. 1-2 meters) imagery if the spatial integrity of these communities is deemed relevant. Unfortunately, small pixels come at the expense of spectral resolution, and only a limited number of bands would be available.

The 2nd derivative and PCA methodologies presented in Chapter 3 were designed to identify those bands that are most applicable to the differentiation of coastal wetland vegetation. This research established seven optimal bands (i.e. 425, 514, 560, 685, 731, 812 and 916nm) that generated SAM classification results comparable to those generated from 48-band, hyperspectral imagery. The reduction of band number without significant classification change is important because it makes it practical to utilize small pixels without fear of sacrificing the ability to differentiate the botanical community. In addition, sensors that record a small number of bands found within the visible and NIR regions of the spectrum are relatively inexpensive to build. Certainly the “best” available spectral information is recorded by truly hyperspectral sensors, but the use of these relatively new technologies is prohibited by their high cost (approximately \$750/km²) for many potential end-users. The identification of a small number of wetland-relevant bands should significantly reduce the cost of image acquisition, which increases the number of potential “coastal” end-users considerably. Much more work is needed in order to test the applicability of the

derivative and PCA methodologies put forth in this research across the overwhelming diversity of coastal wetlands. However, consistency across two eco-reaches of the upper Great Lakes has been demonstrated.

The in-situ- and PC-based derivative methodologies, along with the visual inspection of the PC-loading curves, formed the foundation for the selection of the optimal 7 bands. The predominant wavelength domains were identified via all three approaches indicating that some of these efforts were redundant. However, a variety of less-significant wavelength domains were identified via each method. The bulk of the effort associated with these methodologies involved the preparation of the in-situ signatures and the creation of the derivative spreadsheet templates. Once these preliminary tasks are completed, a variety of methodologies can be easily applied (e.g. covariance-PCA, correlation-PCA, in-situ derivatives and loading derivatives), so it is best to utilize them all in case one identifies a key spectral band missed by the others. The associated redundancy should not be looked on negatively because it cross-validates the results generated via each methodology.

Despite the similarity of the I-4 overall-resiliency values, the replacement of the optimal-7 bands with a neighboring band (except 812 vs. 823nm) caused a statistically significant reduction in classification resiliency. This suggests that movement of these key bands beyond a few nanometers in either direction

would result in a less botanically robust classification. One should remember that these band locations were generated from data collected within botanically similar wetlands despite their location within different eco-regions. In addition, only late-August/early-September imagery was utilized throughout this research. It remains to be seen how static the band locations remain when these methodologies are applied across the entire growing season and/or within strikingly different wetland complexes (e.g. Chesapeake Bay).

It was demonstrated that the probability-based Maximum-Likelihood classifier is very sensitive to the removal of bands, and should therefore not be applied when constrained by a small number of bands. In contrast, SAM is largely insensitive to band removal, as long as key band centers that maintain the essence of vegetative spectral signatures are maintained. Although SAM is less sensitive to band removal, it did consistently under-perform Maximum-Likelihood when using many bands.

Surprisingly, bandwidth played a minor role with respect to overall classification resiliency. Classifications generated from bandwidth-altered imagery were equal to, or slightly better than, those generated from unaltered imagery. This conclusion only holds true until the FWHM of adjacent bands began to overlap and bands were eliminated (i.e. 8x bandwidth).

The results of this research indicate that the IKONOS band centers are less than optimal with respect to the differentiation of coastal wetland vegetation (August/September imagery). SAM classification results using the bands associated with the 4 predominant occurrence peaks out-performed classifications utilizing IKONOS band centers by nearly 10 percent. This limitation, in combination with the 4-meter spatial resolution of multispectral IKONOS imagery, limits its applicability to broad vegetative classifications where detailed spatial patterns are not the focus.

5.3 Optimal Spatial Resolution

This research established the optimal spatial resolution of coastal wetland imagery to be at or below 2 meters. The spatial complexities of the studied coastal wetlands merit the use of such imagery when an accurate depiction of the botanical community is desired. When more broadly defined vegetative classes are appropriate, 4-meter imagery can perform adequately. Next-generation satellite imaging systems are being deployed that will provide multispectral imagery with improved spatial resolutions (e.g. QuickBird, 2.44-meter pixels; www.digitalglobe.com). The four, broad bands offered by QuickBird are functionally identical to those of the IKONOS sensor, which were shown to be less than optimal for coastal wetland studies. Despite its spectral limitations, classification accuracies generated with QuickBird imagery would likely increase due to the significant reduction in pixel size. At the time of this

writing, only programmable, airborne imaging systems encompass the spatial and spectral characteristics needed to map and/or monitor Great Lake coastal wetlands with high classification accuracy.

5.4 Limitations of the Technology

The high accuracy levels at which the methodologies presented in this research delineated the botanical ROIs was a very positive outcome. The objectives of this research focused only on the ability to differentiate the predominant botanical communities found at both study sites, and represented the first step in the evaluation of hyperspectral technologies in Great Lakes coastal wetlands. The improved spatial and spectral resolution of hyperspectral imaging systems show great potential for improving wetland mapping and monitoring in light of the results of this research.

The accurate differentiation of select cover types does not directly equate to improved mapping and monitoring, and hyperspectral approaches are not without limitations. An image-wide, PC-rotated, Maximum-likelihood classification of the 1-meter Horseshoe Bay CASI-II imagery is presented in Figure 5.1 in order to illustrate three limitations: 1) class confusion, 2) unrepresented classes and 3) radiometric path differences.

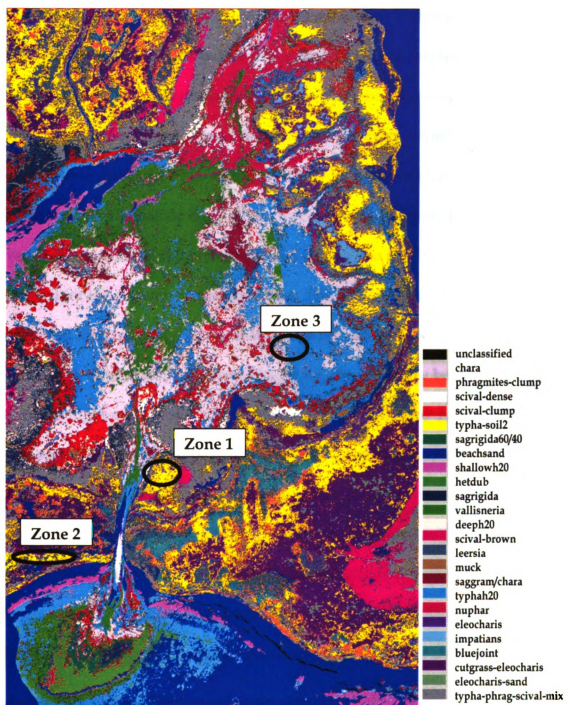


Figure 5.1. Horseshoe Bay; PC654321 Max.-Likelihood Classification.

Zone 1 (Figure 5.1) highlights instances where the cattail training class cross-classified with regions that contained dense stands of other tall-stature emergents and graminoids in Horseshoe Bay. The hyperspectral techniques applied throughout this research were not robust enough to separate this spectrally similar training class from others on an image-wide basis. Zone 2 (also a misclassification) highlights a linear willow thicket (*Salix sp.*) near dynamite cut (Horseshoe Bay). This cover class was not visited during field verification efforts, and therefore was not included in the 24 training classes utilized for the supervised classifications. The lack of a training class to represent this cover type means that it must remain unclassified or be completely cross-classified. Zone 3 highlights the boundary between two adjacent flight paths that were combined into one image mosaic by ITRES, Inc. The predominant cover type in this shallowly inundated portion of Horseshoe Bay was *Chara sp.* Radiometric differences between these two image paths caused the *Chara* class (left path) to be systematically misclassified in one swath (right) while being correctly classified in the swath containing the region-of-interest (left). The botanical community in this zone was homogeneous across both images, indicating that the differences are an artifact of the imagery itself.

The methodologies presented in this research represent the first step in exploring the role hyperspectral technologies can contribute to coastal Great Lakes wetland mapping and monitoring. If the results of this work had

indicated that few detailed botanical classes could be differentiated, there would be little hope for hyperspectral technologies to advance coastal mapping and monitoring. My results indicate there is indeed hope, although limitations exist that are dictated by the nature of current hyperspectral technologies (e.g. band number), the spectral complexities of wetland plant communities (e.g. BRDF, similar greenness), and the methodologies outlined in this research.

5.5 Recommendations for Future Research

Because this research is the “first step”, the potential for future research is great. Improved sensor technologies will result in better spatial, spectral and radiometric resolution. Methodologies similar to those outlined in this research should be applied to this “newer” imagery to test if indeed such advancements will help better define coastal wetland plant communities. A more rigorous radiometric calibration approach (i.e. atmospheric correction models) should be applied to my current imagery data and analogous classifications should be generated in order to evaluate any classification differences. Additional in-situ spectra should be collected that capture the spectral essence of wetland plant communities throughout the growing season and under varied environmental conditions. A more complete spectral library of Great Lakes wetland plant communities will hopefully lead to better differentiation and improve mapping and monitoring strategies. In addition, a larger spectral data set could potentially reveal key spectral domains that were missed in this research that

would improve differentiation. A more complete field-verification campaign should be implemented that would provide a wetland-wide ground-truth standard. This would allow a more formal accuracy assessment strategy to be implemented (i.e. randomly generated, image wide), providing the framework for a statistically defensible mapping of one or more Great Lakes coastal wetlands. This would also eliminate cover types that were not represented within the training data used to generate classification results. Ideally, these mapping efforts would encompass a variety of wetlands, further testing the applicability of these technologies across the Great Lakes region.

Appendix A

Horseshoe Bay 1-meter PCA Image
ENVI's Statistics Output - 6 Dimensions

<u>Band</u>	<u>Min</u>	<u>Max</u>	<u>Mean</u>	<u>Stdev</u>	<u>Eigenvalues</u>	<u>Percent Var.</u> <u>Explained</u>	<u>Cumm.</u> <u>Variance</u>
1	-0.693	34.096	2.625	1.182	711.311	94.357	94.357
2	0	41.779	4.448	1.838	34.892	4.628	98.986
3	0	42.297	4.492	1.867	5.690	0.755	99.741
4	0	42.859	4.318	1.855	0.829	0.110	99.851
5	0	43.443	4.172	1.860	0.678	0.090	99.941
6	0	44.260	3.935	1.880	0.162	0.022	99.962
7	0	45.287	3.993	1.934	0.119	0.016	99.978
8	0	44.650	3.808	1.936	0.100	0.013	99.991
9	0	44.473	3.442	1.921	0.025	0.003	99.994
10	0	45.160	3.414	1.924	0.019	0.002	99.997
11	0	47.039	4.091	2.069	0.010	0.001	99.998
12	0	49.493	7.657	3.484	0.004	0.001	99.999
13	0	49.816	9.851	5.569	0.003	0.000	99.999
14	-0.423	54.896	13.549	10.016	0.002	0.000	99.999
15	0	56.787	14.747	10.481	0.002	0.000	100.000
16	0	57.009	15.010	10.741	0.001	0.000	100.000
17	-0.892	57.471	15.405	12.778	0.001	0.000	100.000
18	-1.082	60.458	15.594	13.565	0.001	0.000	100.000
Total =					753.848514	100	

Prentiss Bay 1-meter PCA Image
ENVI's Statistics Output - 6 Dimensions

<u>Band</u>	<u>Min</u>	<u>Max</u>	<u>Mean</u>	<u>Stdev</u>	<u>Eigenvalues</u>	<u>Percent Var.</u> <u>Explained</u>	<u>Cumm.</u> <u>Variance</u>
1	-1.191	100	0.831	2.020	383.581	92.150	92.150
2	0	100	1.104	2.578	31.387	7.540	99.690
3	0	100	1.137	2.662	0.677	0.163	99.853
4	0	100	1.131	2.722	0.203	0.049	99.902
5	-0.5	100	1.071	2.700	0.143	0.034	99.936
6	0	100	1.067	2.727	0.058	0.014	99.950
7	-0.127	100	1.048	2.736	0.037	0.009	99.959
8	0	100	1.015	2.694	0.032	0.008	99.967
9	0	100	0.967	2.620	0.027	0.006	99.973
10	-0.138	100	0.978	2.645	0.019	0.004	99.978
11	0	100	1.140	2.942	0.016	0.004	99.982
12	0	100	1.405	3.453	0.012	0.003	99.984
13	0	100	1.655	4.054	0.011	0.003	99.987
14	-1.076	100	2.149	5.588	0.009	0.002	99.989
15	-0.555	100	2.317	6.143	0.008	0.002	99.991
16	-0.643	100	2.424	6.461	0.008	0.002	99.993
17	-3.313	100	2.517	6.706	0.008	0.002	99.995
18	-1.929	100	2.683	7.117	0.008	0.002	99.997
19	-1.453	100	2.705	7.154	0.007	0.002	99.999
20	-2.014	100	2.749	7.292	0.006	0.001	100.000

Total = 416.256391 100

Horseshoe Bay 4-meter PCA Image
ENVI's Statistics Output - 6 Dimensions

<u>Band</u>	<u>Min</u>	<u>Max</u>	<u>Mean</u>	<u>Stddev</u>	<u>Eigenvalues</u>	<u>Percent Var.</u> <u>Explained</u>	<u>Cumm.</u> <u>Variance</u>
1	0	0.166	0.051	0.005	0.174	97.238	97.238
2	0	0.186	0.048	0.005	0.003	1.593	98.831
3	0	0.208	0.047	0.006	0.002	1.009	99.840
4	0	0.234	0.044	0.006	0.000	0.062	99.901
5	0	0.248	0.044	0.007	0.000	0.031	99.932
6	0	0.250	0.044	0.007	0.000	0.019	99.951
7	0	0.250	0.043	0.008	0.000	0.012	99.964
8	0	0.248	0.043	0.008	0.000	0.010	99.974
9	0	0.246	0.044	0.008	0.000	0.008	99.982
10	0	0.249	0.047	0.009	0.000	0.006	99.988
11	0	0.252	0.052	0.011	0.000	0.002	99.990
12	0	0.257	0.056	0.012	0.000	0.002	99.992
13	0	0.265	0.058	0.013	0.000	0.001	99.993
14	0	0.272	0.057	0.013	0.000	0.001	99.994
15	0	0.277	0.055	0.012	0.000	0.001	99.995
16	0	0.282	0.053	0.012	0.000	0.001	99.996
17	0	0.287	0.052	0.013	0.000	0.001	99.996
18	0	0.288	0.050	0.013	0.000	0.001	99.997
19	0	0.295	0.049	0.013	0.000	0.001	99.997
20	0	0.305	0.050	0.014	0.000	0.001	99.998
21	0	0.300	0.048	0.014	0.000	0.001	99.998
22	0	0.312	0.046	0.015	0.000	0.001	99.999
23	0	0.298	0.044	0.015	0.000	0.001	99.999
24	0	0.307	0.043	0.015	0.000	0.001	100.000
25	0	0.325	0.048	0.016	0.000	0.000	100.000
26	0	0.340	0.066	0.018	0.000	0.000	100.000
27	0	0.330	0.089	0.025	0.000	0.000	100.000
28	0	0.341	0.114	0.040	0.000	0.000	100.000
29	0	0.335	0.136	0.059	0.000	0.000	100.000
30	0	0.350	0.150	0.070	0.000	0.000	100.000
31	0	0.359	0.153	0.073	0.000	0.000	100.000
32	0	0.384	0.168	0.080	0.000	0.000	100.000
33	0	0.378	0.166	0.079	0.000	0.000	100.000
34	0	0.385	0.171	0.080	0.000	0.000	100.000
35	0	0.388	0.175	0.080	0.000	0.000	100.000
36	0	0.390	0.177	0.081	0.000	0.000	100.000
37	0	0.398	0.181	0.087	0.000	0.000	100.000
38	0	0.403	0.184	0.092	0.000	0.000	100.000
39	0	0.402	0.184	0.094	0.000	0.000	100.000
40	0	0.404	0.187	0.096	0.000	0.000	100.000
41	0	0.410	0.191	0.100	0.000	0.000	100.000
42	0	0.412	0.193	0.102	0.000	0.000	100.000
43	0	0.414	0.192	0.102	0.000	0.000	100.000

44	0	0.419	0.198	0.106	0.000	0.000	100.000
45	0	0.430	0.206	0.112	0.000	0.000	100.000
46	0	0.416	0.192	0.103	0.000	0.000	100.000
47	0	0.459	0.230	0.119	0.000	0.000	100.000
48	0	0.439	0.228	0.118	0.000	0.000	100.000
Total =				0.17854	100	100	

Mismer Bay 1-meter PCA Image
ENVI's Statistics Output - 6 Dimensions

<u>Band</u>	<u>Min</u>	<u>Max</u>	<u>Mean</u>	<u>Stdev</u>	<u>Eigenvalues</u>	<u>Percent Var. Explained</u>	<u>Cumm. Variance</u>
1	-0.377	100	0.707	1.766	332.074	92.792	92.792
2	0	100	0.921	2.259	23.749	6.636	99.428
3	0	100	0.945	2.325	1.499	0.419	99.847
4	0	100	0.919	2.308	0.219	0.061	99.908
5	-0.074	100	0.792	2.072	0.111	0.031	99.939
6	0	100	0.773	2.061	0.044	0.012	99.951
7	-0.196	100	0.744	2.025	0.030	0.008	99.960
8	-0.109	100	0.705	1.972	0.028	0.008	99.968
9	-0.034	100	0.660	1.895	0.022	0.006	99.974
10	-0.609	100	0.664	1.913	0.016	0.005	99.978
11	-0.422	100	0.779	2.174	0.013	0.004	99.982
12	0	100	0.977	2.688	0.010	0.003	99.985
13	-0.192	100	1.184	3.349	0.009	0.003	99.987
14	-0.884	100	1.677	5.102	0.007	0.002	99.989
15	-0.712	100	1.892	5.868	0.007	0.002	99.991
16	-0.753	100	2.020	6.308	0.007	0.002	99.993
17	-1.662	100	2.117	6.577	0.006	0.002	99.995
18	-1.574	100	2.244	6.978	0.006	0.002	99.997
19	-1.759	100	2.263	7.022	0.006	0.002	99.998
20	-3.279	100	2.292	7.103	0.005	0.001	100.000
Total =				357.868	100		

Mismer Bay 4-Meter IKONOS PCA Image
ENVI's Statistics Output - 4 Dimensions

<u>Band</u>	<u>Min</u>	<u>Max</u>	<u>Mean</u>	<u>Stdev</u>	<u>Eigenvalues</u>	<u>Percent Var. Explained</u>	<u>Cumm. Variance</u>
1	276	446	312.795	24.319	16756.310	84.636	84.636
2	242	1631	306.722	39.860	2892.030	14.608	99.244
3	135	1244	198.442	39.426	130.980	0.662	99.905
4	116	1357	300.744	126.742	18.770	0.095	100.000
Total					19798.09	100.000	

Appendix B

Confusion Matrix:

Original
ISODATA

Class Code	Class Code	1	2	3	4	5	6	7	8	9	10	11	12	13	14	15	16	17
1	6	29	0	0	0	0	0	0	0	0	0	0	0	0	0	0	0	0
1	9	0	0	0	0	0	0	0	0	0	0	0	0	0	0	0	0	0
3	23	0	0	24	0	0	3	0	0	0	1	0	0	0	0	0	0	0
3	27	0	0	12	0	0	0	0	0	0	4	0	0	0	0	0	0	0
3	28	0	0	18	0	0	0	0	0	0	8	0	0	0	0	0	0	0
4	15	0	0	0	41	0	4	0	0	0	0	0	0	0	0	0	0	0
5	46	0	12	0	0	18	0	0	0	0	0	0	0	0	0	0	0	0
6	20	0	0	0	0	0	8	0	0	0	0	0	0	0	0	0	0	0
6	22	0	0	0	0	0	5	0	0	0	0	0	0	0	0	0	0	0
7	8	0	0	0	0	0	0	2	0	0	0	0	0	0	0	0	0	0
7	17	0	0	0	0	0	0	15	0	0	0	0	0	0	0	0	0	0
7	32	0	0	0	0	0	0	5	0	0	0	0	0	0	0	0	0	0
7	34	0	0	0	0	0	0	1	0	0	0	0	0	0	0	0	0	0
8	5	0	0	0	0	0	0	0	23	0	0	0	0	0	0	0	0	0
8	11	0	0	0	0	0	0	0	17	0	0	0	0	0	0	0	0	0
9	3	0	0	0	0	0	0	0	0	2	0	0	0	0	0	0	0	0
9	10	0	0	0	0	0	0	0	0	24	0	0	0	0	0	0	0	0
10	29	0	0	0	0	0	0	0	0	0	3	0	0	0	0	0	0	0
10	30	0	0	0	0	0	0	0	0	0	8	0	0	0	1	0	0	0
10	37	0	0	0	0	0	0	0	0	0	5	0	0	0	1	0	0	0
10	38	0	0	0	0	0	0	0	0	0	2	0	0	0	1	0	0	0
12	2	0	0	0	0	0	0	0	0	0	0	36	47	0	0	0	0	0
13	25	0	0	0	0	0	0	0	0	0	0	0	0	14	0	0	0	0
13	26	0	0	0	0	0	0	0	0	0	0	0	0	8	0	0	0	0
14	45	0	5	0	0	0	0	0	0	0	1	0	0	0	6	0	0	0
16	4	17	0	0	0	0	0	0	0	0	0	0	0	0	0	0	30	0

sag1m_ISODATA_48classes.cls
Horseshoe Bay - 1-meter imagery

Ground Truth Class Code

Overall Accuracy: 62.72%
Kappa Coefficient: .6023

Row		Producers Accuracy (Percent)		Consumers Accuracy (Percent)		Omission Errors (Percent)		Commission Errors (Percent)	
Total		Image Class		Unclassified					
18	0	24	0	23	0	22	0	21	0
19	0	20	0	19	0	18	0	17	0
20	0	0	0	0	0	0	0	0	0
21	0	0	0	0	0	0	0	0	0
22	0	0	0	0	0	0	0	0	0
23	0	0	0	0	0	0	0	0	0
24	0	0	0	0	0	0	0	0	0
25	0	0	0	0	0	0	0	0	0
26	0	0	0	0	0	0	0	0	0
27	0	0	0	0	0	0	0	0	0
28	0	0	0	0	0	0	0	0	0
29	0	0	0	0	0	0	0	0	0
30	0	0	0	0	0	0	0	0	0
31	0	0	0	0	0	0	0	0	0
32	0	0	0	0	0	0	0	0	0
33	0	0	0	0	0	0	0	0	0
34	0	0	0	0	0	0	0	0	0
35	0	0	0	0	0	0	0	0	0
36	0	0	0	0	0	0	0	0	0
37	0	0	0	0	0	0	0	0	0
38	0	0	0	0	0	0	0	0	0
39	0	0	0	0	0	0	0	0	0
40	0	0	0	0	0	0	0	0	0
41	0	0	0	0	0	0	0	0	0
42	0	0	0	0	0	0	0	0	0
43	0	0	0	0	0	0	0	0	0
44	0	0	0	0	0	0	0	0	0
45	0	0	0	0	0	0	0	0	0
46	0	0	0	0	0	0	0	0	0
47	0	0	0	0	0	0	0	0	0
48	0	0	0	0	0	0	0	0	0
49	0	0	0	0	0	0	0	0	0
50	0	0	0	0	0	0	0	0	0
51	0	0	0	0	0	0	0	0	0
52	0	0	0	0	0	0	0	0	0
53	0	0	0	0	0	0	0	0	0
54	0	0	0	0	0	0	0	0	0
55	0	0	0	0	0	0	0	0	0
56	0	0	0	0	0	0	0	0	0
57	0	0	0	0	0	0	0	0	0
58	0	0	0	0	0	0	0	0	0
59	0	0	0	0	0	0	0	0	0
60	0	0	0	0	0	0	0	0	0
61	0	0	0	0	0	0	0	0	0
62	0	0	0	0	0	0	0	0	0
63	0	0	0	0	0	0	0	0	0
64	0	0	0	0	0	0	0	0	0
65	0	0	0	0	0	0	0	0	0
66	0	0	0	0	0	0	0	0	0
67	0	0	0	0	0	0	0	0	0
68	0	0	0	0	0	0	0	0	0
69	0	0	0	0	0	0	0	0	0
70	0	0	0	0	0	0	0	0	0
71	0	0	0	0	0	0	0	0	0
72	0	0	0	0	0	0	0	0	0
73	0	0	0	0	0	0	0	0	0
74	0	0	0	0	0	0	0	0	0
75	0	0	0	0	0	0	0	0	0
76	0	0	0	0	0	0	0	0	0
77	0	0	0	0	0	0	0	0	0
78	0	0	0	0	0	0	0	0	0
79	0	0	0	0	0	0	0	0	0
80	0	0	0	0	0	0	0	0	0
81	0	0	0	0	0	0	0	0	0
82	0	0	0	0	0	0	0	0	0
83	0	0	0	0	0	0	0	0	0
84	0	0	0	0	0	0	0	0	0
85	0	0	0	0	0	0	0	0	0
86	0	0	0	0	0	0	0	0	0
87	0	0	0	0	0	0	0	0	0
88	0	0	0	0	0	0	0	0	0
89	0	0	0	0	0	0	0	0	0
90	0	0	0	0	0	0	0	0	0
91	0	0	0	0	0	0	0	0	0
92	0	0	0	0	0	0	0	0	0
93	0	0	0	0	0	0	0	0	0
94	0	0	0	0	0	0	0	0	0
95	0	0	0	0	0	0	0	0	0
96	0	0	0	0	0	0	0	0	0
97	0	0	0	0	0	0	0	0	0
98	0	0	0	0	0	0	0	0	0
99	0	0	0	0	0	0	0	0	0
100	0	0	0	0	0	0	0	0	0

	continued	sag1m_ISODATA_48classes.cls Horseshoe Bay - 1-meter imagery																	Column Total
		48	50	54	50	50	26	27	40	33	42	36	47	31	27	27	30	32	
17	16	0	0	0	0	0	0	0	0	0	0	0	0	0	0	0	0	13	
18	7	0	0	0	0	0	0	0	0	0	0	0	0	0	0	6	0	1	
18	12	0	0	0	4	0	3	0	0	1	0	0	0	0	0	9	0	1	
18	13	0	0	0	5	0	3	0	0	6	0	0	0	0	0	5	0	3	
18	14	0	0	0	0	0	0	1	0	0	0	0	0	0	0	2	0	2	
18	18	0	0	0	0	0	0	1	0	0	0	0	0	0	0	0	0	0	
20	48	0	0	0	0	1	0	0	0	0	0	0	0	0	0	0	0	0	
21	47	0	32	0	0	0	0	0	0	0	0	0	0	0	12	0	0	0	
22	36	0	0	0	0	0	0	0	0	0	0	0	0	0	0	0	0	0	
22	39	0	0	0	0	0	0	1	0	0	1	0	0	0	0	0	0	0	
22	41	0	0	0	0	0	0	0	0	0	0	0	0	0	0	0	0	0	
22	43	0	0	0	0	0	0	0	0	0	6	0	0	0	0	0	0	0	
23	31	0	0	0	0	0	0	0	0	0	0	0	0	8	0	0	0	0	
23	35	0	0	0	0	0	0	0	0	0	0	0	0	0	0	0	0	0	
24	40	0	0	0	0	0	0	0	0	0	2	0	0	0	1	0	0	0	
24	42	0	0	0	0	0	0	1	0	0	1	0	0	0	1	0	0	0	
24	44	0	1	0	0	2	0	0	0	0	0	0	0	0	1	0	0	0	
		48	50	54	50	50	26	27	40	33	42	36	47	31	27	27	30	32	

Compiled Restructured Matrix Summary	Row		Column		Diagonal	
	Total		Total		Total	
	1	46	48	31		
	2	0	50	0		
	3	71	54	44		
	4	47	50	41		
	5	32	50	18		
	6	21	26	13		
	7	23	27	23		
	8	40	40	40		
	9	26	33	26		
	10	25	42	18		
	11	0	36	0		
	12	83	47	47		
	13	27	31	22		
	14	21	27	6		
	15	0	27	0		
	16	47	30	30		
	17	22	32	13		
	18	117	82	64		
	19	0	44	0		
	20	204	100	100		
	21	130	116	41		
	22	120	113	106		
	23	28	25	19		
	24	45	45	35		

9	0	0	0	0	0	0	0	22
19	0	0	0	0	0	0	0	26
17	0	0	0	0	0	0	0	35
17	0	0	0	0	0	0	0	39
4	0	0	0	0	0	0	0	9
7	0	0	0	0	0	0	0	8
0	28	100	75	0	0	0	0	204
0	16	0	41	0	0	0	0	130
0	0	0	0	11	1	0	0	12
0	0	0	0	38	0	0	0	40
0	0	0	0	0	1	0	0	1
0	0	0	0	0	56	0	5	67
0	0	0	0	0	0	3	0	11
0	0	0	0	1	16	0	0	17
0	0	0	0	0	0	10	13	13
0	0	0	0	0	0	8	11	11
0	0	0	0	0	0	17	21	21
82	44	100	116	113	25	45	1175	

Confusion Matrix:

sag1m_MAXLIKE_70_24classes.cls
Horseshoe Bay - 1-meter imagery

Image Class	Ground Truth Class Code																
	1	2	3	4	5	6	7	8	9	10	11	12	13	14	15	16	17
0 Unclassified	2	0	0	0	0	0	0	0	0	0	0	0	0	1	1	3	1
1 chara	42	0	0	0	0	0	0	0	0	0	0	0	0	0	2	16	0
2 phragmites-clump	0	48	0	0	0	0	0	0	0	0	0	0	0	0	0	0	0
3 scival-dense	0	0	45	16	0	0	0	0	0	0	0	0	0	0	0	0	0
4 scival-clump	0	0	0	33	0	7	0	0	0	0	0	0	0	0	1	0	1
5 typha-soil2	0	2	0	0	50	0	0	0	0	7	0	0	4	5	0	0	0
6 sagrigida60/40	0	0	0	0	0	12	0	0	0	0	0	0	0	0	0	0	0
7 beachsand	0	0	0	0	0	0	27	0	0	1	0	0	0	0	0	0	0
8 shallowh20	0	0	0	0	0	0	0	40	0	0	0	0	0	0	1	0	0
9 hetdub	0	0	0	0	0	0	0	0	32	0	0	0	0	0	0	0	0
10 sagrigida_wes	0	0	1	0	0	7	0	0	0	27	0	0	0	0	0	0	0
11 vallisneria	0	0	0	0	0	0	0	0	0	0	36	0	0	0	0	0	0
12 deeph20	0	0	0	0	0	0	0	0	0	0	0	47	0	0	0	0	0
13 scivalbrown	0	0	0	0	0	0	0	0	0	0	0	0	23	0	0	0	0
14 leersia	0	0	0	0	0	0	0	0	0	0	0	0	0	10	0	0	0
15 muck	0	0	0	1	0	0	0	0	0	0	0	0	0	0	1	0	0
16 saggram/chara	0	0	0	0	0	0	0	0	0	0	0	0	0	0	0	9	0
17 typhah20	0	0	0	0	0	0	0	0	0	0	0	0	0	0	13	2	28
18 nuphar	4	0	0	0	0	0	0	0	1	0	0	0	0	0	8	0	2
19 eleocharis	0	0	0	0	0	0	0	0	0	4	0	0	0	1	0	0	0
20 impatians	0	0	0	0	0	0	0	0	0	0	0	0	0	0	0	0	0
21 bluejoint	0	0	0	0	0	0	0	0	0	0	0	0	0	0	0	0	0
22 cutgrass-eleocharis	0	0	0	0	0	0	0	0	0	0	0	0	3	0	0	0	0
23 eleocharis-sand	0	0	0	0	0	0	0	0	0	0	0	0	0	0	0	0	0
24 typha-phrag-scival	0	0	8	0	0	0	0	0	0	3	0	0	1	10	0	0	0
Column Total	48	50	54	50	50	26	27	40	33	42	36	47	31	27	27	30	32

Overall Accuracy: 86.81%
Kappa Coefficient: .8600

	Row	Image Class	Producers		Consumers		Omission		Commission	
			Accuracy (Percent)	Errors (Percent)	Accuracy (Percent)	Errors (Percent)	Errors (Percent)	Errors (Percent)		
0	9	Unclassified	87.50		70.00		12.50		37.50	
1	60	1 chara	96.00		100.00		4.00		0.00	
2	48	2 phragmites-clump	83.33		73.77		16.67		29.63	
3	61	3 scival-dense	66.00		78.57		34.00		18.00	
4	42	4 scival-clump	100.00		72.46		0.00		38.00	
5	69	5 typha-soil2	46.15		100.00		53.85		0.00	
6	12	6 sagrigida60/40	100.00		90.00		0.00		11.11	
7	30	7 beachsand	100.00		97.56		0.00		2.50	
8	41	8 shallowh20	96.97		100.00		3.03		0.00	
9	32	9 hetdub	64.29		77.14		35.71		19.05	
10	35	10 sagrigida	100.00		100.00		0.00		0.00	
11	36	11 vallisneria	100.00		100.00		0.00		0.00	
12	47	12 deeph20	74.19		100.00		25.81		0.00	
13	23	13 scivalbrown	37.04		100.00		62.96		0.00	
14	10	14 leersia	3.70		50.00		96.30		3.70	
15	2	15 muck	30.00		100.00		70.00		0.00	
16	9	16 saggram/chara	87.50		65.12		12.50		46.88	
17	43	17 typhah20	100.00		84.54		0.00		18.29	
18	97	18 nuphar	100.00		89.80		0.00		11.36	
19	44	19 eleocharis	100.00		100.00		0.00		0.00	
20	100	20 impatiens	100.00		100.00		0.00		0.00	
21	116	21 bluejoint	97.35		90.16		2.65		10.62	
22	122	22 cutgrass-eleocharis	56.00		87.50		44.00		8.00	
23	16	23 eleocharis-sand	97.78		66.67		2.22		48.89	
24	66	24 typha-phrag-scival								
82	44									

Confusion Matrix:

sag1m_SAM_25_24classes.cls
Horseshoe Bay - 1-meter imagery

Image Class	Ground Truth Class Code																
	<u>1</u>	<u>2</u>	<u>3</u>	<u>4</u>	<u>5</u>	<u>6</u>	<u>7</u>	<u>8</u>	<u>9</u>	<u>10</u>	<u>11</u>	<u>12</u>	<u>13</u>	<u>14</u>	<u>15</u>	<u>16</u>	<u>17</u>
0 Unclassified	0	0	0	0	0	0	0	0	0	0	0	0	0	0	0	0	0
1 chara	27	0	0	0	0	0	4	6	0	0	0	0	0	0	5	0	0
2 phragmites-clump	0	30	14	0	0	0	0	0	0	0	0	0	0	0	0	0	0
3 scival-dense	0	5	32	0	0	0	0	0	0	2	0	0	0	0	0	0	0
4 scival-clump	0	0	0	26	0	0	1	0	0	0	0	0	0	0	0	0	3
5 typha-soil2	0	5	3	0	38	0	0	0	0	0	0	0	0	7	0	0	0
6 sagrigida60/40	0	0	0	14	0	15	0	0	0	1	0	0	0	0	0	0	5
7 beachsand	0	0	0	0	0	0	16	0	0	0	0	0	0	0	5	0	0
8 shallowh20	14	0	0	0	0	0	3	19	0	0	0	0	0	0	0	2	0
9 hetdub	0	0	0	0	0	0	0	0	33	0	0	0	0	0	0	0	1
10 sagrigida_wes	0	6	2	0	0	2	0	0	0	32	0	0	0	1	0	0	0
11 vallisneria	0	0	0	0	0	0	0	0	0	0	36	0	0	0	0	0	0
12 deeph20	0	0	0	0	0	0	0	0	0	0	0	47	0	0	0	0	0
13 scivalbrown	0	0	0	0	0	0	0	0	0	0	0	0	31	0	0	0	0
14 leersia	0	0	0	0	0	0	0	0	0	2	0	0	0	15	0	0	0
15 muck	5	0	0	0	0	0	0	0	0	0	0	0	0	0	13	0	1
16 saggram/chara	0	0	0	0	0	0	0	15	0	0	0	0	0	0	0	28	0
17 typhah20	0	0	0	10	0	5	0	0	0	0	0	0	0	0	0	0	10
18 nuphar	2	0	0	0	0	3	0	0	0	0	0	0	0	0	1	0	12
19 eleocharis	0	0	0	0	0	0	0	0	0	0	0	0	0	1	0	0	0
20 impatiens	0	0	0	0	0	0	0	0	0	0	0	0	0	0	0	0	0
21 bluejoint	0	3	1	0	4	0	0	0	0	0	0	0	0	1	0	0	0
22 cutgrass-eleocharis	0	0	2	0	0	1	0	0	0	0	0	0	0	2	0	0	0
23 eleocharis-sand	0	0	0	0	0	0	3	0	0	0	0	0	0	0	3	0	0
24 typha-phrag-scival	0	1	0	0	8	0	0	0	0	5	0	0	0	0	0	0	0
Column Total	48	50	54	50	50	26	27	40	33	42	36	47	31	27	27	30	32

Overall Accuracy: 76.85%
Kappa Coefficient: .7555

		Row		Image Class		Producers		Consumers		Omission		Commission	
		24	Total			Accuracy	(Percent)	Accuracy	(Percent)	Errors	(Percent)	Errors	(Percent)
18	0	0	0	0	0	56.25	64.29	64.29	43.75	31.25			
0	0	0	0	0	0	60	57.69	57.69	40	44			
0	0	0	0	0	0	59.26	82.05	82.05	40.74	12.96			
0	0	0	0	0	0	52	86.67	86.67	48	8			
0	0	0	0	0	0	76	55.07	55.07	24	62			
0	0	0	0	0	0	57.69	42.86	42.86	42.31	76.92			
0	0	0	0	0	0	59.26	76.19	76.19	40.74	18.52			
0	0	0	0	0	0	47.5	50	50	52.5	47.5			
0	0	0	0	0	0	100	97.06	97.06	0	3.03			
0	0	0	0	0	0	76.19	57.14	57.14	23.81	57.14			
0	0	0	0	0	0	100	100	100	0	0			
0	0	0	0	0	0	100	100	100	0	0			
0	0	0	0	0	0	100	93.94	93.94	0	6.45			
0	0	0	0	0	0	55.56	75	75	44.44	18.52			
1	0	0	0	0	0	48.15	65	65	51.85	25.93			
0	0	0	0	0	0	93.33	65.12	65.12	6.67	50			
3	0	0	0	0	0	31.25	35.71	35.71	68.75	56.25			
77	0	0	0	0	0	93.9	81.05	81.05	6.1	21.95			
0	42	0	0	0	0	95.45	89.36	89.36	4.55	11.36			
0	0	100	0	0	0	100	100	100	0	0			
0	0	0	0	0	0	73.28	85.86	85.86	26.72	12.07			
0	0	0	0	0	0	99.12	95.73	95.73	0.88	4.42			
1	0	0	0	0	0	96	77.42	77.42	4	28			
0	1	0	0	0	0	33.33	34.88	34.88	66.67	62.22			
82	44	100	113	25	45								

Confusion Matrix:

sag1m_PCA654321_MAXLIKE_70_24classes.cls
Horseshoe Bay - 1-meter imagery

Image Class	Ground Truth Class Code																
	1	2	3	4	5	6	7	8	9	10	11	12	13	14	15	16	17
0 Unclassified	2	0	0	1	0	0	0	1	0	3	0	0	2	4	3	2	1
1 chara	38	0	0	0	0	0	0	0	0	0	0	0	0	0	2	1	0
2 phragmites-clump	0	48	0	0	0	0	0	0	0	0	0	0	0	0	0	0	0
3 scival-dense	0	0	45	0	0	0	0	0	0	0	0	0	0	0	0	0	0
4 scival-clump	0	0	0	49	0	1	0	0	0	0	0	0	0	0	2	0	1
5 typha-soil2	0	2	0	0	50	0	0	0	0	0	0	0	0	1	0	0	0
6 sagrigida60/40	0	0	0	0	0	23	0	0	0	0	0	0	0	0	0	0	0
7 beachsand	0	0	0	0	0	0	27	3	0	2	0	0	0	0	0	0	0
8 shallowh20	0	0	0	0	0	0	0	36	0	0	0	0	0	0	0	0	0
9 hetdub	0	0	0	0	0	0	0	0	33	0	0	0	0	0	0	0	0
10 sagrigida_wes	0	0	2	0	0	2	0	0	0	26	0	0	0	0	0	0	0
11 vallisneria	0	0	0	0	0	0	0	0	0	0	36	0	0	0	0	0	0
12 deeph20	0	0	0	0	0	0	0	0	0	0	0	47	0	0	0	0	0
13 scivalbrown	0	0	0	0	0	0	0	0	0	0	0	0	27	0	0	0	0
14 leersia	0	0	0	0	0	0	0	0	0	0	0	0	0	13	0	0	0
15 muck	0	0	0	0	0	0	0	0	0	0	0	0	0	0	1	0	0
16 saggram/chara	4	0	0	0	0	0	0	0	0	0	0	0	0	0	0	27	0
17 typhah20	1	0	0	0	0	0	0	0	0	0	0	0	0	0	5	0	28
18 nuphar	3	0	0	0	0	0	0	0	0	0	0	0	0	0	14	0	2
19 eleocharis	0	0	0	0	0	0	0	0	0	0	0	0	0	3	0	0	0
20 impatiens	0	0	0	0	0	0	0	0	0	0	0	0	0	0	0	0	0
21 bluejoint	0	0	0	0	0	0	0	0	0	0	0	0	0	0	0	0	0
22 cutgrass-eleocharis	0	0	0	0	0	0	0	0	0	0	0	0	0	0	0	0	0
23 eleocharis-sand	0	0	0	0	0	0	0	0	0	0	0	0	0	0	0	0	0
24 typha-phrag-scival	0	0	7	0	0	0	0	0	0	11	0	0	2	6	0	0	0
Column Total	48	50	54	50	50	26	27	40	33	42	36	47	31	27	27	30	32

Overall Accuracy: 89.79%
Kappa Coefficient: .8921

		Row		Image Class		Producers	Consumers	Omission	Commission
		24	Total			Accuracy (Percent)	Accuracy (Percent)	Errors (Percent)	Errors (Percent)
18	2	0	29	0	Unclassified	79.17	92.68	20.83	6.25
	0	0	41	1	chara	96	97.96	4	2
	0	0	49	2	phragmites-clump	83.33	100	16.67	0
	0	0	45	3	scival-dense	98	92.45	2	8
	0	0	53	4	scival-clump	100	94.34	0	6
	0	0	53	5	typha-soil2	88.46	100	11.54	0
	0	0	23	6	sagrigida60/40	100	84.38	0	18.52
	0	0	32	7	beachsand	90	100	10	0
	0	0	36	8	shallowh20	100	100	0	0
	0	0	33	9	hetdub	61.9	86.67	38.1	9.52
	0	0	30	10	sagrigida	100	100	0	0
	0	0	36	11	vallisneria	100	100	0	0
	0	0	47	12	deeph20	87.1	100	0	0
	0	0	27	13	scivalbrown	48.15	100	12.9	0
	0	1	14	14	leersia	3.7	92.86	51.85	3.7
	5	0	6	15	muck	90	16.67	96.3	18.52
	0	0	31	16	saggram/chara	87.5	87.1	10	13.33
	0	0	34	17	typhah20	91.46	82.35	12.5	18.75
75	0	0	94	18	nuphar	90.91	79.79	8.54	23.17
	40	0	43	19	eleocharis	100	93.02	9.09	6.82
	0	100	100	20	impatians	98.28	100	0	0
	0	0	114	21	bluejoint	94.69	100	1.72	0
	0	0	110	22	cutgrass-eleocharis	88	97.27	5.31	2.65
	0	0	25	23	eleocharis-sand	95.56	88	12	12
	0	0	70	24	typha-phrag-scival		61.43	4.44	60
82	44	100	1175	45					

Confusion Matrix:

sagIm_PCA654321_SAM_25_24classes.cls
Horseshoe Bay - 1-meter imagery

Image Class	Ground Truth Class Code																							
	1	2	3	4	5	6	7	8	9	10	11	12	13	14	15	16	17	18	19	20	21	22	23	24
0 Unclassified	0	0	28	0	0	16	23	0	1	17	0	0	0	0	1	0	0	0	0	0	0	0	0	0
1 chara	29	0	0	0	0	0	0	0	0	0	0	0	0	0	0	0	0	0	0	0	0	0	0	0
2 phragmites-clump	0	38	0	0	0	0	0	0	0	0	0	0	0	0	0	0	0	0	0	0	0	0	0	0
3 scival-dense	0	0	19	0	0	0	0	0	0	1	0	0	0	0	0	0	0	0	0	0	0	0	0	0
4 scival-clump	0	0	0	1	0	1	0	0	5	0	0	0	0	0	0	0	0	0	0	0	0	0	0	1
5 typha-soil2	0	8	0	0	40	0	0	0	0	4	0	0	0	0	0	0	0	0	0	0	0	0	0	0
6 sagrigida60/40	0	0	0	10	0	9	0	0	0	0	0	0	0	0	0	0	0	0	0	0	0	0	0	0
7 beachsand	0	0	0	0	0	0	4	0	0	0	0	0	0	0	0	0	0	0	0	0	0	0	0	0
8 shallowh20	0	0	0	0	0	0	0	40	0	0	0	0	0	0	0	0	0	0	0	0	0	0	0	2
9 hetdub	0	0	0	20	0	0	0	0	27	0	0	0	0	0	0	0	0	0	0	0	0	0	0	0
10 sagrigida_wes	0	0	7	0	0	0	0	0	0	3	0	0	0	0	0	0	0	0	0	0	0	0	0	0
11 valliseria	13	0	0	1	0	0	0	0	0	0	36	0	0	0	0	0	0	0	0	0	0	0	0	1
12 deeph20	0	0	0	18	0	0	0	0	0	0	0	47	0	0	0	0	0	0	0	0	0	0	0	0
13 scivalbrown	0	0	0	0	0	0	0	0	0	0	0	0	16	0	0	0	0	0	0	0	0	0	0	0
14 leersia	0	0	0	0	0	0	0	0	0	0	0	0	0	10	0	0	0	0	0	0	0	0	0	0
15 muck	0	0	0	0	0	0	0	0	0	0	0	0	0	0	0	0	0	0	0	0	0	0	0	0
16 saggram/chara	5	0	0	0	0	0	0	0	0	0	0	0	0	0	1	28	0	0	0	0	0	0	0	0
17 typhah20	0	0	0	0	0	0	0	0	0	0	0	0	0	0	0	0	0	0	0	0	0	0	0	6
18 nuphar	1	0	0	0	0	0	0	0	0	0	0	0	0	0	0	0	0	0	0	0	0	0	0	6
19 eleocharis	0	0	0	0	0	0	0	0	0	8	0	0	0	0	0	0	0	0	0	0	0	0	0	0
20 impatiens	0	0	0	0	5	0	0	0	0	2	0	0	0	0	0	0	0	0	0	0	0	0	0	0
21 bluejoint	0	4	0	0	0	0	0	0	0	0	0	0	0	0	0	0	0	0	0	0	0	0	0	0
22 cutgrass-eleocharis	0	0	0	0	0	0	0	0	0	0	0	0	1	2	0	0	0	0	0	0	0	0	0	0
23 eleocharis-sand	0	0	0	0	0	0	0	0	0	0	0	0	0	0	0	0	0	0	0	0	0	0	0	0
24 typha-phrag-scival	0	0	0	0	5	0	0	0	0	7	0	0	0	0	0	0	0	0	0	0	0	0	0	0
Column Total	48	50	54	50	50	26	27	40	33	42	36	47	31	27	27	30	32	3	6	6	0	0	0	0

Kappa Coefficient: .6409

196

Confusion Matrix:

prentiss_MAXLIKE_70_20classes.cls
Prentiss Bay 1-meter

Image Class	Ground Truth Class Code																
	<u>1</u>	<u>2</u>	<u>3</u>	<u>4</u>	<u>5</u>	<u>6</u>	<u>7</u>	<u>8</u>	<u>9</u>	<u>10</u>	<u>11</u>	<u>12</u>	<u>13</u>	<u>14</u>	<u>15</u>	<u>16</u>	<u>17</u>
0 Unclassified	0	0	0	1	1	0	2	1	0	20	1	1	0	1	3	1	0
1 stricta	33	22	21	7	20	0	0	0	0	0	0	0	0	0	0	0	0
2 stricta/lasio	0	0	0	0	0	0	0	0	0	0	0	0	0	0	0	0	0
3 lasio/acutus	0	0	0	0	0	0	0	0	0	0	0	0	0	0	0	0	0
4 lasio/typha50	0	0	0	0	0	0	0	0	0	0	0	0	0	0	0	0	0
5 roadside-veg	1	1	0	0	0	0	0	0	0	0	0	0	0	0	0	0	0
6 asphalt	0	0	0	0	0	25	0	0	0	2	0	0	0	0	0	0	0
7 80typha-west	0	0	0	0	0	0	20	17	9	0	1	0	0	0	0	0	0
8 acutus/typha50	0	0	1	8	0	0	9	10	6	0	1	0	0	0	0	0	0
9 acutus/soil60	0	0	0	0	0	0	0	0	7	0	2	0	0	0	0	0	0
10 dolomite	0	0	0	0	0	0	0	0	0	0	0	0	0	0	0	0	0
11 chara	0	0	0	0	0	0	0	0	0	0	0	0	0	0	0	0	0
12 soil70/typha15/acutus15	0	0	0	0	0	0	0	0	0	0	0	0	0	0	0	0	0
13 nuphar-12in	0	0	0	0	0	0	0	0	0	0	0	0	0	0	0	0	0
14 potomogeton-15in	0	0	0	0	0	0	0	0	0	0	0	0	0	0	0	0	0
15 muck-20cm	0	0	0	0	0	0	0	0	1	0	14	1	0	5	0	1	0
16 acutus-sparse	0	0	0	0	0	0	0	0	0	0	0	0	0	0	0	1	0
17 vallisneria	0	0	0	0	0	0	0	0	0	0	2	10	0	2	24	8	47
18 pine	0	0	0	0	0	0	0	0	0	0	0	0	0	0	0	0	0
19 shadow	0	0	0	0	0	0	0	0	0	0	0	0	0	0	0	0	0
20 acutusclumps-dense	0	0	0	0	3	0	0	0	0	0	1	9	22	14	1	14	0
Column Total	35	25	25	25	29	31	38	36	32	32	33	33	35	36	43	41	64

Overall Accuracy: 44.42%
Kappa Coefficient: .4046

		Row	Image Class				Producers	Consumers	Omission	Commission
		20	Total	0	1	2	Accuracy (Percent)	Accuracy (Percent)	Errors (Percent)	Errors (Percent)
18	0	0	32	0	0	0	97.06	32.04	2.94	205.88
	0	0	103	0	0	0	0	0	100	0
	0	0	0	0	0	0	0	0	100	0
	0	0	0	0	0	0	0	0	100	0
	0	0	0	0	0	0	0	0	100	0
	0	0	2	0	0	0	0	0	100	8.33
	0	0	27	0	0	0	100	92.59	0	8
	0	0	52	0	0	0	64.52	38.46	35.48	103.23
	0	0	35	0	0	0	35.71	28.57	64.29	89.29
	0	0	9	0	0	0	30.43	77.78	69.57	8.7
	0	0	0	0	0	0	0	0	100	0
	0	0	0	0	0	0	0	0	100	0
	0	0	0	0	0	0	0	0	100	0
	0	0	0	0	0	0	0	0	100	0
	0	0	0	0	0	0	0	0	100	0
	0	0	22	0	0	0	0	0	100	78.57
	0	0	1	0	0	0	4	100	96	0
	0	2	95	0	0	0	100	49.47	0	102.13
25	0	0	25	0	0	0	100	100	0	0
	0	21	21	0	0	0	91.3	100	8.7	0
	0	0	114	0	50	0	100	43.86	0	128
43	42	70	538							

Confusion Matrix:

prentiss_SAM_25_20classes.cls
Prentiss Bay 1-meter

		Ground Truth Class Code																
		<u>1</u>	<u>2</u>	<u>3</u>	<u>4</u>	<u>5</u>	<u>6</u>	<u>7</u>	<u>8</u>	<u>9</u>	<u>10</u>	<u>11</u>	<u>12</u>	<u>13</u>	<u>14</u>	<u>15</u>	<u>16</u>	<u>17</u>
0	Unclassified	0	0	0	0	0	0	0	0	0	0	0	0	0	0	0	0	0
1	stricta	28	1	0	0	1	0	0	0	0	0	0	0	0	0	0	0	0
2	stricta/lasio	4	9	3	0	0	0	0	0	0	0	0	0	0	0	0	0	0
3	lasio/acutus	1	8	17	2	0	0	0	0	0	0	0	0	0	0	0	0	0
4	lasio/typha50	0	5	2	19	0	0	0	0	0	0	0	0	0	0	0	0	0
5	roadside-veg	1	0	0	0	23	0	0	0	0	0	0	0	0	0	0	0	0
6	asphalt	0	0	0	0	0	25	0	0	0	2	0	0	0	1	6	0	0
7	80typha-west	0	0	0	0	0	0	27	12	1	0	0	0	0	0	0	0	0
8	acutus/typha50	0	0	0	0	0	0	4	16	1	2	0	0	0	0	0	0	0
9	acutus/soil60	0	0	0	0	0	0	0	0	21	1	0	0	0	1	0	0	0
10	dolomite	0	0	0	0	0	0	0	0	0	10	0	1	0	3	0	2	0
11	chara	0	0	0	0	0	0	0	0	0	7	21	17	0	2	0	0	0
12	soil70/typha15/acutus15	0	0	0	0	0	0	0	0	0	0	1	1	0	5	0	1	0
13	nuphar-12in	0	0	0	0	0	0	0	0	0	0	0	0	22	0	0	3	0
14	potomogeton-15in	0	0	0	0	0	0	0	0	0	0	0	2	0	6	1	1	0
15	muck-20cm	0	0	0	0	0	0	0	0	0	0	0	0	0	4	7	7	0
16	acutus-sparse	0	0	0	0	0	0	0	0	0	0	0	0	0	0	0	11	0
17	vallisneria	0	0	0	0	0	0	0	0	0	0	0	0	0	0	14	0	47
18	pine	0	0	0	0	0	0	0	0	0	0	0	0	0	0	0	0	0
19	shadow	0	0	0	0	0	0	0	0	0	0	0	0	0	0	0	0	0
20	acutuscumps-dense	0	0	0	0	0	0	0	0	0	0	0	0	0	0	0	0	0
Column Total		34	23	22	21	24	25	31	28	23	22	22	21	22	22	28	25	47

Row	Producers		Consumers		Omission		Commission	
	Image Class	Accuracy (Percent)	Accuracy (Percent)	Errors (Percent)	Errors (Percent)	Errors (Percent)		
18	0	0	0	0	0	0	0	
19	0	0	0	0	0	0	0	
20	0	0	0	0	0	0	0	
21	0	0	0	0	0	0	0	
22	0	0	0	0	0	0	0	
23	0	0	0	0	0	0	0	
24	0	0	0	0	0	0	0	
25	0	0	0	0	0	0	0	
26	0	0	0	0	0	0	0	
27	0	0	0	0	0	0	0	
28	0	0	0	0	0	0	0	
29	0	0	0	0	0	0	0	
30	0	0	0	0	0	0	0	
31	0	0	0	0	0	0	0	
32	0	0	0	0	0	0	0	
33	0	0	0	0	0	0	0	
34	0	0	0	0	0	0	0	
35	0	0	0	0	0	0	0	
36	0	0	0	0	0	0	0	
37	0	0	0	0	0	0	0	
38	0	0	0	0	0	0	0	
39	0	0	0	0	0	0	0	
40	0	0	0	0	0	0	0	
41	0	0	0	0	0	0	0	
42	0	0	0	0	0	0	0	
43	0	0	0	0	0	0	0	
44	0	0	0	0	0	0	0	
45	0	0	0	0	0	0	0	
46	0	0	0	0	0	0	0	
47	0	0	0	0	0	0	0	
48	0	0	0	0	0	0	0	
49	0	0	0	0	0	0	0	
50	0	0	0	0	0	0	0	
51	0	0	0	0	0	0	0	
52	0	0	0	0	0	0	0	
53	0	0	0	0	0	0	0	
54	0	0	0	0	0	0	0	
55	0	0	0	0	0	0	0	
56	0	0	0	0	0	0	0	
57	0	0	0	0	0	0	0	
58	0	0	0	0	0	0	0	
59	0	0	0	0	0	0	0	
60	0	0	0	0	0	0	0	
61	0	0	0	0	0	0	0	
62	0	0	0	0	0	0	0	
63	0	0	0	0	0	0	0	
64	0	0	0	0	0	0	0	
65	0	0	0	0	0	0	0	
66	0	0	0	0	0	0	0	
67	0	0	0	0	0	0	0	
68	0	0	0	0	0	0	0	
69	0	0	0	0	0	0	0	
70	0	0	0	0	0	0	0	
71	0	0	0	0	0	0	0	
72	0	0	0	0	0	0	0	
73	0	0	0	0	0	0	0	
74	0	0	0	0	0	0	0	
75	0	0	0	0	0	0	0	
76	0	0	0	0	0	0	0	
77	0	0	0	0	0	0	0	
78	0	0	0	0	0	0	0	
79	0	0	0	0	0	0	0	
80	0	0	0	0	0	0	0	
81	0	0	0	0	0	0	0	
82	0	0	0	0	0	0	0	
83	0	0	0	0	0	0	0	
84	0	0	0	0	0	0	0	
85	0	0	0	0	0	0	0	
86	0	0	0	0	0	0	0	
87	0	0	0	0	0	0	0	
88	0	0	0	0	0	0	0	
89	0	0	0	0	0	0	0	
90	0	0	0	0	0	0	0	
91	0	0	0	0	0	0	0	
92	0	0	0	0	0	0	0	
93	0							

Appendix C

2nd Der. <u>HB-1</u>	Band <u>HB-1</u>	2nd Der. <u>HB-2</u>	Band <u>HB-2</u>	2nd Der. <u>HB-3</u>	Band <u>HB-3</u>	2nd Der. <u>HB-4</u>	Band <u>HB-4</u>
-0.0116	731.5	-0.01237	720	-0.01592	720	-0.01088	720
-0.0103	720	-0.00961	731.5	-0.00704	812.3	-0.00545	812.3
-0.00617	823.9	-0.00684	823.9	-0.00683	708.5	-0.00417	731.5
-0.00548	812.3	-0.00627	812.3	-0.00635	823.9	-0.00416	708.5
-0.00484	916.7	-0.00352	708.5	-0.00539	731.5	-0.00402	823.9
-0.00397	800.8	-0.00327	916.7	-0.00279	800.8	-0.00186	800.8
-0.00245	905.1	-0.00309	800.8	-0.00249	560.1	-0.00154	560.1
-0.00207	708.5	-0.00176	560.1	-0.00226	571.4	-0.00147	571.4
-0.00206	560.1	-0.00152	905.1	-0.00112	548.8	-0.00096	639.7
-0.0019	928.3	-0.00141	639.7	-0.00111	639.7	-0.00092	548.8
.....
0.000984	893.4	0.001482	503.6	0.001421	777.7	0.001058	754.6
0.001711	503.6	0.001552	939.9	0.001691	928.3	0.001103	503.6
0.002017	514.9	0.001746	514.9	0.001796	514.9	0.001213	777.7
0.002704	939.9	0.002255	743	0.002786	754.6	0.001464	514.9
0.003322	847.1	0.003417	754.6	0.0035	847.1	0.002303	847.1
0.003469	754.6	0.003503	847.1	0.003837	674.1	0.002868	674.1
0.003983	674.1	0.003624	674.1	0.00539	835.5	0.004007	835.5
0.004392	835.5	0.004916	835.5	0.007499	697	0.004658	743
0.011892	697	0.010217	697	0.00762	743	0.005847	697
0.012594	685.5	0.011146	685.5	0.009756	685.5	0.007218	685.5
.....
2nd Der. <u>HB-5</u>	Band <u>HB-5</u>	2nd Der. <u>HB-6</u>	Band <u>HB-6</u>	2nd Der. <u>HB-7</u>	Band <u>HB-7</u>	2nd Der. <u>HB-8</u>	Band <u>HB-8</u>
-0.00922	731.5	-0.00699	743	-0.01343	743	-0.00517	708.5
-0.00606	812.3	-0.00605	731.5	-0.00891	928.3	-0.0033	697
-0.00604	720	-0.00453	916.7	-0.00818	754.6	-0.00294	720
-0.00435	928.3	-0.00372	766.1	-0.0054	731.5	-0.00289	812.3
-0.0043	823.9	-0.00223	812.3	-0.00539	916.7	-0.00167	651.2
-0.00293	800.8	-0.00221	754.6	-0.00407	766.1	-0.00164	823.9
-0.00292	916.7	-0.00204	823.9	-0.00298	777.7	-0.0012	800.8
-0.00226	743	-0.00184	800.8	-0.00265	881.9	-0.00109	582.8
-0.00181	905.1	-0.00153	928.3	-0.00217	812.3	-0.00101	594.1
-0.00156	560.1	-0.00137	881.9	-0.00214	800.8	-0.00091	571.4
.....
0.000616	492.4	0.00103	503.6	0.000728	582.8	0.0006	605.5
0.000718	582.8	0.00121	847.1	0.001293	503.6	0.000723	616.9
0.001524	503.6	0.001392	514.9	0.001795	835.5	0.000735	777.7
0.00165	514.9	0.002025	674.1	0.00185	514.9	0.001088	847.1
0.00195	847.1	0.002115	835.5	0.002251	674.1	0.001116	754.6
0.00323	674.1	0.002611	720	0.006691	685.5	0.001573	685.5
0.004191	835.5	0.002815	939.9	0.008287	939.9	0.002298	835.5
0.004466	939.9	0.005245	708.5	0.00933	708.5	0.002311	674.1
0.009803	697	0.00547	685.5	0.009607	697	0.003572	731.5
0.009893	685.5	0.007181	697	0.010469	720	0.004878	743

2nd Der. HB-9	Band HB-9	2nd Der. HB-10	Band HB-10	2nd Der. HB-11	Band HB-11	2nd Der. HB-12	Band HB-12
-0.00539	708.5	-0.0053	708.5	-0.00633	708.5	-0.02376	743
-0.00346	720	-0.00334	697	-0.0062	720	-0.01751	754.6
-0.00346	697	-0.00322	812.3	-0.00331	812.3	-0.01698	928.3
-0.0034	812.3	-0.00309	720	-0.00239	823.9	-0.00918	766.1
-0.00211	823.9	-0.00176	651.2	-0.00145	800.8	-0.00828	916.7
-0.00176	651.2	-0.00173	823.9	-0.0009	639.7	-0.00787	731.5
-0.00147	800.8	-0.00129	800.8	-0.00061	651.2	-0.00589	560.1
-0.00107	582.8	-0.00113	582.8	-0.00041	571.4	-0.0055	777.7
-0.00096	594.1	-0.001	594.1	-0.00037	537.5	-0.00499	548.8
-0.00093	571.4	-0.0009	571.4	-0.00033	526.2	-0.00449	537.5
.....
0.000572	766.1	0.000636	605.5	0.000514	503.6	0.002693	582.8
0.000709	616.9	0.000643	616.9	0.000541	514.9	0.003034	823.9
0.000737	777.7	0.000711	777.7	0.000743	731.5	0.00449	503.6
0.001157	847.1	0.001264	847.1	0.000763	777.7	0.005521	514.9
0.001257	754.6	0.001272	754.6	0.001424	847.1	0.007165	708.5
0.001845	685.5	0.001628	685.5	0.001547	754.6	0.008239	674.1
0.002479	674.1	0.002376	674.1	0.00266	835.5	0.012789	720
0.00292	835.5	0.002387	835.5	0.002696	674.1	0.017855	939.9
0.00355	731.5	0.00354	731.5	0.004121	743	0.020204	697
0.005263	743	0.00498	743	0.005234	685.5	0.02338	685.5
.....
2nd Der. HB-13	Band HB-13	2nd Der. HB-14	Band HB-14	2nd Der. HB-15	Band HB-15	2nd Der. HB-16	Band HB-16
-0.01656	743	-0.03446	743	-0.01124	743	-0.00879	928.3
-0.01242	731.5	-0.02378	731.5	-0.00789	928.3	-0.00716	743
-0.01149	928.3	-0.01605	754.6	-0.00642	731.5	-0.00666	731.5
-0.00642	754.6	-0.01348	928.3	-0.00601	754.6	-0.00348	916.7
-0.00583	916.7	-0.01178	916.7	-0.00556	916.7	-0.00321	754.6
-0.00509	777.7	-0.01134	766.1	-0.00378	766.1	-0.00195	777.7
-0.00342	560.1	-0.0066	560.1	-0.0018	560.1	-0.00157	881.9
-0.00302	881.9	-0.00554	548.8	-0.00167	777.7	-0.0015	560.1
-0.00275	548.8	-0.00473	537.5	-0.00158	881.9	-0.00128	893.4
-0.00254	537.5	-0.00441	881.9	-0.00143	548.8	-0.0011	548.8
.....
0.001516	582.8	0.002161	594.1	0.000507	594.1	0.000776	582.8
0.002204	503.6	0.003321	582.8	0.000811	582.8	0.0008	823.9
0.002602	823.9	0.004017	503.6	0.000979	503.6	0.000933	503.6
0.003332	514.9	0.006681	514.9	0.001752	514.9	0.001158	720
0.00396	674.1	0.006683	674.1	0.002136	674.1	0.001719	514.9
0.005135	720	0.013421	720	0.00503	939.9	0.002104	674.1
0.007379	708.5	0.016018	939.9	0.006648	685.5	0.004269	708.5
0.013359	685.5	0.019267	708.5	0.006743	720	0.006873	685.5
0.013812	939.9	0.023247	685.5	0.008306	708.5	0.00808	939.9
0.015648	697	0.031895	697	0.009715	697	0.008923	697

2nd Der. <u>HB-17</u>	Band <u>HB-17</u>	2nd Der. <u>HB-18</u>	Band <u>HB-18</u>	2nd Der. <u>HB-19</u>	Band <u>HB-19</u>	2nd Der. <u>HB-20</u>	Band <u>HB-20</u>
-0.00498	928.3	-0.00794	928.3	-0.01662	720	-0.01443	720
-0.00411	743	-0.00363	731.5	-0.00836	731.5	-0.00749	708.5
-0.00405	731.5	-0.00361	754.6	-0.00665	823.9	-0.00669	812.3
-0.00316	754.6	-0.00291	720	-0.00648	708.5	-0.00496	823.9
-0.00172	916.7	-0.00258	812.3	-0.00612	812.3	-0.00468	731.5
-0.00164	571.4	-0.00207	893.4	-0.00289	560.1	-0.00258	800.8
-0.00155	651.2	-0.00195	916.7	-0.0028	571.4	-0.00228	560.1
-0.00142	777.7	-0.00192	743	-0.00274	905.1	-0.00226	571.4
-0.00125	560.1	-0.00184	560.1	-0.00263	800.8	-0.0013	639.7
-0.00121	893.4	-0.00168	823.9	-0.00253	916.7	-0.00113	905.1
.....
0.000608	628.3	0.000674	492.4	0.001255	503.6	0.001228	503.6
0.000741	858.7	0.000837	628.3	0.001929	514.9	0.001673	514.9
0.000745	870.3	0.001269	503.6	0.002269	754.6	0.001829	766.1
0.001046	492.4	0.00127	514.9	0.003109	847.1	0.002719	939.9
0.001093	503.6	0.001574	939.9	0.003906	939.9	0.00279	847.1
0.001296	514.9	0.001679	766.1	0.004845	743	0.004666	674.1
0.003186	697	0.00169	835.5	0.004861	674.1	0.005003	835.5
0.004128	939.9	0.004026	697	0.004887	835.5	0.005829	743
0.004963	674.1	0.004586	674.1	0.010683	697	0.007683	697
0.009404	685.5	0.00922	685.5	0.013302	685.5	0.011161	685.5
.....
2nd Der. <u>HB-21</u>	Band <u>HB-21</u>	2nd Der. <u>HB-22</u>	Band <u>HB-22</u>	2nd Der. <u>HB-23</u>	Band <u>HB-23</u>	2nd Der. <u>HB-24</u>	Band <u>HB-24</u>
-0.01788	743	-0.00944	743	-0.00812	928.3	-0.02004	743
-0.01235	731.5	-0.00472	754.6	-0.00644	743	-0.01916	754.6
-0.00855	928.3	-0.00453	766.1	-0.00615	754.6	-0.01879	928.3
-0.00721	754.6	-0.00427	916.7	-0.00391	731.5	-0.01439	766.1
-0.0057	777.7	-0.00419	928.3	-0.00264	766.1	-0.01143	916.7
-0.00567	916.7	-0.00248	777.7	-0.00191	812.3	-0.00467	881.9
-0.00303	800.8	-0.00189	881.9	-0.00185	905.1	-0.00457	777.7
-0.00302	560.1	-0.00178	731.5	-0.00146	893.4	-0.00359	893.4
-0.00244	548.8	-0.00137	800.8	-0.00132	560.1	-0.00335	847.1
-0.0024	881.9	-0.00097	870.3	-0.00097	537.5	-0.00293	789.2
.....
0.000841	594.1	0.000331	594.1	0.000575	594.1	0.001616	582.8
0.001392	582.8	0.000473	582.8	0.000825	503.6	0.001873	905.1
0.001691	503.6	0.00056	503.6	0.001004	835.5	0.002682	514.9
0.002974	674.1	0.000987	514.9	0.001332	514.9	0.002802	823.9
0.003183	514.9	0.001217	674.1	0.001626	674.1	0.003505	674.1
0.008415	720	0.003315	685.5	0.003903	685.5	0.011277	685.5
0.010558	685.5	0.005278	697	0.004632	720	0.014168	708.5
0.01115	708.5	0.006047	939.9	0.004715	939.9	0.015448	697
0.011345	939.9	0.006839	708.5	0.005597	708.5	0.015527	939.9
0.015149	697	0.008864	720	0.006245	697	0.021887	720

2nd Der. HB-25	Band HB-25	2nd Der. HB-26	Band HB-26	2nd Der. HB-27	Band HB-27	2nd Der. HB-28	Band HB-28
-0.02589	928.3	-0.01778	928.3	-0.02294	743	-0.02612	743
-0.02541	743	-0.0157	743	-0.01893	928.3	-0.02129	928.3
-0.01901	754.6	-0.01189	731.5	-0.01403	916.7	-0.01741	754.6
-0.01788	731.5	-0.00992	754.6	-0.01007	766.1	-0.01186	731.5
-0.00677	916.7	-0.00815	916.7	-0.00976	754.6	-0.00706	916.7
-0.00676	777.7	-0.00326	777.7	-0.00904	731.5	-0.00677	766.1
-0.00583	560.1	-0.00323	893.4	-0.006	881.9	-0.00631	777.7
-0.00524	893.4	-0.00309	881.9	-0.00531	777.7	-0.00408	560.1
-0.00485	548.8	-0.00255	560.1	-0.00311	870.3	-0.00358	893.4
-0.00466	537.5	-0.0025	537.5	-0.00288	560.1	-0.00349	881.9
.....
0.002898	905.1	0.001491	905.1	0.001528	582.8	0.001899	503.6
0.003215	503.6	0.001612	823.9	0.001743	503.6	0.001906	582.8
0.003919	823.9	0.001852	503.6	0.002771	812.3	0.002292	823.9
0.004794	674.1	0.003003	514.9	0.003602	514.9	0.003239	674.1
0.005928	514.9	0.005329	674.1	0.004322	674.1	0.003795	514.9
0.013005	720	0.007693	720	0.011402	685.5	0.011126	685.5
0.015914	685.5	0.008425	708.5	0.014222	708.5	0.018723	939.9
0.016332	708.5	0.014077	697	0.016401	697	0.01982	720
0.022842	939.9	0.01478	685.5	0.018005	720	0.019825	697
0.024662	697	0.01523	939.9	0.022899	939.9	0.020074	708.5
.....
2nd Der. HB-29	Band HB-29	2nd Der. HB-30	Band HB-30	2nd Der. HB-31	Band HB-31	2nd Der. HB-32	Band HB-32
-0.01676	731.5	-0.02402	928.3	-0.02642	743	-0.00551	928.3
-0.01645	743	-0.01688	731.5	-0.02225	731.5	-0.00179	916.7
-0.01559	928.3	-0.01234	754.6	-0.01613	916.7	-0.0015	458.8
-0.00866	754.6	-0.01222	743	-0.01405	766.1	-0.00138	447.7
-0.00842	916.7	-0.00616	720	-0.00457	560.1	-0.00134	881.9
-0.00517	560.1	-0.00443	893.4	-0.00439	823.9	-0.00116	858.7
-0.0043	548.8	-0.00363	639.7	-0.00401	777.7	-0.00108	905.1
-0.00384	766.1	-0.00289	537.5	-0.00386	548.8	-0.00097	605.5
-0.00371	537.5	-0.00278	789.2	-0.00371	928.3	-0.00093	571.4
-0.0026	881.9	-0.00251	605.5	-0.00339	537.5	-0.00091	777.7
.....
0.00121	594.1	0.001172	662.6	0.002853	503.6	0.000528	560.1
0.002225	582.8	0.001739	766.1	0.003516	893.4	0.000541	594.1
0.003077	720	0.002469	582.8	0.004531	674.1	0.000587	616.9
0.003236	503.6	0.002674	503.6	0.004884	514.9	0.000687	470
0.005331	514.9	0.003375	835.5	0.005292	812.3	0.000695	514.9
0.006171	674.1	0.003999	514.9	0.011189	939.9	0.000729	481.2
0.007493	708.5	0.009034	674.1	0.015097	720	0.00074	436.5
0.014028	939.9	0.014666	939.9	0.01603	708.5	0.000961	835.5
0.018593	685.5	0.021063	697	0.016523	685.5	0.001106	870.3
0.019981	697	0.025434	685.5	0.021392	697	0.005863	939.9

2nd Der. PB-1	Band PB-1	2nd Der. PB-2	Band PB-2	2nd Der. PB-3	Band PB-3	2nd Der. PB-4	Band PB-4
-0.00213	743	-0.00392	743	-0.00426	743	-0.02366	731.5
-0.00198	916.7	-0.00291	916.7	-0.00335	916.7	-0.01512	743
-0.00186	754.6	-0.0023	754.6	-0.00228	766.1	-0.01283	720
-0.00177	766.1	-0.00213	928.3	-0.00209	731.5	-0.00956	560.1
-0.00135	731.5	-0.00192	731.5	-0.00207	754.6	-0.00952	754.6
-0.00133	928.3	-0.0016	766.1	-0.00135	928.3	-0.00759	928.3
-0.00083	789.2	-0.00068	870.3	-0.00066	905.1	-0.00745	548.8
-0.00063	905.1	-0.0006	560.1	-0.00044	881.9	-0.0066	916.7
-0.00052	858.7	-0.00038	548.8	-0.00042	870.3	-0.00543	537.5
-0.00051	425.4	-0.00036	812.3	-0.00041	548.8	-0.00483	571.4
.....
0.000401	594.1	0.000346	582.8	0.000246	582.8	0.002427	526.2
0.000467	514.9	0.000379	594.1	0.00025	893.4	0.003275	594.1
0.000475	503.6	0.000379	823.9	0.000385	514.9	0.003713	503.6
0.000913	674.1	0.000654	514.9	0.000418	594.1	0.004264	582.8
0.001124	720	0.000834	674.1	0.0007	674.1	0.006571	708.5
0.001131	777.7	0.002127	685.5	0.001518	685.5	0.006997	674.1
0.001696	939.9	0.00246	720	0.00204	939.9	0.007802	939.9
0.001715	708.5	0.003008	939.9	0.00316	697	0.009012	514.9
0.001764	685.5	0.003131	708.5	0.003342	720	0.021881	685.5
0.002394	697	0.003192	697	0.004082	708.5	0.032092	697
2nd Der. PB-5	Band PB-5	2nd Der. PB-6	Band PB-6	2nd Der. PB-7	Band PB-7	2nd Der. PB-8	Band PB-8
-0.01101	731.5	-0.00348	731.5	-0.02573	731.5	-0.01453	731.5
-0.00845	720	-0.00227	743	-0.01645	743	-0.01258	720
-0.00627	743	-0.00214	720	-0.01378	720	-0.00675	743
-0.00582	928.3	-0.00182	916.7	-0.01013	560.1	-0.00433	928.3
-0.00435	916.7	-0.00174	754.6	-0.00975	928.3	-0.00426	708.5
-0.00258	754.6	-0.00163	812.3	-0.00806	754.6	-0.00371	916.7
-0.00216	708.5	-0.00155	766.1	-0.00761	548.8	-0.00299	605.5
-0.00213	571.4	-0.00104	560.1	-0.00533	916.7	-0.00299	560.1
-0.00205	560.1	-0.00101	905.1	-0.00475	537.5	-0.00272	571.4
-0.00193	639.7	-0.00099	928.3	-0.00454	571.4	-0.00245	639.7
0.000736	594.1	0.000471	662.6	0.002722	594.1	0.000923	492.4
0.000742	582.8	0.000674	503.6	0.003557	526.2	0.001244	582.8
0.000852	492.4	0.000762	708.5	0.003605	503.6	0.001362	628.3
0.001116	662.6	0.000914	514.9	0.003983	582.8	0.001699	662.6
0.001458	939.9	0.001007	835.5	0.006879	708.5	0.001866	503.6
0.001732	503.6	0.001303	777.7	0.007286	674.1	0.004135	514.9
0.002852	514.9	0.001933	939.9	0.008132	939.9	0.005266	939.9
0.006114	674.1	0.002451	674.1	0.008389	514.9	0.006788	674.1
0.014051	697	0.004546	697	0.023562	685.5	0.019428	697
0.016412	685.5	0.004815	685.5	0.034532	697	0.019766	685.5

2nd Der. PB-9	Band PB-9	2nd Der. PB-10	Band PB-10	2nd Der. PB-11	Band PB-11	2nd Der. PB-12	Band PB-12
-0.00194	812.3	-0.00217	812.3	-0.00422	916.7	-0.00201	708.5
-0.0016	720	-0.00185	720	-0.00324	928.3	-0.00156	916.7
-0.00157	708.5	-0.00181	708.5	-0.0021	905.1	-0.00121	905.1
-0.00154	823.9	-0.0018	823.9	-0.002	458.8	-0.00094	766.1
-0.00073	800.8	-0.00093	697	-0.00197	571.4	-0.0009	731.5
-0.00068	697	-0.00082	800.8	-0.00165	777.7	-0.00084	720
-0.00046	651.2	-0.00052	651.2	-0.00144	708.5	-0.00082	651.2
-0.00023	905.1	-0.00025	582.8	-0.0014	881.9	-0.00076	425.4
-0.00019	571.4	-0.00024	905.1	-0.00121	870.3	-0.00058	571.4
-0.00018	582.8	-0.00024	870.3	-0.0012	662.6	-0.00047	458.8
.....
0.000217	447.7	0.000259	766.1	0.000738	720	0.000276	492.4
0.000339	939.9	0.000483	685.5	0.000999	823.9	0.000404	470
0.000412	685.5	0.000527	928.3	0.001079	893.4	0.000409	514.9
0.0005	777.7	0.00053	777.7	0.001153	470	0.000426	503.6
0.000516	731.5	0.000715	731.5	0.001157	514.9	0.000445	436.5
0.000567	754.6	0.000717	754.6	0.001169	481.2	0.000488	939.9
0.000794	674.1	0.000817	674.1	0.001639	674.1	0.000509	893.4
0.000842	847.1	0.000914	847.1	0.002209	754.6	0.000687	754.6
0.001329	835.5	0.001586	835.5	0.002941	685.5	0.002714	674.1
0.001976	743	0.002374	743	0.006552	939.9	0.003725	685.5
2nd Der. PB-13	Band PB-13	2nd Der. PB-14	Band PB-14	2nd Der. PB-15	Band PB-15	2nd Der. PB-16	Band PB-16
-0.00273	928.3	-0.00486	928.3	-0.01056	743	-0.01203	754.6
-0.00261	916.7	-0.00307	754.6	-0.00986	731.5	-0.01023	928.3
-0.00195	905.1	-0.00269	743	-0.00698	754.6	-0.00876	731.5
-0.00148	425.4	-0.0023	731.5	-0.00633	928.3	-0.00858	743
-0.0008	708.5	-0.0015	916.7	-0.00482	560.1	-0.00435	560.1
-0.00071	812.3	-0.00109	893.4	-0.00352	548.8	-0.00297	537.5
-0.00067	835.5	-0.00102	560.1	-0.00322	916.7	-0.00289	548.8
-0.00058	789.2	-0.00081	458.8	-0.00248	537.5	-0.00283	812.3
-0.0005	651.2	-0.00071	548.8	-0.00233	571.4	-0.00283	720
-0.00046	571.4	-0.00069	537.5	-0.00227	766.1	-0.0027	893.4
.....
0.000328	503.6	0.00036	662.6	0.000924	526.2	0.001432	594.1
0.000369	800.8	0.000434	628.3	0.001579	594.1	0.00186	835.5
0.00037	481.2	0.000601	582.8	0.001879	582.8	0.001883	582.8
0.00041	628.3	0.000695	503.6	0.002291	503.6	0.002372	503.6
0.000417	743	0.000807	708.5	0.002568	708.5	0.003604	674.1
0.000483	881.9	0.000876	514.9	0.004262	514.9	0.004072	708.5
0.000845	436.5	0.001494	674.1	0.004336	674.1	0.004093	514.9
0.001159	685.5	0.003763	685.5	0.006475	939.9	0.005898	939.9
0.001162	674.1	0.003785	939.9	0.013568	685.5	0.012013	685.5
0.00224	939.9	0.004277	697	0.015389	697	0.015534	697

2nd Der. PB-17	Band PB-17	2nd Der. PB-18	Band PB-18	2nd Der. PB-19	Band PB-19	2nd Der. PB-20	Band PB-20
-0.00362	928.3	-0.029	743	-0.01094	743	-0.00484	916.7
-0.00211	743	-0.02126	731.5	-0.00805	731.5	-0.00473	743
-0.002	916.7	-0.01576	754.6	-0.00647	928.3	-0.00465	731.5
-0.00173	731.5	-0.01117	928.3	-0.00558	754.6	-0.0025	766.1
-0.00092	754.6	-0.00787	916.7	-0.00441	916.7	-0.00138	777.7
-0.0007	847.1	-0.00573	766.1	-0.00248	766.1	-0.00115	651.2
-0.00057	881.9	-0.00464	777.7	-0.00243	777.7	-0.00103	708.5
-0.00055	571.4	-0.0041	537.5	-0.00196	560.1	-0.00091	835.5
-0.00051	548.8	-0.00384	560.1	-0.00167	548.8	-0.0009	720
-0.00042	777.7	-0.00316	639.7	-0.00153	537.5	-0.00083	905.1
.....
0.000325	651.2	0.001714	662.6	0.000781	594.1	0.000482	492.4
0.000359	708.5	0.002719	582.8	0.001001	582.8	0.000652	928.3
0.000447	823.9	0.003714	503.6	0.00143	503.6	0.000878	812.3
0.000537	720	0.005127	514.9	0.002203	514.9	0.000942	503.6
0.000609	674.1	0.006424	720	0.003275	674.1	0.001	514.9
0.000707	594.1	0.008042	674.1	0.004665	720	0.001832	754.6
0.000894	514.9	0.011519	708.5	0.00509	939.9	0.002261	939.9
0.002346	697	0.013314	939.9	0.006059	708.5	0.004078	697
0.00258	685.5	0.026453	685.5	0.009847	685.5	0.004121	674.1
0.004592	939.9	0.030069	697	0.010249	697	0.008436	685.5
2nd Der. PB-21	Band PB-21	2nd Der. PB-22	Band PB-22	2nd Der. PB-23	Band PB-23	2nd Der. PB-24	Band PB-24
-0.00218	708.5	-0.00322	916.7	-0.00169	916.7	-0.01437	743
-0.00175	916.7	-0.00212	458.8	-0.00149	425.4	-0.01358	731.5
-0.00089	651.2	-0.00164	447.7	-0.00104	458.8	-0.01205	754.6
-0.00071	743	-0.00137	571.4	-0.00086	766.1	-0.01094	928.3
-0.00069	766.1	-0.00135	582.8	-0.00071	447.7	-0.00804	548.8
-0.00063	571.4	-0.00133	743	-0.00059	605.5	-0.00763	560.1
-0.00061	731.5	-0.00126	777.7	-0.00058	743	-0.00541	537.5
-0.00052	835.5	-0.00121	605.5	-0.00055	905.1	-0.0039	571.4
-0.00046	905.1	-0.00116	708.5	-0.0005	526.2	-0.00291	916.7
-0.00045	697	-0.00095	766.1	-0.00049	571.4	-0.00229	777.7
.....
0.000281	481.2	0.000657	893.4	0.000334	651.2	0.001797	492.4
0.000282	492.4	0.000711	436.5	0.00038	720	0.002065	582.8
0.000401	847.1	0.000712	651.2	0.000459	893.4	0.003537	526.2
0.000415	503.6	0.000919	560.1	0.000482	514.9	0.004442	939.9
0.000437	514.9	0.000948	720	0.000609	560.1	0.004729	503.6
0.00049	436.5	0.00118	514.9	0.000685	436.5	0.005506	674.1
0.001006	754.6	0.001449	685.5	0.00069	481.2	0.006414	708.5
0.001576	939.9	0.00181	481.2	0.000925	928.3	0.009158	514.9
0.002724	674.1	0.002113	754.6	0.001071	939.9	0.015595	685.5
0.003712	685.5	0.004143	939.9	0.001098	754.6	0.019587	697

2nd Der. PB-25	Band PB-25	2nd PB-26	Band PB-26	2nd Der. PB-27	Band PB-27	2nd Der. PB-28	Band PB-28
-0.0115	743	-0.02419	743	-0.02278	743	-0.00881	743
-0.01001	731.5	-0.01351	731.5	-0.01163	731.5	-0.00789	731.5
-0.00624	916.7	-0.0112	766.1	-0.01101	754.6	-0.00787	916.7
-0.00462	754.6	-0.01007	916.7	-0.01049	766.1	-0.00424	928.3
-0.00302	766.1	-0.00788	754.6	-0.00827	928.3	-0.00363	766.1
-0.00295	928.3	-0.0071	928.3	-0.00784	916.7	-0.00228	870.3
-0.0029	560.1	-0.00545	777.7	-0.00528	560.1	-0.0015	881.9
-0.00262	548.8	-0.00489	560.1	-0.00385	548.8	-0.0014	560.1
-0.00238	537.5	-0.0043	881.9	-0.0035	777.7	-0.00116	537.5
-0.00196	777.7	-0.00391	548.8	-0.00335	881.9	-0.00111	777.7
.....
0.001163	594.1	0.002346	812.3	0.001686	893.4	0.000769	582.8
0.00151	582.8	0.00256	893.4	0.002279	582.8	0.001062	503.6
0.001744	720	0.002704	503.6	0.002778	503.6	0.001473	812.3
0.002087	503.6	0.004432	514.9	0.004383	674.1	0.001513	514.9
0.003143	514.9	0.004467	674.1	0.004621	514.9	0.002312	720
0.003577	674.1	0.013357	708.5	0.011139	939.9	0.003184	674.1
0.00518	708.5	0.014122	685.5	0.012901	708.5	0.004151	708.5
0.005574	939.9	0.014644	939.9	0.013341	720	0.007184	939.9
0.011682	685.5	0.015493	720	0.014272	685.5	0.00899	697
0.013084	697	0.018385	697	0.018547	697	0.009623	685.5
.....
2nd Der. PB-29	Band PB-29	2nd PB-30	Band PB-30	2nd Der. PB-31	Band PB-31	2nd Der. PB-32	Band PB-32
-0.0045	731.5	-0.00353	916.7	-0.00155	731.5	-0.0062	743
-0.00431	743	-0.00306	766.1	-0.00149	916.7	-0.00443	731.5
-0.00387	916.7	-0.00229	731.5	-0.00136	708.5	-0.00378	916.7
-0.00373	928.3	-0.00216	708.5	-0.00119	766.1	-0.00266	928.3
-0.00301	766.1	-0.00161	743	-0.00112	743	-0.00239	766.1
-0.00109	560.1	-0.0011	835.5	-0.00081	651.2	-0.00152	881.9
-0.00106	548.8	-0.0009	639.7	-0.00057	605.5	-0.00104	870.3
-0.00097	905.1	-0.00089	594.1	-0.00055	720	-0.00101	777.7
-0.00086	870.3	-0.00085	800.8	-0.00051	571.4	-0.00081	754.6
-0.00084	537.5	-0.00083	905.1	-0.00046	928.3	-0.00067	800.8
.....
0.00048	662.6	0.000805	616.9	0.000205	481.2	0.000463	582.8
0.000841	582.8	0.000831	514.9	0.000217	858.7	0.000505	893.4
0.000976	514.9	0.000925	436.5	0.000258	812.3	0.000805	812.3
0.001036	777.7	0.001274	928.3	0.000287	503.6	0.000864	674.1
0.001043	503.6	0.001378	893.4	0.000312	492.4	0.000873	514.9
0.002236	674.1	0.001688	812.3	0.000579	514.9	0.003135	685.5
0.002246	708.5	0.002983	674.1	0.001022	754.6	0.003206	720
0.003629	939.9	0.003318	754.6	0.001803	939.9	0.004361	939.9
0.005453	697	0.004156	939.9	0.00266	674.1	0.004709	697
0.005817	685.5	0.005838	685.5	0.00409	685.5	0.004749	708.5

2nd Der. PB-33	Band PB-33	2nd Der. PB-34	Band PB-34	2nd Der. PB-35	Band PB-35	2nd Der. PB-36	Band PB-36
-0.00629	928.3	-0.0043	743	-0.00726	743	-0.01858	743
-0.00531	743	-0.00367	916.7	-0.00609	731.5	-0.00974	731.5
-0.00403	731.5	-0.00254	928.3	-0.00547	928.3	-0.00711	916.7
-0.00326	754.6	-0.00251	731.5	-0.00441	916.7	-0.00661	928.3
-0.00207	916.7	-0.0011	777.7	-0.00223	777.7	-0.00626	754.6
-0.00161	881.9	-0.00103	754.6	-0.00202	754.6	-0.00481	766.1
-0.00115	777.7	-0.001	881.9	-0.00187	766.1	-0.00478	777.7
-0.00102	560.1	-0.00094	766.1	-0.00124	560.1	-0.0031	881.9
-0.00096	847.1	-0.0008	870.3	-0.0011	870.3	-0.00239	560.1
-0.00082	548.8	-0.00067	905.1	-0.00109	548.8	-0.00189	548.8
.....
0.000509	503.6	0.000225	823.9	0.000661	823.9	0.001231	503.6
0.000582	823.9	0.000239	582.8	0.000674	582.8	0.001324	812.3
0.000612	835.5	0.000271	503.6	0.000833	503.6	0.001612	823.9
0.000945	514.9	0.000592	514.9	0.001777	514.9	0.0025	674.1
0.00102	674.1	0.00064	674.1	0.001855	674.1	0.002566	514.9
0.001951	720	0.002322	685.5	0.003436	720	0.008287	685.5
0.003136	685.5	0.002348	720	0.004096	708.5	0.010162	939.9
0.003891	708.5	0.003319	697	0.0058	685.5	0.011265	720
0.004462	939.9	0.003411	708.5	0.006454	939.9	0.011489	708.5
0.005535	697	0.004137	939.9	0.007057	697	0.012479	697
.....
2nd Der. PB-37	Band PB-37	2nd Der. PB-38	Band PB-38	2nd Der. PB-39	Band PB-39	2nd Der. PB-40	Band PB-40
-0.01372	743	-0.01829	928.3	-0.01646	731.5	-0.01733	928.3
-0.0102	731.5	-0.01634	731.5	-0.01276	928.3	-0.0134	731.5
-0.00725	916.7	-0.01098	754.6	-0.01051	743	-0.01285	754.6
-0.0042	928.3	-0.01005	720	-0.00718	777.7	-0.0088	743
-0.00353	777.7	-0.00897	743	-0.00526	754.6	-0.00549	812.3
-0.00347	766.1	-0.00479	560.1	-0.00451	720	-0.0049	720
-0.00301	754.6	-0.00384	548.8	-0.00408	560.1	-0.00471	777.7
-0.00272	881.9	-0.00367	893.4	-0.00334	916.7	-0.00411	560.1
-0.00225	560.1	-0.00335	537.5	-0.00271	548.8	-0.00304	893.4
-0.00198	800.8	-0.0033	571.4	-0.00219	537.5	-0.00261	548.8
.....
0.000913	582.8	0.001464	582.8	0.001483	582.8	0.00187	503.6
0.000932	503.6	0.001531	662.6	0.001552	823.9	0.002917	835.5
0.002471	674.1	0.001611	594.1	0.001862	503.6	0.003494	514.9
0.002492	514.9	0.002864	503.6	0.003797	708.5	0.003957	674.1
0.002524	812.3	0.003789	766.1	0.004352	514.9	0.00436	916.7
0.007284	720	0.005703	514.9	0.004814	674.1	0.00512	939.9
0.008024	708.5	0.006793	674.1	0.006346	766.1	0.006879	708.5
0.008773	685.5	0.009786	939.9	0.011663	939.9	0.009133	766.1
0.009357	939.9	0.019109	685.5	0.014359	685.5	0.011562	685.5
0.009962	697	0.022103	697	0.018239	697	0.017627	697

2nd Der. PB-41	Band PB-41	2nd Der. PB-42	Band PB-42	2nd Der. PB-43	Band PB-43	2nd Der. PB-44	Band PB-44
-0.00465	754.6	-0.01004	928.3	-0.00214	708.5	-0.00559	916.7
-0.00436	731.5	-0.00798	754.6	-0.00194	823.9	-0.00385	766.1
-0.00388	743	-0.00476	743	-0.00183	720	-0.00384	731.5
-0.00323	928.3	-0.00425	731.5	-0.00178	812.3	-0.00355	720
-0.00204	812.3	-0.00279	812.3	-0.00133	928.3	-0.0034	708.5
-0.00129	560.1	-0.00216	893.4	-0.00124	916.7	-0.00336	823.9
-0.00125	916.7	-0.00127	560.1	-0.00106	905.1	-0.00121	881.9
-0.00093	881.9	-0.00087	789.2	-0.00095	697	-0.00112	905.1
-0.00092	548.8	-0.00087	548.8	-0.00083	651.2	-0.00085	639.7
-0.0008	823.9	-0.00074	847.1	-0.00068	800.8	-0.0008	743
.....
0.00041	662.6	0.001081	514.9	0.0002	503.6	0.000539	503.6
0.000467	503.6	0.001259	720	0.000202	766.1	0.000859	939.9
0.000545	939.9	0.001438	674.1	0.000292	777.7	0.00102	514.9
0.000568	582.8	0.001672	835.5	0.000625	847.1	0.001461	893.4
0.001001	514.9	0.002457	766.1	0.000677	754.6	0.001827	847.1
0.001378	835.5	0.002503	916.7	0.000948	939.9	0.002406	697
0.001631	674.1	0.003647	939.9	0.001341	835.5	0.002754	928.3
0.003386	685.5	0.003667	685.5	0.001718	743	0.003352	674.1
0.00419	708.5	0.00516	708.5	0.001901	674.1	0.004663	754.6
0.005785	697	0.006168	697	0.002436	685.5	0.007192	685.5
2nd Der. PB-45	Band PB-45	2nd Der. PB-46	Band PB-46	2nd Der. PB-47	Band PB-47	2nd Der. PB-48	Band PB-48
-0.00261	720	-0.00319	708.5	-0.00321	928.3	-0.00331	928.3
-0.00212	708.5	-0.00309	720	-0.00255	731.5	-0.00311	812.3
-0.00172	731.5	-0.00304	812.3	-0.00252	754.6	-0.0027	754.6
-0.00166	916.7	-0.00243	823.9	-0.00218	812.3	-0.0021	720
-0.00164	823.9	-0.00151	697	-0.00095	743	-0.00146	893.4
-0.00143	928.3	-0.00076	800.8	-0.00081	823.9	-0.00133	823.9
-0.00127	812.3	-0.00075	651.2	-0.00073	800.8	-0.00086	731.5
-0.00082	800.8	-0.00038	639.7	-0.00072	893.4	-0.00061	800.8
-0.00074	905.1	-0.00035	582.8	-0.00069	720	-0.0006	708.5
-0.00058	639.7	-0.00029	594.1	-0.00068	560.1	-0.00059	858.7
.....
0.000306	789.2	0.000537	766.1	0.000208	582.8	0.000408	881.9
0.000333	514.9	0.000609	928.3	0.000394	503.6	0.000761	514.9
0.000347	743	0.000674	754.6	0.000735	708.5	0.001089	743
0.000683	847.1	0.000801	777.7	0.000799	514.9	0.001298	697
0.000783	835.5	0.001285	731.5	0.001278	766.1	0.001498	939.9
0.000911	754.6	0.001374	847.1	0.001398	674.1	0.001511	674.1
0.000929	939.9	0.001508	674.1	0.001438	835.5	0.001551	916.7
0.001556	697	0.001516	685.5	0.002327	939.9	0.001667	766.1
0.001817	674.1	0.002065	835.5	0.002456	697	0.002242	835.5
0.004015	685.5	0.003551	743	0.003096	685.5	0.002619	685.5

2nd Der. PB-49	Band PB-49	2nd Der. PB-50	Band PB-50	2nd Der. PB-51	Band PB-51	2nd Der. PB-52	Band PB-52
-0.00538	928.3	-0.00783	928.3	-0.00458	916.7	-0.00734	928.3
-0.00324	731.5	-0.00508	731.5	-0.00372	731.5	-0.00483	754.6
-0.00284	743	-0.0043	754.6	-0.00301	743	-0.0032	743
-0.00234	754.6	-0.0042	743	-0.00223	766.1	-0.00314	731.5
-0.00216	777.7	-0.00147	560.1	-0.00098	870.3	-0.00183	916.7
-0.00133	720	-0.00127	777.7	-0.00087	800.8	-0.0017	560.1
-0.00127	812.3	-0.00114	548.8	-0.00084	881.9	-0.0015	893.4
-0.00126	560.1	-0.0011	893.4	-0.00082	548.8	-0.00148	812.3
-0.00111	893.4	-0.00109	847.1	-0.00076	560.1	-0.00126	720
-0.00105	916.7	-0.00105	916.7	-0.00063	905.1	-0.00115	847.1
.....
0.000441	708.5	0.000741	503.6	0.000345	777.7	0.000581	708.5
0.000558	789.2	0.000748	582.8	0.000404	616.9	0.000821	823.9
0.000563	835.5	0.001261	823.9	0.00057	893.4	0.000839	503.6
0.000699	503.6	0.001364	514.9	0.001042	754.6	0.001085	835.5
0.001307	514.9	0.001633	766.1	0.001185	812.3	0.001336	766.1
0.001784	674.1	0.001731	708.5	0.001311	514.9	0.001341	514.9
0.001787	766.1	0.002204	674.1	0.001486	674.1	0.00224	674.1
0.004257	697	0.005938	685.5	0.003159	697	0.005632	697
0.004815	939.9	0.00601	939.9	0.005063	685.5	0.006181	685.5
0.00533	685.5	0.00657	697	0.005519	939.9	0.006332	939.9
2nd Der. PB-53	Band PB-53	2nd Der. PB-54	Band PB-54	2nd Der. PB-55	Band PB-55	2nd Der. PB-56	Band PB-56
-0.0068	928.3	-0.00923	731.5	-0.00726	731.5	-0.01445	928.3
-0.00529	731.5	-0.00867	743	-0.00694	743	-0.00732	731.5
-0.004	916.7	-0.00769	916.7	-0.00398	916.7	-0.00647	754.6
-0.00371	754.6	-0.00383	928.3	-0.0037	766.1	-0.00537	743
-0.00364	743	-0.00336	560.1	-0.00363	928.3	-0.00367	777.7
-0.00209	560.1	-0.00289	766.1	-0.00285	754.6	-0.00266	893.4
-0.00184	720	-0.00201	548.8	-0.00279	560.1	-0.0025	916.7
-0.00164	870.3	-0.00195	881.9	-0.00203	548.8	-0.00213	560.1
-0.00126	548.8	-0.00145	571.4	-0.00184	720	-0.00174	847.1
-0.00125	777.7	-0.00131	800.8	-0.00151	571.4	-0.00154	548.8
.....
0.000721	858.7	0.000802	662.6	0.000729	526.2	0.000806	835.5
0.000749	582.8	0.000884	582.8	0.001268	582.8	0.000835	582.8
0.000756	823.9	0.000889	594.1	0.001464	503.6	0.001279	503.6
0.001011	503.6	0.001363	812.3	0.00163	777.7	0.001767	823.9
0.001164	766.1	0.001378	503.6	0.001868	708.5	0.002597	514.9
0.002066	514.9	0.003076	514.9	0.002553	514.9	0.003105	674.1
0.003403	674.1	0.003721	674.1	0.003143	674.1	0.004554	766.1
0.006333	697	0.008001	939.9	0.003559	939.9	0.008682	697
0.008414	939.9	0.010721	697	0.009828	697	0.011172	685.5
0.010017	685.5	0.012182	685.5	0.010366	685.5	0.014414	939.9

2nd Der. PB-57	Band PB-57	2nd Der. PB-58	Band PB-58	2nd Der. PB-59	Band PB-59	2nd Der. PB-60	Band PB-60
-0.01031	731.5	-0.01937	928.3	-0.00593	916.7	-0.00754	916.7
-0.0084	743	-0.01651	743	-0.00513	731.5	-0.00545	743
-0.00688	916.7	-0.01367	754.6	-0.00346	928.3	-0.00514	731.5
-0.00371	766.1	-0.01102	731.5	-0.00334	743	-0.00228	766.1
-0.00349	928.3	-0.00538	777.7	-0.00143	766.1	-0.00174	928.3
-0.00304	560.1	-0.00293	893.4	-0.00132	881.9	-0.00163	881.9
-0.00228	548.8	-0.00239	560.1	-0.00113	560.1	-0.00144	870.3
-0.00166	870.3	-0.00229	847.1	-0.00112	800.8	-0.00142	777.7
-0.00165	537.5	-0.00211	881.9	-0.00107	777.7	-0.00114	800.8
-0.00154	571.4	-0.00207	812.3	-0.001	548.8	-0.00094	560.1
.....
0.000832	594.1	0.001147	582.8	0.000514	789.2	0.000702	708.5
0.000938	708.5	0.002113	514.9	0.000587	582.8	0.000776	893.4
0.001169	582.8	0.002245	674.1	0.000709	503.6	0.001047	720
0.001463	812.3	0.002286	766.1	0.000916	812.3	0.001347	514.9
0.001669	503.6	0.002576	823.9	0.001304	514.9	0.001588	812.3
0.003141	514.9	0.00889	685.5	0.001326	754.6	0.002184	754.6
0.004317	674.1	0.009614	720	0.002685	674.1	0.002251	674.1
0.009131	939.9	0.013233	708.5	0.004021	697	0.004647	697
0.010768	697	0.01414	939.9	0.007195	685.5	0.006871	685.5
0.013476	685.5	0.015821	697	0.007937	939.9	0.007091	939.9
.....
2nd Der. PB-61	Band PB-61	2nd Der. PB-62	Band PB-62	2nd Der. PB-63	Band PB-63	2nd Der. PB-64	Band PB-64
-0.00786	928.3	-0.0192	928.3	-0.00535	928.3	-0.00198	916.7
-0.00466	754.6	-0.01469	754.6	-0.00214	458.8	-0.001	458.8
-0.00418	731.5	-0.01144	731.5	-0.00213	916.7	-0.00087	447.7
-0.00366	743	-0.0094	743	-0.002	447.7	-0.00077	928.3
-0.00146	916.7	-0.00553	720	-0.00157	754.6	-0.00059	847.1
-0.00144	560.1	-0.00501	893.4	-0.00151	605.5	-0.00056	789.2
-0.00115	789.2	-0.00488	560.1	-0.00145	582.8	-0.00051	674.1
-0.00112	847.1	-0.00468	537.5	-0.00141	571.4	-0.00051	571.4
-0.00093	548.8	-0.00442	812.3	-0.00113	594.1	-0.00042	526.2
-0.00085	881.9	-0.00405	548.8	-0.00102	789.2	-0.00041	628.3
.....
0.000655	582.8	0.002069	708.5	0.000599	560.1	0.00021	560.1
0.000659	503.6	0.002197	492.4	0.000758	685.5	0.000211	720
0.000708	823.9	0.00281	823.9	0.000782	662.6	0.000226	639.7
0.000882	835.5	0.004376	503.6	0.000865	835.5	0.000273	823.9
0.001354	514.9	0.005835	514.9	0.000869	537.5	0.000328	436.5
0.001896	674.1	0.006194	674.1	0.000944	492.4	0.000382	481.2
0.002264	708.5	0.008782	766.1	0.001087	766.1	0.000387	685.5
0.005057	685.5	0.011184	939.9	0.001203	514.9	0.000492	470
0.006191	697	0.017548	685.5	0.001567	481.2	0.000576	514.9
0.006726	939.9	0.017552	697	0.006556	939.9	0.001385	939.9

Appendix D

SYSTAT Output						
Correlation-based, Principal Components Analysis						
CASI-48 Resampled Spectral Library						
Merged Data File (88 signatures)						
6 Dimension Output						
Latent Roots (Eigenvalues)						
	<u>1</u>	<u>2</u>	<u>3</u>	<u>4</u>	<u>5</u>	<u>6</u>
	32.773	12.816	1.362	0.769	0.123	0.066
Component Loadings						
	<u>1</u>	<u>2</u>	<u>3</u>	<u>4</u>	<u>5</u>	<u>6</u>
Band01	0.694	0.585	0.39	-0.029	-0.076	-0.118
Band02	0.721	0.58	0.363	-0.002	-0.059	-0.084
Band03	0.748	0.575	0.326	0.028	-0.042	-0.035
Band04	0.757	0.581	0.291	0.053	-0.027	0.005
Band05	0.759	0.589	0.265	0.067	-0.012	0.029
Band06	0.755	0.603	0.242	0.077	0.005	0.043
Band07	0.749	0.616	0.219	0.087	0.021	0.053
Band08	0.748	0.623	0.196	0.09	0.038	0.062
Band09	0.767	0.61	0.162	0.074	0.053	0.07
Band10	0.832	0.533	0.111	0.009	0.068	0.067
Band11	0.921	0.358	0.042	-0.11	0.078	0.033
Band12	0.949	0.226	-0.014	-0.198	0.08	-0.014
Band13	0.948	0.177	-0.05	-0.241	0.079	-0.041
Band14	0.942	0.181	-0.077	-0.256	0.071	-0.047
Band15	0.931	0.242	-0.11	-0.24	0.057	-0.038
Band16	0.912	0.326	-0.148	-0.194	0.039	-0.022
Band17	0.898	0.373	-0.173	-0.146	0.015	-0.011
Band18	0.892	0.395	-0.188	-0.101	-0.01	-0.005
Band19	0.875	0.429	-0.214	-0.043	-0.019	0.002
Band20	0.854	0.461	-0.236	0.014	-0.021	0.009
Band21	0.835	0.485	-0.247	0.06	-0.019	0.01
Band22	0.797	0.531	-0.254	0.13	-0.001	-0.001
Band23	0.758	0.559	-0.26	0.21	0.006	-0.012
Band24	0.728	0.568	-0.262	0.272	0.006	-0.028
Band25	0.762	0.527	-0.265	0.257	-0.017	-0.02
Band26	0.921	0.28	-0.231	0.057	-0.115	0.029
Band27	0.962	-0.064	-0.113	-0.154	-0.168	0.038
Band28	0.926	-0.289	-0.027	-0.187	-0.14	0.025
Band29	0.877	-0.453	0.025	-0.128	-0.077	0.017
Band30	0.838	-0.536	0.045	-0.075	-0.027	0.016
Band31	0.817	-0.57	0.05	-0.052	-0.002	0.019
Band32	0.803	-0.59	0.056	-0.034	0.008	0.023
Band33	0.798	-0.597	0.053	-0.026	0.009	0.025
Band34	0.796	-0.6	0.05	-0.022	0.007	0.026
Band35	0.794	-0.603	0.048	-0.019	0.005	0.028
Band36	0.795	-0.603	0.044	-0.013	0.003	0.026
Band37	0.796	-0.602	0.04	0.008	0.004	0.018
Band38						

Band39	0.799	-0.597	0.032	0.057	0.013	0.001
Band40	0.799	-0.596	0.029	0.07	0.014	-0.002
Band41	0.798	-0.595	0.026	0.083	0.015	-0.005
Band42	0.799	-0.592	0.022	0.094	0.016	-0.008
Band43	0.803	-0.586	0.017	0.103	0.016	-0.013
Band44	0.806	-0.579	0.014	0.114	0.016	-0.02
Band45	0.808	-0.573	0.01	0.128	0.018	-0.026
Band46	0.814	-0.56	0.003	0.137	0.019	-0.033
Band47	0.824	-0.539	0	0.15	0.02	-0.05
Band48	0.827	-0.526	-0.005	0.168	0.022	-0.057
Variance Explained by Components						
	<u>1</u>	<u>2</u>	<u>3</u>	<u>4</u>	<u>5</u>	<u>6</u>
	32.773	12.816	1.362	0.769	0.123	0.066
Percent of Total Variance Explained						
	<u>1</u>	<u>2</u>	<u>3</u>	<u>4</u>	<u>5</u>	<u>6</u>
	68.277	26.699	2.837	1.601	0.255	0.137
SYSTAT Output						
Covariance-based, Principal Components Analysis						
CASI-48 Resampled Spectral Library						
Merged Data File (88 signatures)						
6 Dimension Output						
Latent Roots (Eigenvalues)						
	<u>1</u>	<u>2</u>	<u>3</u>	<u>4</u>	<u>5</u>	<u>6</u>
	3382.219	72.063	28.677	3.744	2.446	1.171
Component Loadings						
	<u>1</u>	<u>2</u>	<u>3</u>	<u>4</u>	<u>5</u>	<u>6</u>
Band01	0.278	0.935	-0.026	0.453	-0.328	0.107
Band02	0.316	0.974	0.007	0.455	-0.312	0.11
Band03	0.355	1.012	0.043	0.451	-0.283	0.118
Band04	0.37	1.056	0.076	0.449	-0.255	0.125
Band05	0.373	1.085	0.098	0.448	-0.228	0.122
Band06	0.361	1.107	0.118	0.446	-0.205	0.113
Band07	0.349	1.13	0.138	0.444	-0.181	0.103
Band08	0.348	1.156	0.151	0.441	-0.157	0.088
Band09	0.385	1.19	0.145	0.423	-0.122	0.068
Band10	0.537	1.24	0.083	0.367	-0.085	0.016
Band11	0.905	1.35	-0.062	0.26	-0.058	-0.097
Band12	1.289	1.501	-0.216	0.14	-0.036	-0.234
Band13	1.518	1.636	-0.315	0.05	-0.009	-0.328
Band14	1.569	1.727	-0.349	-0.01	0.026	-0.351
Band15	1.41	1.767	-0.287	-0.037	0.083	-0.304
Band16	1.174	1.759	-0.164	-0.042	0.143	-0.224
Band17	1.06	1.757	-0.066	-0.055	0.174	-0.153
Band18	1.019	1.768	0.014	-0.067	0.19	-0.09
Band19						

Band20	0.842	1.727	0.224	-0.06	0.268	-0.001
Band21	0.789	1.737	0.309	-0.046	0.292	0.022
Band22	0.674	1.73	0.437	0	0.318	0.033
Band23	0.579	1.688	0.57	0.037	0.334	0.064
Band24	0.529	1.656	0.678	0.054	0.336	0.093
Band25	0.648	1.698	0.669	0.013	0.335	0.128
Band26	1.436	1.894	0.316	-0.234	0.243	0.229
Band27	3.223	2.151	-0.44	-0.587	-0.056	0.322
Band28	5.643	2.067	-1.109	-0.743	-0.37	0.308
Band29	8.584	1.389	-1.366	-0.548	-0.466	0.14
Band30	10.843	0.602	-1.322	-0.19	-0.314	-0.087
Band31	12.008	0.118	-1.282	0.043	-0.104	-0.198
Band32	12.553	-0.244	-1.194	0.22	0.026	-0.173
Band33	12.855	-0.369	-1.141	0.231	0.112	-0.109
Band34	12.945	-0.412	-1.1	0.195	0.161	-0.037
Band35	12.987	-0.458	-1.063	0.162	0.194	0.038
Band36	13.019	-0.45	-0.96	0.116	0.213	0.08
Band37	13.169	-0.469	-0.663	0.106	0.19	0.106
Band38	13.484	-0.47	-0.223	0.141	0.143	0.071
Band39	13.727	-0.481	0.081	0.132	0.143	0.065
Band40	13.85	-0.498	0.298	0.113	0.128	0.078
Band41	13.973	-0.51	0.505	0.095	0.126	0.101
Band42	14.029	-0.482	0.701	0.062	0.121	0.106
Band43	13.957	-0.38	0.892	-0.001	0.081	0.098
Band44	13.815	-0.292	1.097	-0.046	0.005	0.076
Band45	13.686	-0.225	1.333	-0.075	-0.05	0.032
Band46	13.227	-0.026	1.511	-0.164	-0.143	-0.056
Band47	12.09	0.246	1.677	-0.226	-0.364	-0.214
Band48	11.596	0.367	1.906	-0.282	-0.492	-0.289
Variance Explained by Components						
	<u>1</u>	<u>2</u>	<u>3</u>	<u>4</u>	<u>5</u>	<u>6</u>
	3382.2	72.063	28.677	3.744	2.446	1.171
Percent of Total Variance Explained						
	<u>1</u>	<u>2</u>	<u>3</u>	<u>4</u>	<u>5</u>	<u>6</u>
	96.866	2.064	0.821	0.107	0.07	0.034

APPENDIX E



Figure E-1. Prentiss Bay; False Color Composite.

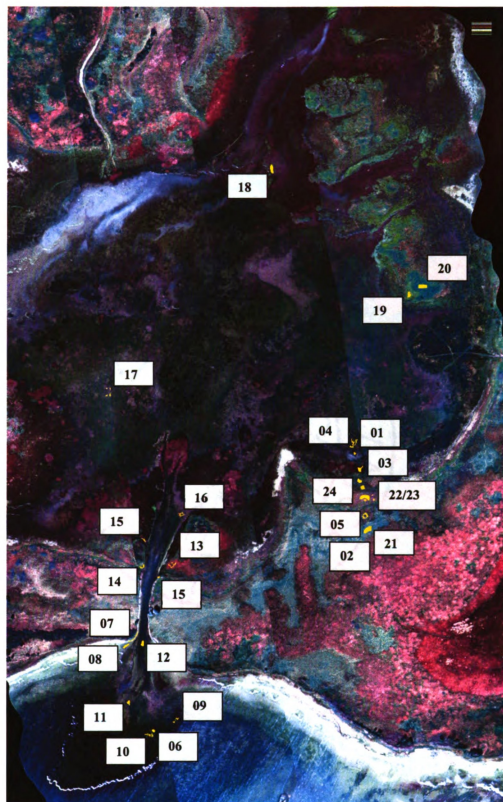


Figure E-2. Horseshoe Bay; True Color Composite and ROIs.

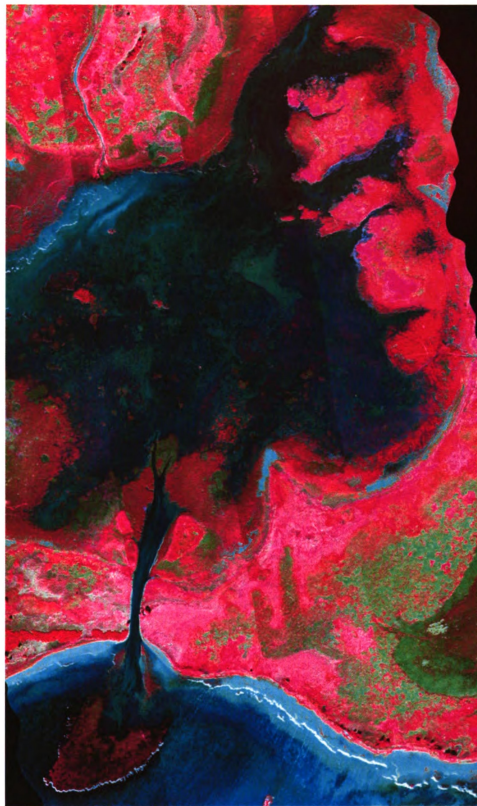


Figure E-3. Horseshoe Bay; False Color Composite.

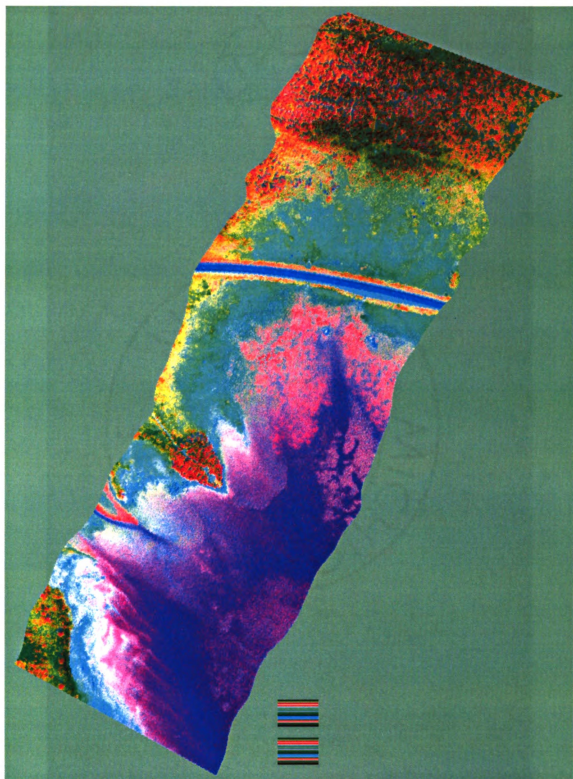


Figure E-4. Prentiss Bay, PC-image; 4, 3, 2 Color Composite.

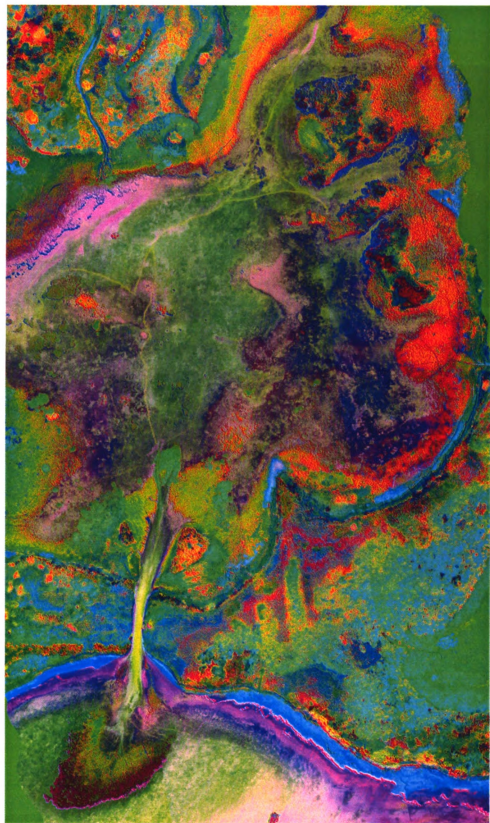
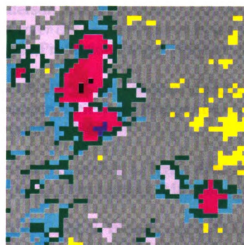


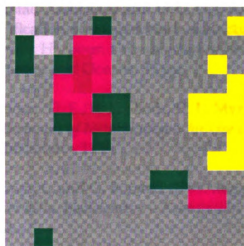
Figure E-5. Horseshoe Bay PC-Image; 4, 3, 2 Color Composite.



1-meter Spatial Resolution



2-meter Spatial Resolution



4-meter Spatial Resolution



8-meter Spatial Resolution

Figure E-6. Pixel Level Spatial Degradation Patterns.

BIBLIOGRAPHY

Anderson, J. R., E. E. Hardy, J. T. Roach, and R. E. Witmer. 1976. *A land use and land cover classification system for use with remote sensor data*: U.S. Geological Survey Professional Paper #964, p. 28.

ASPRS, 1995. Land satellite information in the next decade: Data notebook, American Society of Photogrammetry and Remote Sensing (ASPRS), Bethesda, Maryland, USA.

Avery, T. E., and G. L. Berlin. 1986. Fundamentals of Remote Sensing and Airphoto Interpretation. Macmillian Publishers, NY.

Best, R. G., M. E. Wehde, and R. L. Linder. 1981. *Spectral reflectance of hydrophytes*. Remote Sensing of Environment, Vol. 11: Pp. 27-35.

Borstad Associates Ltd. 1995. Fish habitat mapping: Remote sensing, verification of imagery and production of digital maps from Baynes Sound and Comox Harbour. Unpublished report prepared for the Canadian Department of Fisheries and Oceans. 33 pp.

Bowker, D. E., R. E. Davis, D. L. Myrick, K. Stacy, and W. T. Jones. 1985. *Spectral Reflectances of Natural targets for Use in Remote Sensing Studies*. NASA Reference Publication – 1139.

Brown, L. and G. Borstad. 1999. *Mapping wetland breeding habitats in the Frazier River delta*. Backscatter – Association of Marine Remote Sensing Vol. 10(1): Pp. 8-11.

Burton, T. M., D. G. Uzarski, J. P. Gathman, J. A. Genet, B. E. Keas, C. A. Stricker. 1999. *Development of a preliminary invertebrate index of biotic integrity for Lake Huron coastal wetlands*. Wetlands Vol. 19(4): Pp. 869-882.

Butera, M. K. 1983. *Remote Sensing of Wetlands*. IEEE Trans. Geoscience Remote Sensing. Vol. 21: Pp. 383-392.

Campbell, J. B. 1996. Introduction to remote sensing, 2nd edition. The Guilford Press, NY.

Cardinale, B. J., V. J. Brady, and T. M. Burton. 1998. *Changes in the Abundance and Diversity of Coastal Wetland Fauna from the Open Water/Macrophyte edge towards shore*, Wetlands Ecology and Management Vol. 6(1). Pp. 59-68.

Carter, G. A. 1993. *Responses of leaf spectral reflectance to plant stress*. American Journal of Botany Vol. 80(3): Pp. 239-243.

Carter, G. A. 1998. *Reflectance bands and indices for remote estimation of photosynthesis and stomatal conductance in pine canopies*. Remote Sensing and Environment. Vol. 63: Pp. 61-72.

Carter, V. P., and R. R. Anderson. 1982. *Interpretation of wetlands imagery based on spectral reflectance characteristics of selected plant species*. Proceedings of the American Society of Photogrammetry 38th Annual Meeting, Pp. 580-595.

Chadde, S.W. 1998. A Great Lakes Wetland Flora, Pocketflora Press, Calumet, Michigan.

Chow-Fraser, P., and D. A. Albert. 1998. *Biodiversity Investment Areas: Coastal Wetland Ecosystems*. State of the Lake Ecosystem Conference-1998. United States Environmental Protection Agency and Environment Canada.

Clark, R.N., G.A. Swayze, A.J. Gallagher, T.V.V. King, and W.M. Calvin, 1993, *The U. S. Geological Survey, Digital Spectral Library: Version 1: 0.2 to 3.0 microns*, U.S. Geological Survey Open File Report 93-592, 1340 pages.

Comer, A. J., Albert, D.A., Wells, H. A., Hart, B. L., Raab, S. B., Price, D. L., Kashian, D.M., Corner, R. A., and Shuen, D. W. 1995. *Michigan's Native Landscape, as Interpreted from general Land Office Surveys, 1816-1865*. Michigan Natural Features Inventory Report to Water Division, U.S. EPA and Wildlife Division, Michigan Dept. of Nat. Res. Lansing, Michigan.

Congalton, R. G. 1991. *A review of Assessing the Accuracy of Classifications of Remotely Sensed Data*. Remote Sensing and Environment. Vol. 37: Pp. 35-46.

Congalton, R. G., 1983. *Assessing Landsat Classification Accuracy Using Discrete Multivariate Analysis Statistical Techniques*. Photogrammetric Engineering and Remote Sensing, Vol. 49(12): Pp. 1671-1678.

Cowardin, L. M., V. Carter, F. C. Golet, and E. T. LaRoe. 1979. *Classification of wetlands and deep-water habitats of the United States*. U.S. Department of the Interior, Fish and Wildlife Service, Washington DC.

Crist, E. P., and R. C. Cicone, 1984. *Application of Tasselled Cap Concept to Simulated Thematic Mapper Data*. Photogrammetric Engineering and Remote Sensing, Vol. 50: Pp. 343-352.

Dahl, T. E. 2000. *Status and trends of wetlands in the conterminous United States - 1986 to 1997*. U.S. Department of the Interior, Fish and Wildlife Service, Washington, DC.

Dahl, T.E., C. E. Johnson, and W. E. Frayer. 1991. *Status and Trends of wetlands in the Conterminous United States - Mid 1970's to mid 1980's*, U.S. Department of the Interior, Fish and Wildlife Service, Washington, DC.

Davis, J. C. 1986. Statistics and Data Analysis in Geology. John Wiley & Sons, New York.

Demetriades-Shah, T. H., M. D. Steven, and J. A. Clark. 1990. *High resolution derivative spectra in remote sensing*. Remote Sensing and Environment. Vol. 33: Pp.55-64.

Detenbeck, N. E., S. M. Galatowitsch, J. Atkinson, and H. Bell. 1999. *Evaluation perturbations and developing restoration strategies for inland wetlands in the Great Lakes basin*. Wetlands Vol. 19(4): Pp. 789-820.

Earnst-Dottavio, C. L., R. M. Hoffer, and R. P. Morczynski. 1981. *Spectral characteristics of wetland habitats*. Photogrammetric Engineering and Remote Sensing Vol. 47: Pp. 223-227.

Elvidge, C. D., and F. P. Portigal. 1990. *Reflectance spectra of green and dry vegetation derived from 1989 AVIRIS data*. Proceedings, fifth Australian remote sensing conference, Perth Australia: Pp 185-195.

Elvidge, C. D., and Z. Chen. 1995. *Comparison of broad-band and narrow-band red and near infrared vegetation indices*. Remote Sensing and Environment. Vol. 54: Pp. 38-48.

Environment Canada. 1994. *Environmental Sensitivity Atlas for Lake Huron's Canadian Shoreline*. Environment Canada.

ESRI, 2001. ARCINFO users manual, page 158. Redlands, California. Fell, A. F., and G. Smith. 1982. *Higher derivative methods in ultraviolet-visible and infrared spectroradiometry*. Analytical Procedures. Vol. 54: Pp. 28-32.

Forsyth, F., G. Borstad, W. Horniak, and L. Brown. 1998. *Prince Rupert intertidal habitat inventory project*. Unpublished report to Prince Rupert Port Corporation, the Canadian Department of Fisheries and Oceans, and the City of Prince Rupert.

Gathman, J., and B. Keas. 1999. *Les Cheneaux coastal wetland project: A synthesis*. A report submitted to the Michigan Coastal Management Program, Project Number 99-3099-24 by The Nature Conservancy.

Goetz, A. F. H. 1992. *Principles of narrow band spectroscopy in the visible and IR: instruments and analysis*. In Imaging spectrometry: fundamentals and prospective applications, edited by F. Toselli and J. Bodechtel (Dordrecht: Kluwer), Pp 21-32.

Gottgens, J. F., Swartz, B. P., Kroll, R. W. and Eboch, M. 1998. *Long term GIS-based records of habitat changes in a Lake Erie coastal marsh*. Wetlands Ecology and Management Vol. 6(1): Pp. 5-17.

Gross, M. F., and V. Klemas. 1986. *The use of airborne imaging spectrometer (AIS) data to differentiate marsh vegetation*. Remote Sensing of Environment Vol. 19: Pp. 97-103.

Gross, M. F., M. A. Hardisky, and V. Klemas. 1989. *Applications to coastal wetlands vegetation*. In Theory and applications of optical remote sensing, Ghassem Asrar, Editor. John Wiley and Sons, NY.

Hardisky, M. A., Gross, M.F., and Klemas, V. 1986. *Remote Sensing of Coastal Wetlands*. Bioscience, Vol. 36(7): Pp.453-460.

Henderndorf, C. E. 1987. *Lake Eerie coastal wetlands: an overview*. Journal of Great Lakes Research, Vol. 18(4) Pp. 533-551.

<http://www.borstad.com/papers/terranoval.html>. March 20, 2001. Intertidal Habitat in Terra Nova National Park.

Hudson W. D., and C. W. Ramm, 1987. *Correct Formulation of the Kappa Coefficient of Agreement*. Photogrammetric Engineering and Remote Sensing, Vol. 53(4): Pp. 421-422.

Huguenin, R. LO., and J. L. Jones. 1986, *Intelligent information extraction from reflectance spectra: absorption band position*. Journal of Geophysical Research. Vol. 91(B9): Pp. 9585-9598.

International Joint Commission. 1993. *Levels Reference Study, Great Lakes St. Lawrence River Basin, Annex 2. Landuse Management*. International Joint Commission.

ITRES Research Limited, 2000. Draft report – *Airborne Imaging Systems for Coastal Applications: An Update*. For Joint Airborne Lidar Bathymetry Technical Center of Expertise, Mobile, Alabama.

Jain, A. K., 1989. *Fundamentals of Digital Image Processing*. Prentice Hall, Englewood Cliffs, NJ.

Jaworski, E, and N. C. Raphael. 1978. *Fish, Wildlife, and Recreational Values of Michigan's Coastal Wetlands*. Michigan Department of Natural Resources: Lansing, Michigan.

Jensen, J. R. 1996. Remote Sensing of the Environment : an Earth Resource Perspective. Prentice Hall. Upper Saddle River, NJ.

Jensen, J. R. 1996. Digital Image Processing Prentice Hall. Upper Saddle River, NJ.

Jensen, J. R., E. J. Christiansen, and R. Sharitz. 1984. *Non-tidal wetland mapping in South Carolina using airborne multispectral scanner data*. Remote Sensing of Environment Vol. 16: Pp. 1-12.

Jensen, J. R., M. E. Hodgson, E. Christensen, M. E. Jr. Halkard, L. R. Tinney, and R. Sharitz. 1986. *Remote Sensing Inland Wetlands: A Multispectral Approach*. Photogrammetric Engineering. Vol. 52(1): Pp. 87-100.

Jupp, D. L. B. G. Byrne, J. Anstee, E. McDonald, T. McVicar and D. Parkin. (1996). *Port Phillip Bay sea grass mapping project G2.2. Final report series I, II, III and IV*. CSIRO Division of Water Resources, Consulting Reports 96/.

Kauth, R. J., and G. S. Thomas. 1976. *The tasseled cap – A graphical description of spectral-temporal development of agricultural crops as seen by Landsat*. Proceedings, 6th International Symposium on machine Processing of Remotely Sensed Data, Purdue University West Lafayette, IN. Pp. 41-51.

Keddy, P. A. and A. A. Reznicek. 1986. *Great Lakes vegetation dynamics: the role of fluctuating water levels and buried seed*. Journal of Great Lakes Research Vol. 12 Pp.25-36.

Keough, J. R., T. A. Thompson, G. R. Guntenspergen, and D. A. Wilcox, 1999. *Hydrogeomorphic factors and ecosystem responses in coastal wetlands of the Great Lakes*. Wetlands Vol. 19(4): Pp. 821-834.

Koonce, J. F., C. K. Minns, and H. A. Morrison. 1999. *Biodiversity investment areas, aquatic ecosystems*. State of the Lakes Ecosystem Conference (SOLEC, 1998).

Krieger, K. A., 1992. *The Ecology of invertebrates in Great lakes Coastal Wetlands*, Journal of Great Lakes Research Vol. 18(4): Pp. 634-650.

Kruse, F. A., A. B. Lefkoff, J. W. Boardman, K. B. Heidebrecht, A. T. Shapiro, J. P. Barloon, and A. F. H. Goetz. 1993. *The Spectral Image Processing System (SIPS) – Interactive visualization and analysis of imaging spectrometer data*. Remote Sensing of Environment, Vol. 44: Pp. 145-163.

Kumar, L., K. S. Schmidt., S. Dury and A. K. Skidmore. (in press 2001) *Review of Hyperspectral Remote Sensing and Vegetation Science*. In van der Meer, F., (2001) (editor). Hyperspectral Remote Sensing (Kluwer Academic Press: Dordrecht)

Lillesand, T.M., and R.W. Kiefer. 1994. Remote Sensing and Image Interpretation, 3rd Edition. John Wiley and Sons, NY.

Lillesand, T.M., and R.W. Kiefer. 2000. Remote Sensing and Image Interpretation, 4th Edition. John Wiley and Sons, NY.

Maynard, L. and D. Wilcox. 1997. *Coastal Wetlands*. Background Paper, State of the Lakes Ecosystem Conference (SOLEC, 1996).

Minc, L. D. 1997. *Great Lakes Coastal Wetlands: An overview of controlling abiotic factors, regional distribution, and species composition*. A report submitted to the Michigan Natural Features Inventory, December, 1997.

Mitsch, W. J., and J. G. Gosselink. 2000. Wetlands – 4th Edition, John Wiley & Sons, Inc. New York, NY.

Oguma, H., Nakayama, M., Nishio, F., Yamagata, Y. 1996. *Studies on metrologies for monitoring the distribution of wetland vegetation using multispectral data in Kushiro Mire, Japan*, in Proceeding at the Second International Airborne Remote Sensing Conference and Exhibition, San Francisco, California, Vol. II: Pp. 711-716.

Prince, H. P., P. I. Padding, and R. W. Knapton. 1992. *Waterfowl use of the Laurentian Great Lakes*. Journal of Great Lakes Research, Vol. 18(4): Pp 673-699. Proceedings, 2nd International Symposium on Automated Cartography, Ottawa. Vol. 2: Pp. 883-896.

Raphael, N. C. 1987. *Prehistoric and historic wetland heritage of the upper great lakes*. Michigan Academician, Vol. 19(3): Pp. 331-365.

Reimold, R. J., J. L. Gallagher, and D. E. Thompson. 1973. *Remote Sensing of Coastal Marsh*. Photogrammetric Engineering and Remote Sensing Vol. 39: Pp. 477-488.

Research Systems, Inc., 1999. ENVI User's Manual, Version 3.2.

Ritter, R. and E. L. Lanzer. 1997. *Remote sensing of nearshore vegetation in Washington State's Puget Sound*. Proceedings of the 1997 Geospatial Conference, Seattle, WA, Vol. 3: Pp. 527-536.

Roe, H. B. and Q. C. Ayres. 1954. Engineering for Agricultural Drainage, McGraw- Hill, New York.

Rummel R. J. 1970. Applied Factor Analysis. Northwestern University Press, Evanston, IL.

Sabins, M. J., 1987. *Convergence and consistency of Fuzzy c-means/ISODATA algorithms*. IEEE Transactions Pattern Analysis & Machine Intelligence, Vol. 9: Pp. 661-668.

Savastano, K. J., K. H. Faller, and R. L. Iverson. 1984. *Estimating vegetation coverage in St. Joseph Bay, Florida with an airborne multispectral scanner*. Photogrammetric Engineering and Remote Sensing Vol. 50: Pp. 1159-1170.

Seher, S.J., and Tueller, P.T., 1973. *Color Aerial Photos for Marshland*. Photogrammetric Engineering. Vol. 39(2): Pp. 489-499.

Shafique, N. A., A.C. Bradley, F. Fulk, and S. M. Cormier, 2001. *The Selection of Narrow Wavebands for Optimizing Water Quality Monitoring on the Great Miami River, Ohio using Hyperspectral Remote Sensor Data* Journal of Spatial Hydrology Vol. 1(1): Pp. 1-22, (<http://www.spatialhydrology.com>).

Singh, a., and A. Harrison. 1985. *Measuring the fractal dimensions of surfaces*. Proceedings, 2nd International Symposium on Automated Cartography, Ottawa. Vol. 2: Pp. 883-896.

Smith, P. G. R., V. Glooschenko, V., and D. A. Hagen. 1991. *Coastal wetlands of the three Canadian Great Lakes: inventory, current conservation initiatives and patterns of variation*. Canadian Journal of Fisheries and Aquatic Sciences Vol. 48: Pp. 1581-1594.

- Stewart, W. R., V. Carter, and P. D. Brooks. 1980. *Inland (non- tidal) wetland mapping*. Photogrammetric Engineering and Remote Sensing Vol. 46: Pp. 617-628.
- Stoney, W. E. and J. R. Hughes, 1998. *A new space race is one!* GIS World, Vol. 11: Pp. 44-46.
- Thenkabail, P.S., R. B. Smith, and E. DePauw. 2000. *Hyperspectral Vegetation Indices and Their Relationships with Agricultural Crop Characteristics*. Remote Sensing and Environment. Vol. 71: Pp. 158-182.
- Tou, J. T. and R. C. Gonzalez, 1974. Pattern Recognition Principles. Addison-Wesley Publishing Company, Reading, Massachusetts.
- Tsai, F., and W. Philpot. 1998. *Derivative Analysis of Hyperspectral data*. Remote Sensing and Environment. Vol. 66: Pp. 41-51.
- Wang, J., L. Zhang, and Q. Tong. 1998. *The derivative matching for wetland vegetation identification and classification by hyperspectral data*. In Proceedings of SPIE, Hyperspectral Remote Sensing and Application. Volume: 3502: Pp. 280-288.
- Wetzel, R. G., 1992. *Wetlands as Metabolic Gates*, Journal of Great Lakes Research, Vol.18(4) Pp. 529-532.
- Wilcox, D. A. 1995. *The role of wetlands as nearshore habitat in Lake Huron*. In Munawar, M., T., Edsall, and J. Leach (eds.) The Lake Huron Ecosystem: ecology, fisheries and management. SPB Academic Publishing, Amsterdam, The Netherlands. Pp. 223-245.
- Zacharias, M, O. Niemann, and G. Borstad. 1992 An assessment and classification of a multispectral bandset for the remote sensing of intertidal seaweeds. Canadian Journal of Remote Sensing, Vol. 18(4) Pp. 263-274.
- Zarco-Tejada, P. J. and J. R. Miller. 1999. *Land cover mapping at BOREAS using red edge spectral parameters from CASI imagery*. Journal of Geophysical Research. Vol. 22: p. 27
- Zelazny J. and J. S. Feierabend, Editors. 1988. Increasing our Wetland Resources. National Wildlife Federation, Washington, DC.

MICHIGAN STATE UNIVERSITY LIBRARIES



3 1293 02372 6700